



**University of
Nottingham**
UK | CHINA | MALAYSIA

Manufacturing Metrology Team

Faculty of Engineering

**Applications of coherence scanning
interferometry in additive manufacturing**

by

Carlos Alberto Gomez Moreno

Thesis submitted to the University of Nottingham for the degree of

Doctor of Philosophy

December 2021

Abstract

Additive manufacturing (AM) is increasingly being used to fabricate fully functional parts. In this scenario, tolerances for dimensions and surface finish become crucial, especially for applications with stringent requirements. Therefore, the measurement of AM parts is essential to ensure adequate performance and to inform the manufacturing process. Typical metal AM surfaces are highly irregular, exhibiting a large number of high aspect-ratio topographic features, deep recesses and loose particles, while polymer AM surfaces are often translucent or have low reflectivity. Because of these characteristics, it can be challenging for any surface measuring technique to accurately measure the topography of metal and polymer AM surfaces.

Coherence scanning interferometry (CSI) is one of the most accurate methods for areal surface topography measurement. CSI uses an interferometric objective lens and spatially extended, spectrally broadband illumination. When scanning a surface along the optical axis through the focus of the interferometric objective lens, interference fringes will be visible only within a narrow surface height range, corresponding to the zero group-velocity optical path difference of the interferometer. This phenomenon is known as 'low-coherence interference' and provides a highly accurate non-contact sensing mechanism to determine the three-dimensional topography of a surface.

CSI has the ability to measure a wide range of surface types, from optically smooth to rough, as well as discontinuous surfaces without the 2π ambiguity that can arise with single-wavelength, phase-shifting interferometry. However, due to the limited numerical aperture of the imaging system, CSI may suffer from poor signal-to-noise ratios when measuring high-slope angle topographic features and surfaces with significant texture, or more generally, surfaces with low reflectance, compromising the ability to reliably determine surface heights.

Although previous CSI technologies have shown difficulties when measuring AM surfaces, recent progress in the development of CSI allows a significantly enhanced detection sensitivity through the use of advanced analysis techniques,

such as filtering of the light source spectrum bandwidth, high dynamic range lighting levels, oversampling (i.e. adjusting the number of camera acquisitions over each interference fringe) and sophisticated topography reconstruction algorithms. In this thesis, the effects of the aforementioned advanced analysis techniques on the measurement of typical as-built metal AM surfaces covering various textures and slope distributions are empirically investigated and systematically analysed. Guidelines are provided for the optimisation of the measurement of metal AM surfaces by balancing the total data acquisition time, the size of the measurement area, and the percentage of measured data points (i.e. data coverage).

The detailed surface topography information captured with CSI is essential for providing feedback to the manufacturing process and for quality control of AM products. To validate this, a challenging case study has been considered. The feasibility of ink-jet printing a transparent polymer of tetrafluoroethylene, hexafluoropropylene and vinylidene fluoride (known as THV) to produce films of a few nanometres to several micrometres in thickness has been assessed using CSI. Solutions to minimise the 'coffee ring' effect and the formation of undesired wrinkle-like features on the surface when ink-jet printing THV are demonstrated. This work contributes to the field of polymer AM by providing insight into how to control and optimise the quality of ink-jet printed parts with the aid of surface metrology.

Reducing measurement noise in CSI is an important consideration when measuring AM surfaces, in particular when the ability to capture data is compromised by poor signal-to-noise ratios. This thesis contributes to the understanding of the workings of measurement noise reduction methods and compares their effects when measuring surface topography in the presence of environmental vibration. The results provide guidance for the reduction of error in surface measurement for AM surfaces, and could be applied in a wider range of applications. The knowledge developed in this research is relevant to the manufacturing and scientific communities as CSI technologies are increasingly applied to the measurement of complex surfaces and in environments that resemble production areas more than metrology laboratories.

Declaration of authorship

I, Carlos Alberto Gomez Moreno, hereby declare that this thesis entitled “Applications of coherence scanning interferometry in additive manufacturing” is my own work, except where specific reference is made to the work of others. The work presented in this thesis was carried out entirely during my doctoral studies at the University of Nottingham, under the supervision of Professor Richard Leach, Dr Simon Lawes, Dr Rong Su and Professor Peter de Groot. The contents of this thesis have not been submitted in whole or in part for consideration for any other degree or qualification in this, or any other university.

Acknowledgements

I am deeply grateful to CONACYT for providing me with the scholarship that allowed me to carry out my PhD studies. I would like to express my sincere gratitude to my supervisors Professor Richard Leach, Dr Simon Lawes and Dr Rong Su for their valuable advice, patient guidance and continuous support throughout my PhD studies. Their knowledge, experience, passion and work culture inspire me to be better and what they have given me will undoubtedly benefit the rest of my life.

I am very thankful to my industry supervisor Professor Peter de Groot (Zygo Corporation, USA) for his insightful comments and suggestions at every stage of my research project. I feel very lucky to have had the opportunity to collaborate with him. My appreciation extends to my internal assessor Dr Samanta Piano for her assistance and constructive feedback. I would also like to thank all of my colleagues from the Manufacturing Metrology Team for their kind support and friendship.

I am eternally grateful to my dad Salvador and my mom Eva for their endless love, encouragement and unwavering support. For nurturing me in every aspect. For being such amazing parents. All that I am or hope to be, I will always owe to them. Many thanks to my grandparents, my brothers, my aunts, my uncles, my cousins, my friends and everyone who has ever cared about me. I would like to offer special thanks to Aislinn for brightening my days and filling me with so much love, for being there by my side in these strange pandemic times. I am also grateful to all of my teachers, and others, who have taught me valuable lessons along the way. I dedicate my PhD to my lovely daughter Eva and to my wonderful family. No matter where I go, they are always in my heart and in my thoughts. I am blessed to have them in my life. They are, truly, my greatest source of strength and joy. I wish them, always, immense happiness.

“The journey of a thousand miles begins with a single step.”

– Lao Tzu

Table of contents

Abstract	I
Declaration of authorship	III
Acknowledgements	IV
Table of contents	V
List of figures	IX
List of Tables	XIV
1 Introduction	1
1.1 Motivation, aim and objectives	1
1.2 Research novelty	4
1.3 Thesis outline.....	4
1.4 List of publications.....	6
2 Surface topography measurement for additive manufacturing	9
2.1 Additive manufacturing.....	9
2.1.1 Overview of additive manufacturing technologies	9
2.1.2 Powder bed fusion.....	11
2.1.3 Material jetting.....	13
2.1.4 The roles of surface measurement in additive manufacturing .	14
2.2 Surface topography measurement	16
2.2.1 Introduction to surface metrology	16
2.2.2 Profile and areal measurement	17
2.2.3 Contact and non-contact methods.....	20

2.2.4	Areal surface texture characterisation	24
2.2.5	Measurement uncertainty and error	26
2.2.6	Metrological characteristics for areal surface topography measurement.....	30
2.2.6.1	Measurement noise	31
3	Coherence scanning interferometry	35
3.1	Introduction to CSI.....	35
3.2	Working principles	37
3.2.1	Configuration	37
3.2.2	Signal formation	39
3.2.3	Surface topography reconstruction methods	43
3.3	Considerations and characteristic errors	46
3.4	Applications and technical advances.....	49
4	Coherence scanning interferometry for metal additive manufacturing.....	55
4.1	Introduction	55
4.2	Advanced functions in CSI.....	58
4.2.1	Topography reconstruction method	58
4.2.2	Filtering of the source spectrum.....	58
4.2.3	Oversampling.....	59
4.2.4	HDR lighting levels	59
4.3	Method.....	60
4.3.1	Instrument.....	60
4.3.2	Samples	61
4.3.3	Experimental design	62

4.4	Results	63
4.4.1	Areal surface texture measurements	63
4.4.2	Effects of measurement functions and settings on data coverage.....	65
4.4.2.1	Effects of spectral filtering.....	65
4.4.2.2	Effects of oversampling.....	66
4.4.2.3	Effects of HDR of lighting levels.....	68
4.4.3	Recommendations for the optimisation of the measurement...	69
4.5	Conclusion.....	70
5	Process-surface analysis in polymer additive manufacturing.....	73
5.1	Introduction	73
5.2	Materials and methods.....	74
5.2.1	THV 221	74
5.2.2	Ink-jet printing of THV 221	75
5.2.3	Surface-measuring coherence scanning interferometry	77
5.2.4	Surface topography analysis.....	78
5.3	Results	80
5.3.1	THV 1 wt. % in MIBK	80
5.3.2	THV 10 wt. % in MIBK.....	83
5.3.3	THV 20 wt. % in 50–50 vol. % MIBK–acetone.....	84
5.4	Conclusion.....	86
6	Noise reduction in coherence scanning interferometry	89
6.1	Introduction	89
6.2	Methods.....	91
6.2.1	Topography averaging.....	91

6.2.2	Oversampling.....	92
6.2.3	Instrument and materials	94
6.2.4	Evaluation of measurement noise	94
6.2.5	Noise density	95
6.3	Results over a range of surface tilts	96
6.3.1	Noise as a function of data acquisition time	96
6.3.2	Correlated and uncorrelated noise	98
6.3.3	Evaluation of environment-induced vibration	99
6.3.4	Simulation of surface measurement and environment-induced vibration	100
6.4	Conclusion	103
7	Conclusions and future work.....	105
7.1	Concluding remarks	105
7.2	Areas for future work	107
	References	109

List of figures

Figure 1.1 Topography of a metal AM surface: top surface of a Ti-6Al-4V part produced by laser powder bed fusion and imaged via a digital optical microscope (adapted from [13]).	2
Figure 2.1 Generic illustration of PBF.	11
Figure 2.2 Examples of the topographies of PBF surfaces made of (a) Ti-6Al-4V and (b) Al-Si-10Mg. The scale bar is 50 μm . The surfaces were measured with CSI [45].	12
Figure 2.3 Illustration of ink-jet printing operating in drop-on-demand mode.	13
Figure 2.4 Example of the surface topography of an inkjet-printed hexagonal structure made of a fluoropolymer. The surface was measured with CSI.	14
Figure 2.5 Illustration of the different surface types, adapted from [84].	17
Figure 2.6 Example of (a) profile and (b) areal measurement of a metal AM surface.	18
Figure 2.7 Coordinate system and measurement loop of an areal surface topography measurement instrument (adapted from [19]).	19
Figure 2.8 Diagram of the NA of a microscope objective lens.	21
Figure 2.9 Surface measurement of an AM part using CSI.	23
Figure 2.10 Filtering of a metal AM surface topography (a) original topography measured with CSI, (b) S-F surface showing the underlying large-scale waviness and (c) S-L surface showing weld tracks and spatter formations.	25
Figure 2.11 Illustration of the difference between accuracy and precision.	28
Figure 2.12 Calibration pyramid [112].	29

Figure 2.13 Illustration of the distinction between (a) instrument noise and (b) measurement noise, adapted from [94].....	32
Figure 3.1 Schematic of a CSI instrument, adapted from [29].....	37
Figure 3.2 Schematic of interference objectives typically used for CSI. (a) Mirau and (b) Michelson type, adapted from [142].	38
Figure 3.3 Appearance of low-coherence interference fringes during the axial scanning process (adapted from [18, 145]).	40
Figure 3.4 Conceptual diagram of the signal formation by incoherent superposition, adapted from [29].	41
Figure 3.5 CSI signal for a single camera pixel as a function of scan position z showing the coherence envelope (adapted from [28]).....	42
Figure 3.6 Illustration of the FDA method, adapted from [131].....	45
Figure 3.7 CSI measurements of metal AM surfaces with several missing data points over regions featuring high slopes and deep recesses. A 5.5 \times lens (0.5 \times zoom) was used.....	47
Figure 3.8 Example of an application of CSI for the measurement of automotive fuel injectors. Deviations outside tolerance can lead to reduced fuel efficiency and unacceptable emissions (adapted from [194]).	50
Figure 3.9 Wide-field interference microscope objective for areal surface topography measurement with coaxial, slightly tilted reference and beam splitter plates (adapted from [142]).	52
Figure 4.1 Pictures of the metal AM samples: (a) Al-Si-10Mg, (b) Ti-6Al-4V LPBF cubes, and (c) Ti-6Al-4V EBPBF rectangular prism.	61
Figure 4.2 CSI measurements of metal AM surfaces: (a–b) LPBF Al-Si-10Mg cube top surfaces, (c) LPBF Al-Si-10Mg cube side surface, (d) LPBF Ti-6Al-4V cube top surface, (e) EBPBF Ti-6Al-4V rectangular prism top surface, and (f) LPBF Ti-6Al-	

4V cube side surface. The 1.4× objective lens (1× zoom) was used for (a), the 5.5× objective lens (1× zoom) was used for (b–e), and the 50× objective lens (1× zoom) was used for (f).....	65
Figure 4.3 Effects of spectral filtering on data coverage. The data coverage is plotted against (a) Sq and (b) Sdq . The 5.5× objective lens (1× zoom) was used.	66
Figure 4.4 Effects of oversampling on data coverage. (a) Data coverage plotted against oversampling factor where the factor number equal to one means oversampling is not used; (b), (d), (f) and (h) measured topography maps of S1, S2, S3 and S4 without using oversampling, respectively; (c), (e), (g) and (i) measured topography maps of S1, S2, S3 and S4 using 8× oversampling, respectively. The 5.5× objective lens (1× zoom) and the 40 nm bandwidth spectrum were used.	67
Figure 4.5 Effects of oversampling on data coverage for (a) EBPBF Ti-6Al-4V rectangular prism top surface (S4) using the 5.5× objective lens (0.5 and 1× zoom) and (b) LPBF Ti-6Al-4V cube side surface (S5) using the 20× and 50× objective lenses (1× zoom). The 40 nm bandwidth spectrum was used.....	68
Figure 4.6 Comparison of performance between HDR (two lighting levels) and oversampling (2×). (a) The data coverage is plotted against Sdq . The result of the original measurement without using any of the advanced functions is shown as the crosses; (b), (d), (f) and (h) measured topography maps of S1, S2, S3 and S4 using HDR, respectively; (c), (e), (g) and (i) measured topography maps of S1, S2, S3 and S4 using 2× oversampling, respectively. The 5.5× objective lens (0.5× zoom) and the 40 nm bandwidth spectrum were used.....	69
Figure 5.1 Diagram of thickness calculation.	79
Figure 5.2 Surface topography and profiles corresponding to (a) one and (b) two-layer ink-jet printed drops of THV 1 wt. % in MIBK.	80
Figure 5.3 Thickness for the centre (T_c) and edge (T_e) of ink-jet printed drops of THV 1 wt. % in MIBK with increased number of layers.	81

Figure 5.4 Surface topography and profile of a one-layer ink-jet printed film of THV 1 wt. % in MIBK.....	82
Figure 5.5 Surface topography corresponding to (a) five-layer, (b) ten-layer, (c) twenty-layer and (d) fifty-layer ink-jet printed films of THV 1 wt. % in MIBK....	83
Figure 5.6 Surface topography corresponding to (a) a one-layer drop, (b) a two-layer drop, (c) a one-layer film and (d) a two-layer film of ink-jet printed THV 10 wt. % in MIBK.....	84
Figure 5.7 Surface topography corresponding to (a) a one-layer drop, (b) a two-layer drop, (c) a one-layer film and (d) a two-layer film of ink-jet printed THV 20 wt. % in 50–50 vol. % MIBK–acetone.....	85
Figure 5.8 Surface topography corresponding to a heat-treated ten-layer film of ink-jet printed THV 20 wt. % in 50–50 vol. % MIBK–acetone.....	86
Figure 6.1 CSI signal acquired (a) with a typical sampling rate of four camera frames per fringe and (b) with oversampling at eight frames per fringe ($N = 2$).	93
Figure 6.2 Experimental results: measurement noise for the SiC flat measured at a 0° , 2° and 4° tilt angles. Each line corresponds to the least squares fit using Equation (6.10). The coefficient βM for each fitted line is shown in the legend.	97
Figure 6.3 Difference between two successive individual measurements acquired using oversampling for the SiC flat at a (a) 0° tilt angle and a (b) 4° tilt angle along the horizontal axis.....	98
Figure 6.4 Evaluation of the environment-induced vibration. (a–c) Examples of measured environment-induced vibration profiles; (d–f) their corresponding amplitude spectra.....	99
Figure 6.5 Simulation of surface measurement. (a) The mean and interpolated vibration amplitude spectra; (b) an arbitrary simulated environment-induced vibration profile; (c) the (simulated) measured surface profile; (d) the (simulated) areal surface topography measurement.....	101

Figure 6.6 Simulation results: measurement noise for a flat surface measured at 2° and 4° tilt angles. Each line corresponds to the least squares fit using Equation (6.10). The coefficient βM for each fitted line is shown in the legend..... 102

Figure 6.7 True colour surface topography measurement for a Ti-6Al-4V LPBF sample measured with CSI. The measurement represents a 4×4 laterally stitched 3D image for a $50\times$ lens ($NA = 0.55$). Adapted from [45, 124]..... 104

List of Tables

Table 2.1 Metrological characteristics in ISO 25178 part 600 [94].	30
Table 4.1 Optical parameters for different objective lenses [239].	60
Table 4.2 Results of the areal surface texture parameters.	63
Table 4.3 Measurement optimisations for metal AM surfaces in terms of measurement time and FOV (95% minimum data coverage by default).	70
Table 5.1 Vapour pressure and viscosity at 20 °C for the solvents used to dissolve THV [255].	76
Table 5.2 Viscosity of THV 221 inks (mean of three measurements) at different temperatures.	76
Table 5.3 CSI instrument specification.	78
Table 6.1 Optical parameters for the investigated objective lenses.	94
Table 6.2 Noise density for the SiC flat measured at a 0° tilt angle.	97

1 Introduction

1.1 Motivation, aim and objectives

Additive manufacturing (AM) holds substantial promise for the fields of engineering and industrial production [1]. By providing the ability to selectively add material to a part as it is formed, AM can produce complex part geometries that were previously beyond the capabilities of conventional subtractive manufacturing [2], finding applications in fields from biomedical implants [3] to aerospace engineering [4]. Since AM technologies rarely require part-specific tooling, setup costs are reduced, allowing for economic low volume production [5]. Other advantages of AM include functional integration, shorter lead times and reduced material waste [6, 7].

While there are substantial advantages with AM, there are still open challenges in improving the manufacturing process. One of these challenges is the surface finish of as-built AM parts, which is still poor when compared to that achievable with well-established methods (e.g. subtractive manufacturing) [8, 9]. In general, the understanding of the complex physical interactions occurring during AM processes is still limited [10-12]. One motivation for carrying out the work presented in this thesis is that accurate surface topography information can be useful for better understanding, controlling and optimising AM processes, ultimately allowing the achievement of higher quality manufactured goods [13]. As Lord Kelvin, one of the most important physicists of the 19th century, once said, “To measure is to know,” and also, “If you cannot measure it, you cannot improve it” [14].

Yet another challenge is the ability to reliably measure the topography of AM surfaces [8]. Common issues of surface metrology for metal and polymer AM arise from the complex and highly irregular surface topographies that result from the AM processes. Metal AM surfaces typically present local high slopes, deep recesses, high aspect-ratio features and undercuts, as well as varying surface texture and regions with a large variation in reflectance [8, 9]. In the case of

polymer AM, surfaces are often translucent or have low reflectivity [15-17]. An example image taken from a metal AM surface is shown in Figure 1.1. This image provides a qualitative notion of the complexity of the topographic features that must be faced when measuring AM surfaces.

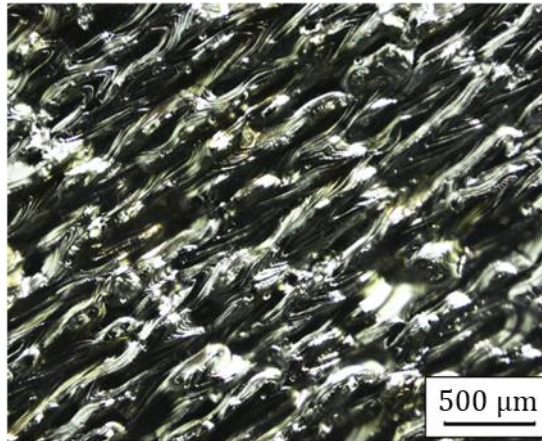


Figure 1.1 Topography of a metal AM surface: top surface of a Ti-6Al-4V part produced by laser powder bed fusion and imaged via a digital optical microscope (adapted from [13]).

A variety of technologies are currently available for measuring the three-dimensional topography of surfaces at the micrometre and sub-micrometre scales, including optical methods such as coherence scanning interferometry (CSI) [18, 19], focus variation microscopy (FV) [20, 21] and confocal microscopy (CM) [22, 23]. Surface metrology instruments based on optical techniques are considerably faster in terms of independent surface measurement points per unit time than those using a contact stylus, which involve mechanical raster scanning to measure a surface area [24]. Furthermore, the non-contact nature of optical instruments provides the benefit of avoiding the risk of damaging the measured surface [25].

Optical interferometers can be used to measure length in terms of the wavelength of light [26]. For the measurement of areal surface topography, optical interferometers divide the source light so that it follows two independent paths, with one path to the reference surface and the other to the object surface. The two light beams are then recombined and directed to a digital camera that captures the resulting light intensity over an array of image points simultaneously. The resulting light intensity is highly sensitive to the differences in path lengths,

providing measurement sensitivity along the axial direction in the nanometre range [27]. A fundamental characteristic of optical interferometry methods is that the measurement sensitivity in the axial direction does not depend on the lens magnification, as opposed to other optical methods that rely on focus [28]. This is due to the use of the wavelength of light as a metric for length measurement, rather than the focus position.

At present, the dominant optical interferometry methods for the measurement of areal surface topography are phase-shifting interferometry (PSI) and CSI [29]. The CSI technique is based on the localisation of broadband light interference fringes during axial scanning as a means to evaluate the topography of a surface. CSI has the ability to measure a wide range of surface types, from optically smooth to surfaces featuring large height variations or discontinuities without the height range limitation related to the 2π ambiguity that can arise with PSI [18].

However, because of the limited numerical aperture of the optical imaging system, CSI and other optical methods may come under poor signal-to-noise ratios when measuring surface topography features with high slope angles and surfaces with high levels of texture, compromising the ability to reliably determine surface heights [30]. As mentioned before, these surface topography characteristics are common in AM parts. Although CSI can achieve sub-nanometre measurement noise when measuring flat surfaces with a smooth texture [31], measurement noise levels can rise significantly when measuring complex surfaces [32] and environmental disturbances may further compromise measurement accuracy.

New developments in CSI technology have enhanced the baseline sensitivity of a measurement, expanding the capability of CSI instruments to measure surface features with high slopes or low reflectance and therefore making CSI a potentially valuable tool for process development and quality control of AM parts. The aim of this thesis is to identify, demonstrate and optimise new applications for CSI in AM. The objectives are to:

- Investigate the effects of CSI measurement parameters on the measurement of AM surfaces.
- Optimise the conditions and settings for the measurement of AM surfaces with CSI.

- Demonstrate the use of CSI as an off-line process development and quality control tool in AM.
- Advance the understanding of the workings of data acquisition strategies to reduce measurement noise in CSI.

1.2 Research novelty

This thesis contributes to the development of guidelines for optimal CSI measurement of AM surfaces and a wide variety of applications. The novelty of the work presented here lies in the following:

- Evaluation of the effectiveness of recent technical enhancements in CSI when measuring as-built metal AM surfaces.
- Development of approaches to optimise the measurement of metal AM surfaces with CSI.
- Demonstration of the application of CSI as an off-line tool for process development and optimisation in ink-jet printing (material jetting).
- Advancement in the understanding of the topographic formations that result from the ink-jet printing process of THV (a fluoropolymer material).
- Experimental comparison of the effectivity of measurement noise reduction methods on surface topography measurement.
- Development of a simple method to model the effects of measurement noise reduction methods where the environmental vibration is considered.
- Advancement in the understanding of the practical application of noise reduction methods in real-world conditions.

1.3 Thesis outline

A brief description of the content of each chapter is given below:

- Chapter 2 begins with an overview of additive manufacturing technologies, focusing on powder bed fusion and material jetting processes. The roles of

surface topography measurement in additive manufacturing are discussed. This is followed by a review on surface topography measurement, covering profile and areal measurement, contact and non-contact methods, as well as relevant terms related to measurement uncertainty and error. Finally, the metrological characteristics for areal surface topography measuring instruments are presented, focusing on measurement noise.

- Chapter 3 addresses the working principles of CSI, including instrument configuration, signal formation and surface topography reconstruction methods. The characteristic measurement errors that have been reported in the literature are discussed, followed by a review on industrial applications and recent technical advances.
- Chapter 4 presents the findings of an experimental investigation of the use of coherence scanning interferometry for measuring metal additively manufactured surfaces. The implemented approach takes advantage of recent technical enhancements in coherence scanning interferometry, including high dynamic range lighting levels and adjustable data acquisition rates to improve the signal-to-noise ratio. The investigation covered several typical metal additively manufactured surfaces made from different high-performance engineering materials and powder bed fusion processes. This chapter provides recommendations for measurement optimisation, balancing data coverage, measurement area, and measurement time.
- Chapter 5 presents the results of an investigation into the relationship between the ink-jet printing process of a transparent fluoropolymer and the resulting surface topography measured with coherence scanning interferometry. The experimental design covered a variety of ink-jet printed single- and multi-layer structures with basic geometries. Relevant printing parameters, including polymer concentration, drop spacing and number of layers were selected and varied to produce the samples used for the investigation. This chapter provides a better understanding of the characteristic topographic features that result from the ink-jet printing

process and an insight into how to control and optimise the quality of ink-jet printed polymer parts.

- Chapter 6 presents an investigation into data acquisition strategies to reduce measurement noise in coherence scanning interferometry, consisting of 1) averaging a sequence of repeated topography measurements, and 2) increasing the sampling frequency of the fringe signal during a single data acquisition. This chapter improves the understanding of the mechanisms of the two noise reduction methods and compares their effects on surface topography measurement in the presence of environment-induced vibration. The results provide guidance for the reduction of uncertainty in surface measurement for a wide range of applications.
- Finally, Chapter 7 summarises the main conclusions and provides recommendations for future research that expands upon the new knowledge that is presented within this thesis.

1.4 List of publications

The work presented in this thesis resulted in three peer-reviewed journal papers and five conference papers, all of which are published.

Peer-reviewed journal papers:

- Gomez, C., Campanelli, C., Su, R., Leach, R. K. 2020. Surface-process correlation for an ink-jet printed transparent fluoroplastic. *Surf. Topogr.: Metrol. Prop.* **8**, 034002.
- Gomez, C., Su, R., de Groot, P., Leach, R. K. 2020. Noise reduction in coherence scanning interferometry for surface topography measurement. *Nanomanuf. Metrol.* **3**, 68–76.
- Gomez, C., Su, R., Thompson, A., DiSciacca, J., Lawes, S., Leach, R. K. 2017. Optimization of surface measurement for metal additive manufacturing using coherence scanning interferometry. *Opt. Eng.* **56**(11), 111714.

Conference papers:

- Gomez, C., Su, R., Lawes, S., Leach, R. K. 2019. Comparison of two noise reduction methods in coherence scanning interferometry for surface measurement. *Proceedings of the 14th International Symposium of Measurement Technology and Intelligent Instruments (ISMTII 2019)*, Niigata, Japan, September 1st – 4th.
- Gomez, C., Campanelli, C., Su, R., Lawes, S., Leach, R. K. 2019. Characterisation of the surface topography evolution of an ink-jet printed transparent fluoroplastic with coherence scanning interferometry. *Proceedings of the 22th Conference on Metrology and Properties of Surfaces (Met & Props 2019)*, Lyon, France, July 3rd – 5th.
- DiSciacca, J., Gomez, C., Thompson, A., Lawes, S., Leach, R. K., Colonna de Lega, X., de Groot, P. 2017. True-color 3D surface metrology for additive manufacturing using interference microscopy. *Proceedings of the Special Interest Group Meeting between euspen and ASPE on Dimensional Accuracy and Surface Finish in Additive Manufacturing*, pp. 145–148, Leuven, Belgium, October 10th – 12th.
- Gomez, C., Su, R., Thompson, A., DiSciacca, J., Lawes, S., Leach, R. K. 2017. Optimisation of surface topography characterisation for metal additive manufacturing using coherence scanning interferometry. *Proceedings of the Special Interest Group Meeting between euspen and ASPE on Dimensional Accuracy and Surface Finish in Additive Manufacturing*, pp. 162–166, Leuven, Belgium, October 10th – 12th.
- Gomez, C., Su, R., Thompson, A., DiSciacca, J., Lawes, S., Leach, R. K. 2017. Coherence scanning interferometry for metal additive manufacturing. *Proceedings of the 16th Conference on Metrology and Properties of Engineering Surfaces (Met & Props 2017)*, Gothenburg, Sweden, June 26th – 29th.

Part of the work presented here contributed in the following peer-reviewed journal paper:

- Newton, L., Senin, N., Gomez, C., Danzl, R., Helmlı, F., Blunt, L., Leach, R. K. 2019. Areal topography measurement of metal additive surfaces using focus variation microscopy. *Addit. Manuf.* **25**, 365-389.

2 Surface topography measurement for additive manufacturing

2.1 Additive manufacturing

2.1.1 Overview of additive manufacturing technologies

The joint ISO/ASTM terminology standard defines additive manufacturing (AM) to be the ‘process of joining materials to make parts from three-dimensional model data, usually layer upon layer, as opposed to subtractive manufacturing and formative manufacturing methodologies’ [33]. The benefits of AM include geometric design flexibility, functional integration, minimum material waste, economic low volume production and shorter lead times [5-7]. Due to the reduction of design constraints that AM facilitates relative to conventional manufacturing, the production of complex parts that would previously have been constructed as multi-component assemblies is possible. In summary, AM processes involve the following eight steps, starting with a computer-aided design (CAD) model, and resulting in a finished part [2]:

- Step 1: CAD. A digital three-dimensional model is created according to the specifications set by the designer.
- Step 2: Conversion to triangulated model. The CAD model is converted into a triangulated model, often in .STL format. This file describes the external surfaces of the original CAD model as a set of connected triangles and forms the basis for calculation of the slices.
- Step 3: File transfer to the AM machine. The file describing the triangulated model of the part (e.g. .STL file) is loaded onto the AM machine. The file is then configured to have the correct position and orientation for building. The triangulated model is sliced into layers and machine-readable code is generated to manufacture the layers.

- Step 4: Machine setup: The process parameters must be properly set up on the machine prior to the build process.
- Step 5: Build. The part is built by the machine.
- Step 6: Removal. Once the AM machine has completed the build, the produced part must be removed. Since many AM machines operate at high temperatures, the build volume is cooled down if necessary.
- Step 7: Post-processing. The produced part is cleaned. Any support structures are removed.
- Step 8: Application. The finished part is ready for use.

AM processes are classified into seven categories based on the binding mechanism and the feedstock morphology or delivery: binder jetting, directed energy deposition, material extrusion, material jetting, powder bed fusion (PBF), sheet lamination, and vat polymerization [34]. In this thesis, the processes used to produce the investigated AM samples were PBF and material jetting. AM is broadly applicable to all classes of materials including metals, polymers, ceramics and composites [35].

AM saw its first successful commercialisation in the late 1980s with a stereolithography printer designed by 3D Systems, while PBF processes were first commercialised in the early 1990s [2]. Back in the 1990s, the high cost, narrow variety of material choices, and low dimensional accuracy of these systems limited their industrial application to rapid prototyping [16]. During the 2000s and early 2010s, the expiration of key patents for a number of older AM processes opened the market to competition, resulting in new generations of commercial systems offering a wider range of materials and enhanced capabilities. Low-cost, powerful computers contributed to make AM machines smaller and more affordable; quality improved to the point that AM technologies could be used to produce tooling and end use parts. Advances in CAD software made modelling of three-dimensional objects straightforward and inexpensive, while the Internet made knowledge sharing simple, enabling the development of open-source software and hardware [1, 2].

Today, wide scale adoption of AM has occurred in the medical, dental, architecture, aerospace and automotive industries, while low-cost machines have

made AM technologies available to the masses [2, 16]. AM technologies can be used for the production of models, prototypes, fixtures, tooling, assemblies and end use parts [1, 2]. The evolution of AM is being pulled by market factors such as the increased demand for customised products, the need for shorter product development cycles and lead times, as well as the increased focus on sustainability [1, 36, 37].

2.1.2 Powder bed fusion

AM of high-performance metal alloys such as titanium, aluminium and nickel alloys, can provide significant advantages to industry, such as weight savings of parts, reduced lead times and lesser design constraints, which are particularly attractive for aerospace, automotive and biomedical applications [4, 38-43]. Among metal AM processes, PBF has been the process with the greatest economic impact and is the subject of extensive research [36], representing a logical focus for the purposes of the work presented in this thesis. PBF is a process in which thermal energy (typically a laser or electron beam) selectively fuses regions of a powder bed [34]. An illustration of PBF is shown in Figure 2.1.

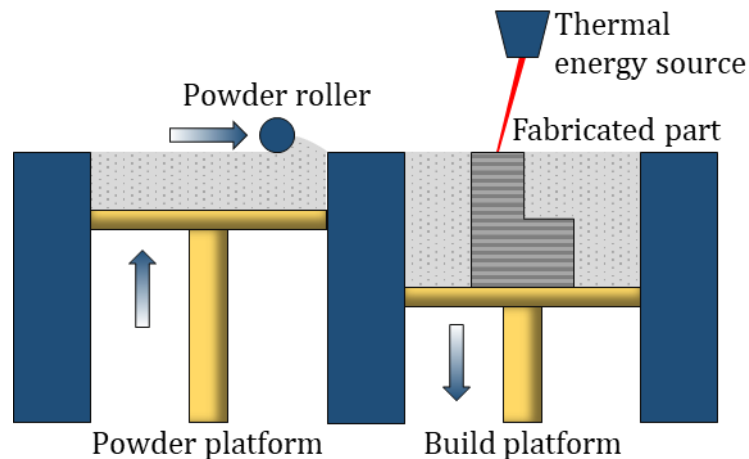


Figure 2.1 Generic illustration of PBF.

The two most common PBF processes are laser PBF (LPBF) and electron beam PBF (EBPBF). LPBF is also referred to as selective laser melting, while EBPBF is sometimes referred to as electron beam melting [44]. In LPBF, a laser beam is rastered over the surface of a powder bed, causing selected areas to melt and fuse.

As the laser beam moves away, the molten areas cool down and solidify. The build platform is then lowered by a single-layer thickness (typically between 20 μm and 150 μm in thickness) and by laying and fusing successive layers of powder, complex three-dimensional parts can be formed. The build chamber is filled with an inert gas (commonly argon) to avoid the oxidisation of the metal as it melts and solidifies. EBPF is based on the same working principles as LPBF, but the thermal energy source is an electron beam (rather than a laser beam) and the build chamber is under vacuum to avoid the electron beam deflection by gas molecules [2].

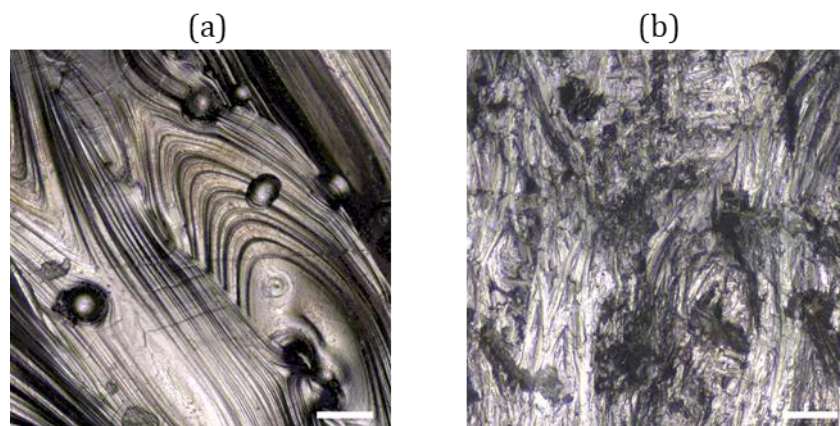


Figure 2.2 Examples of the topographies of PBF surfaces made of (a) Ti-6Al-4V and (b) Al-Si-10Mg. The scale bar is 50 μm . The surfaces were measured with CSI [45].

PBF processes can be difficult to control due to the complex interaction between the laser/electron beam and the powder bed, involving numerous process parameters such as beam power, scan speed, scan pattern, hatch spacing, particle size and layer thickness [11, 46, 47]. As a result of multiple melting phenomena, typical PBF surfaces tend to be highly irregular, exhibiting high slopes, deep recesses and local high aspect-ratio topographic features. Figure 2.2 provides a qualitative notion of the complexity of the topographic features that must be faced when measuring PBF surfaces. Because of these characteristics, PBF surfaces can be highly challenging for any type of measurement technique, requiring a careful selection of measurement conditions to minimise a number of common error sources (this issue will be discussed in more detail later in this chapter). Nevertheless, key process parameters may be identifiable from the specific textures and topographic features that they produce, e.g. weld tracks, weld ripples

and spatter formations. This realisation suggests that the correlation of surface topography with process parameters can be used to provide feedback for process control [8-10, 48-59].

2.1.3 Material jetting

Material jetting is a process in which droplets of build material are selectively deposited [34]. Material jetting is based on well-established ink-jet printing technologies [2]. Typically, ink-jet printing means printing two-dimensional documents or images, meanwhile in AM refers to the printing of three-dimensional parts or structures. In ink-jet printing, a print head ejects droplets of liquid phase material (e.g. a polymer ink) at precise coordinates onto the substrate; the deposited ink droplets dry to form a film and, by printing sequential layers, three-dimensional parts can be formed [2, 60].

A given polymer ink is made by dissolving the polymer in a suitable solvent or solvent combination. Generally, ink droplets are ejected in continuous or drop-on-demand mode; in continuous mode, a stream of droplets is continuously generated and diverted to a gutter when not needed, while in drop-on-demand mode the droplets are generated only when required by piezoelectric actuation [2, 61, 62]. An illustration of an ink-jet printing system operating in drop-on-demand mode is shown in Figure 2.3.

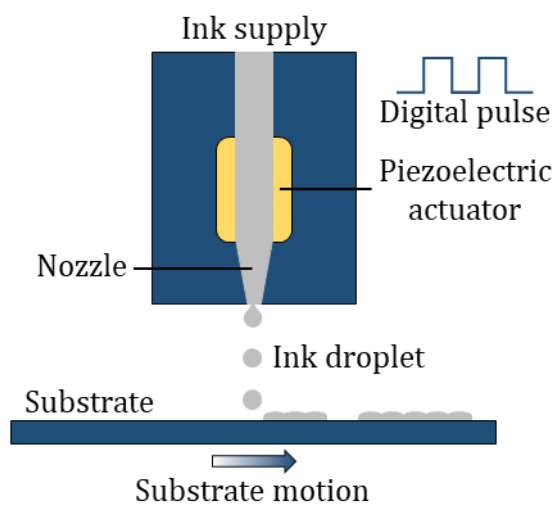


Figure 2.3 Illustration of ink-jet printing operating in drop-on-demand mode.

Due to its low cost and flexibility, ink-jet printing is considered to be one of the key technologies in the field of controlled micro- and nanoscale deposition of polymers [63, 64]. Ink-jet printing has been employed for the fabrication of polymer transistor circuits [65], light-emitting polymer displays [66-68], polymer solar cells [69], as well as polymer sensors and actuators [70, 71].

While ink-jet printing and other polymer AM technologies have been on the market for several years, it has been identified that there are still many advances that can be made [72]. A general issue is the limited understanding about the impact of process parameters on the quality of printed parts [12]. Particularly, there is scarce knowledge regarding the optimal printing parameters (e.g. polymer concentration and type of solvent) for some specific polymers. The measurement and analysis of surface topography, as exemplified in Figure 2.4, can be helpful to advance the understanding of the correlation between ink-jet printing process of specific materials parameters and the resulting surface texture.

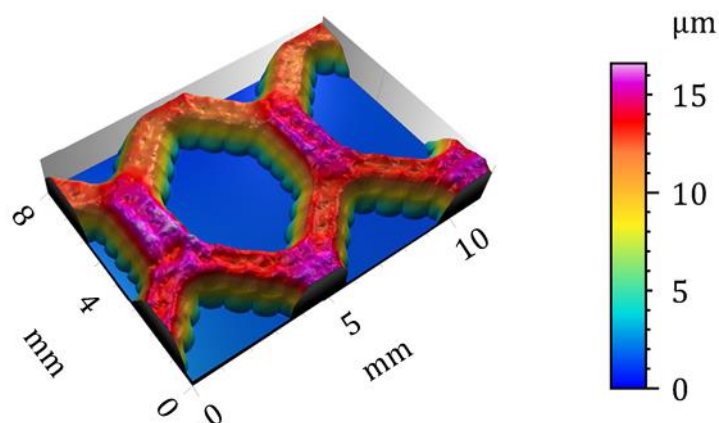


Figure 2.4 Example of the surface topography of an inkjet-printed hexagonal structure made of a fluoropolymer. The surface was measured with CSI.

2.1.4 The roles of surface measurement in additive manufacturing

There are currently a number of significant barriers, related to quality assurance, to further industrial adoption of AM for the production of high-value goods. While AM has the benefit of allowing the creation of complex geometries and internal features that cannot be produced using subtractive processes due to tool path

restrictions, the dimensional control, surface integrity (i.e. condition of a surface produced by a manufacturing process) and surface texture are still not equivalent to those achievable using subtractive processes [8, 73]. For AM to gain more industrial acceptance and become an established method of high-value manufacture, AM processes must be well understood in order to be well controlled. Therefore, rigorous verification of parts produced by AM processes is required, which includes accurate surface topography measurement [9].

Until recently, AM parts in general have suffered from a limited understanding of the mechanisms of the underlying processes [11, 44]. The measurement of AM surfaces in their 'as-built' state may be useful to better understand how the topographic features of a given surface were formed, and ultimately how these topographic features correlate to the AM process parameters that created that surface. On the other hand, the measurement of AM surfaces that have been subjected to further finishing processes is necessary to determine whether the surfaces comply with specifications. Therefore, the measurement of surface topography in AM is fundamental for providing feedback for process optimisation, as well as for product quality control [9, 13].

Several methods exist for the measurement of surface topography (this topic will be discussed in more detail in the next section). Optical methods, such as coherence scanning interferometry, focus variation microscopy and confocal microscopy, can capture topographic information with a high level of detail and are significantly faster than contact stylus measurements that require mechanical raster scanning to cover a surface area. Nevertheless, typical as-built AM surfaces can present significant challenges to existing (contact and non-contact) surface topography measuring methods, as they are often highly complex and irregular, hence revealing the need to develop basic knowledge on how to optimise the measurement of AM surfaces [8, 9, 17, 74-77].

2.2 Surface topography measurement

2.2.1 Introduction to surface metrology

Manufactured parts must comply to design specifications and standards, which include geometrical and surface requirements. The surface is usually defined as the material boundary of a component, through which it interacts with other components or the environment in which the component operates [78]. The term used to refer to the geometrical information associated to all the features present on a surface is surface topography, which is comprised of surface form and surface texture [79]. Surface form is the underlying shape of a part within the measured surface region, while surface texture is the geometrical irregularities present at a surface. Surface texture does not include those geometrical irregularities contributing to the form or shape of the surface [80]. In a practical sense, surface texture refers to what remains after the surface form has been removed from the surface topography. Figure 2.5 depicts the relationship between surface topography, surface form and surface texture.

The science and application of measurement and characterisation of surface texture is surface metrology [13]. In the previous century, the measurement of surface texture was primarily achieved by tracing a contact stylus across the surface to be measured, whose vertical displacement is converted into a signal as a function of position [81, 82]. The 1980s and 1990s saw the appearance of automated interferometric microscopy and the development of several other optical methods for surface topography measurement, which have the benefit of being non-contact and faster than stylus instruments [24, 83].

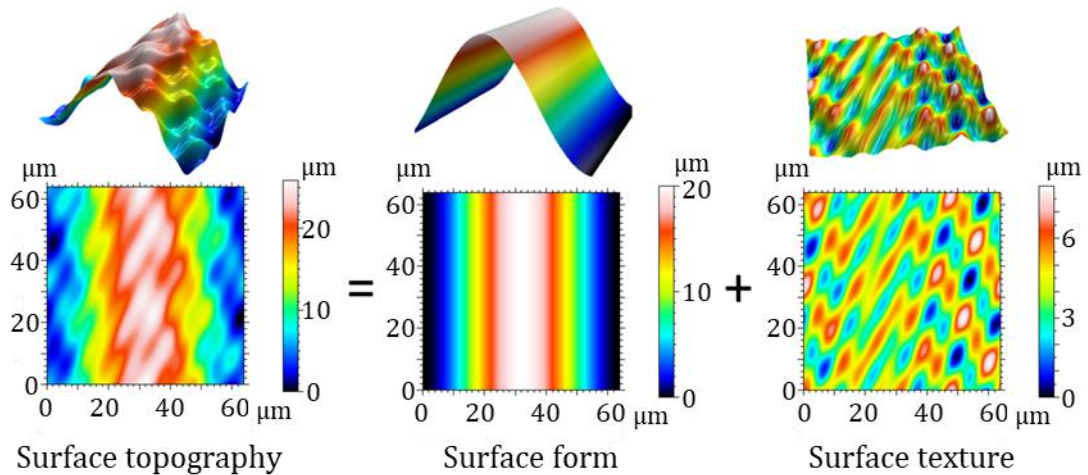


Figure 2.5 Illustration of the different surface types, adapted from [84].

Along with material properties and surface integrity [85, 86], surface texture plays an important role in the functionality of manufactured components (e.g. tribological properties, fatigue resistance and heat transfer) [87, 88]. The need to control and therefore accurately measure the surface topography becomes increasingly important as components and devices get smaller and more complex, in which case the surface topography features become key functional features of a component [25, 83, 87].

On the other hand, surface metrology is indispensable to increase the understanding of the ‘fingerprint’ (i.e. traces left on the topography of the surface) of manufacturing processes that are still at an early stage of industrialisation, such as AM processes [48, 74]. Thus, in modern manufacturing, surface metrology is instrumental not only for part quality control, but also for process development and optimisation [83, 89].

2.2.2 Profile and areal measurement

There are two approaches for the measurement of surface topography – profile and areal measurement [79, 90]. Profile measurement (or line profiling) refers to the measurement of an individual line across the surface, which may be represented mathematically as a one-dimensional height function $z(x)$ [79, 90]. An example of the result of a profile measurement is shown in Figure 2.6(a).

Methods that were developed to measure line profiles include contact stylus scanning [91] and optical differential profiling [92].

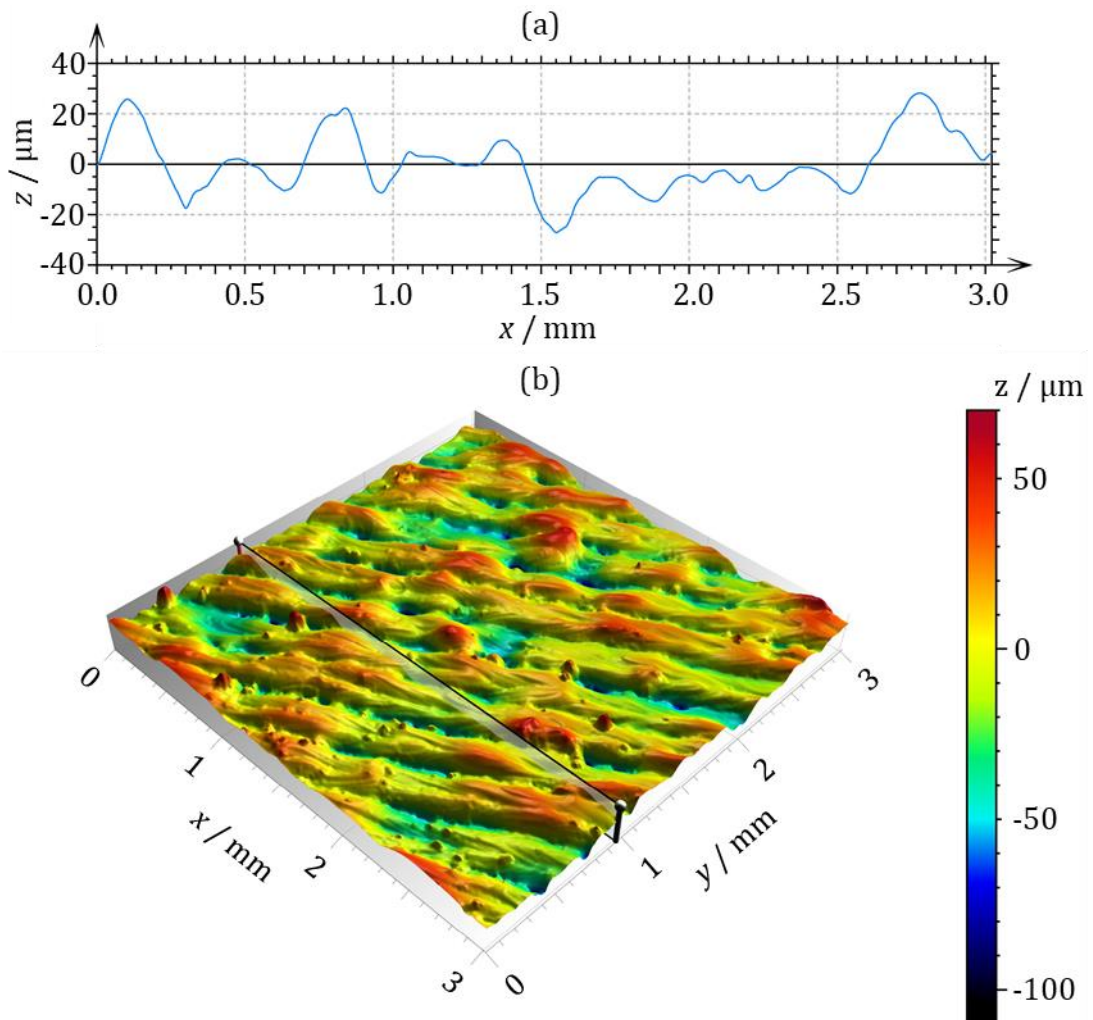


Figure 2.6 Example of (a) profile and (b) areal measurement of a metal AM surface.

Areal measurement extends the profile case to two dimensions to cover an area, producing a topographical three-dimensional image of a surface, which may be represented mathematically as a height function $z(x,y)$ of two independent variables (x,y) [79, 90]. An example of the result of an areal measurement is shown in Figure 2.6(b). Areal measurement capability can be obtained from a set of parallel profiles scanned sequentially (a process sometimes referred to as raster scanning); however, this approach is time-consuming. Alternatively, optical methods can image an entire area at once, significantly reducing measurement time [24]. Examples of methods for areal measurement include coherence

Surface topography measurement for additive manufacturing

scanning interferometry [18, 19], focus variation microscopy [20, 21] and confocal microscopy [22, 23].

While profile measurement can be used for process and quality control purposes, areal measurement can provide considerably more information about the topography of a surface [13, 79, 93]. Actually, not all surface topographies may be adequately described by individual profile measurements. For example, the topography of a metal AM surface often contains relevant information in multiple directions, which may not be fully captured by an individual profile measurement (see Figure 2.6). Furthermore, areal measurements have more statistical significance than equivalent profile measurements, merely because there are more data points [79]. Although profile measurement is well established and widely used in industry, the growing demand for manufactured components with tailored surface features for enhanced functionality is positioning areal measurement as a more useful approach to surface topography measurement [25].

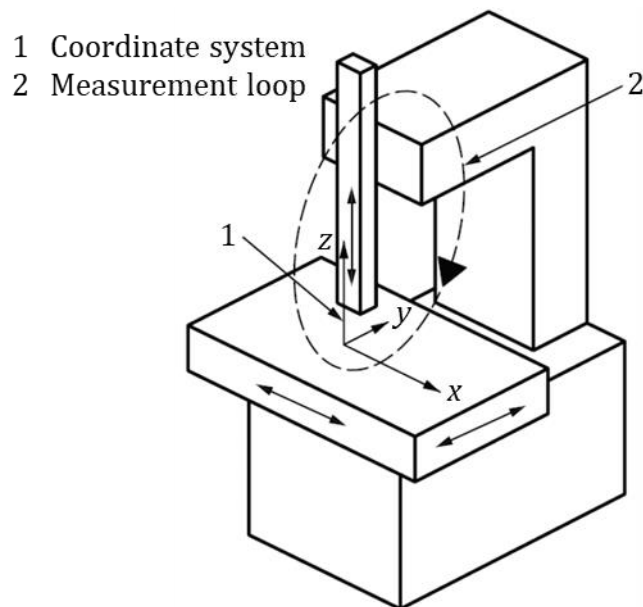


Figure 2.7 Coordinate system and measurement loop of an areal surface topography measurement instrument (adapted from [19]).

The coordinate system of a typical areal surface topography measurement instrument is defined as a right-handed orthogonal system of axes (x, y, z) [94], as shown in Figure 2.7. For optical instruments, the z -axis is oriented nominally parallel to the optical axis and is perpendicular to the (x, y) plane. The z -axis is

also referred to as the vertical axis, and the x - and y -axes are sometimes referred to as the horizontal axes. The measurement loop is a closed chain that comprises all components connecting the workpiece and the measuring probe [94].

2.2.3 Contact and non-contact methods

In general, methods for the measurement of surface topography can be distinguished in two types – contact and non-contact [90]. To obtain height information, contact methods rely on the mechanical interaction of a contact stylus with the surface to be measured; this interaction is well understood, allowing for robust models [25]. A stylus instrument essentially consists of a probing system that draws a contacting stylus along the surface, whose vertical motion is converted into an electrical signal that is subsequently digitised [95]. Further information about the general characteristics of stylus instruments is given in ISO 3274 [91] and ISO 25178 part 601 [96] specification standards.

Stylus instruments rely on a straightforward and intuitive measurement principle and are the most common instruments used in industry for surface measurement, however, there are some limitations to be considered [95]. The resolution of the detectable surface features is limited by the size of the stylus tip, which affects the measured topography and surface texture parameters [97, 98]. Also, if the stylus force is too high, the stylus tip may cause damage to the surface being measured, whereas smaller forces can induce ‘stylus flight’ (i.e. the stylus skips over the surface) [95, 99]. Another issue is that deep recesses and local high aspect-ratio features (relatively common on AM surfaces) could potentially block the stylus and damage it [13]. A downside of stylus instruments when areal measurements are performed is the total measurement time – while a profile measurement typically takes seconds or minutes, an areal measurement can take hours [25].

Unlike contact methods, non-contact methods avoid mechanical interaction with the surface throughout the measurement process, thus eliminating the risk of damaging the surface and allowing faster measurement times [98]. The most common type of non-contact methods are optical methods [24]. Optical methods use light reflected from a surface as a means to reconstruct surface topography. Although different optical principles can be used to obtain topographic data from

reflected light, interpreting data acquired with an optical instrument is not as simple as it is with a stylus instrument [25]. In general, optical methods require a significant amount of data processing to generate the measurement result. The characteristics of the incident light, as well as the geometry and material characteristics of the surface being measured have a significant effect on the result [98].

Many optical instruments use microscopy to magnify the topographic features of the measured surface. However, optical instruments using microscope objectives have two physical limitations – the numerical aperture (NA) and the optical lateral resolution of the employed microscope objective lens [25]. The NA dictates the slope angle limit on the surface that can be measured and has an impact on the optical lateral resolution [24, 100]. The NA is given by

$$A_N = n \sin(\alpha), \quad (2.1)$$

where n is the refractive index of the medium between the objective and the surface (usually air, at $n \cong 1$) and α is the acceptance angle of the aperture, as shown in Figure 2.8.

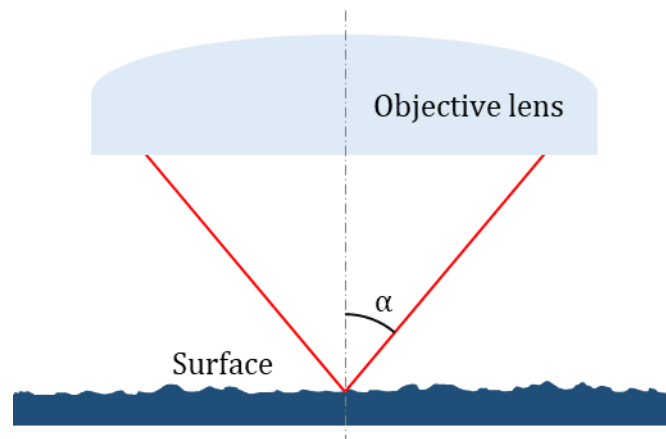


Figure 2.8 Diagram of the NA of a microscope objective lens.

The lateral resolution is the smallest distance between two lateral features on a surface that can be recognised [94]. For a theoretically perfect, incoherent optical system with a filled objective pupil, the optical lateral resolution given by the Rayleigh criterion [94, 100] is

$$r = 0.61 \frac{\lambda}{A_N}, \quad (2.2)$$

where λ is the effective value of the wavelength of the light used to measure a surface. Another measure of the optical lateral resolution is the Sparrow criterion, which is equal to $0.47 \lambda/A_N$ (approximately 0.77 times the Rayleigh criterion). Examples of optical methods include the following:

- Focus variation microscopy (FV) – Combines vertical scanning positioning with limited depth of focus to determine the surface height from the variation of focus for every lateral position along the surface. FV relies on an algorithmic assessment of local image contrast to detect in-focus points [20, 21].
- Confocal microscopy (CM) – Employs vertical scanning to acquire a sequence of confocal images through the depth of focus of the objective, where a pinhole acts as a spatial filter to block the light that is out of focus, enabling the surface topography reconstruction [22, 23].
- Phase-shifting interferometric microscopy (PSI) – Interference data acquired during a controlled phase shift is evaluated to reconstruct surface topography [27, 101].
- Coherence scanning interferometry (CSI) – Uses the low coherence of broadband light to localise interference fringes over a narrow surface height range during a vertical scan along the optical axis, where the height-dependent variation in fringe contrast provides a mean to determine the surface topography [18, 19] (CSI will be reviewed in more detail in Chapter 3).

There are several other methods for measuring surface topography. Examples of methods of the non-contact, non-optical type include scanning electron microscopy (SEM) and X-ray computed tomography (X-ray CT). SEM instruments usually provide two-dimensional topography images by focusing an electron beam on the surface and capturing the resulting electron emissions with a detector [25]. There are methods that have been developed to obtain three-dimensional surface topography from the analysis of SEM images [102]. In X-ray

Surface topography measurement for additive manufacturing

CT, a series of radiographic projections of the imaged part are obtained at multiple angular orientations. An algorithm is used to combine the projections into a volumetric dataset that represents the material density at different positions within the part. By analysing the volumetric dataset for changes in material density, the part surfaces can be reconstructed, and if the volumetric dataset has sufficient resolution, the surface topography as well [13, 103]. An example of a pseudo-contact method is atomic force microscopy (AFM). In AFM, a probe tip is placed so close to the surface that the attractive and repulsive interatomic forces can be sensed and used to reconstruct the surface topography [25, 90].

When using optical instruments to measure AM surfaces in their as-built state (see Figure 2.9), measurement challenges generally relate to surface regions exhibiting low reflectance or varying optical properties, high slope angles and undercuts. In general, the high complexity and irregularity of as-built AM surfaces can present significant issues for any type of measurement technique, requiring a careful selection of measurement conditions to minimise a number of common error sources [8, 9]. Therefore, it is necessary to develop basic knowledge on how to optimise the measurement of AM surfaces. A number of studies have recently been carried out to determine the optimal measurement conditions and settings that should be used when measuring AM surfaces with optical instruments, for example, with FV [76] and CSI (presented in Chapter 4).

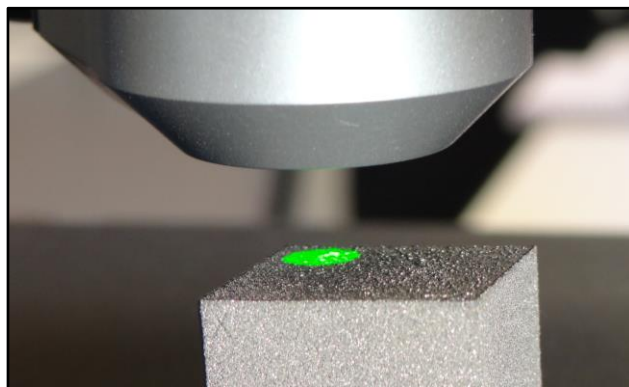


Figure 2.9 Surface measurement of an AM part using CSI.

It is worth highlighting that no single measurement technology provides a completely reliable rendition of the topographic features that characterise the metal AM process. In an investigation carried out by Nicola Senin and other

colleagues from the Manufacturing Metrology Team, a region of interest on a metal AM surface was inspected using different optical areal topography instruments [74]. Several smaller regions were extracted from the topography datasets to represent examples of relevant metal AM surface features, such as weld ripples, particles, recesses and weld tracks. Overall, it was found that when measuring metal AM surfaces, the most significant differences between these technologies relate to smaller-scale, high aspect ratio localised features. When the measurement task is the characterisation of large regions through the computation of texture field parameters, then the discrepancies between instruments may be considered to have limited effects on the characterisation results. However, when the measurement task is targeted at localised, smaller-scale features, which is often the case in off-line metrology for manufacturing process development and optimisation, then the discrepancies between both methods may become more significant.

For optical techniques, a combination of optical resolution, pixel width, and data processing used to obtain height information, leads to the final resolving power achievable by the instrument. For example, FV requires a window of adjacent pixels to compute contrast for any given pixel, therefore, it means that the heights of two adjacent pixels are not entirely independent, and consequently the actual lateral resolution of a FV instrument is poorer than that calculated by considering only pixel width and the optical resolution limit [74].

2.2.4 Areal surface texture characterisation

Filtering is fundamental for surface texture characterisation and its purpose is to separate the measured surface into different scales of interest [79, 104]. ISO 25178 part 2 [105] defines two surface filters – the S-filter and the L-filter. The S-filter removes small-scale lateral components (i.e. a low-pass filter in terms of spatial frequencies) from the surface, whilst the L-filter removes large-scale lateral components (i.e. a high-pass filter in terms of spatial frequencies) from the surface. Additionally, the F-operation removes the nominal form from the surface [79, 105]. Levelling is an F-operation used to compensate for surface tilts due to

sample placement within the measurement instrument, often performed by subtracting the mean least-squares plane from the topography dataset.

The combined application of these filtering operations to a measured surface results in one of the two defined scale-limited surfaces – the S-F surface and the S-L surface [79, 105]. An S-F surface is the outcome of using an S-filter in combination with an F-operation on a surface, whilst an S-L surface is the result of using an L-filter on an S-F surface. By default, the S-filter and the L-filter are areal Gaussian filters [106, 107]. The scale at which the S-filter and the L-filter operate is specified by the nesting index value (or cut-off wavelength) [106], which indicates the spatial wavelength at which the filter attenuates the amplitude of a signal by 50% [107].

The term ‘roughness’ is sometimes used to refer to the small-scale lateral components of surface texture, while the term ‘waviness’ is sometimes used to refer to the large-scale components of surface texture [13]. An example of the result of filtering operations applied to isolate the signature features on the topography of a metal AM surface is shown in Figure 2.10. In this example, an S-filter with a nesting index of 25 μm and an L-filter with a nesting index of 800 μm were applied.

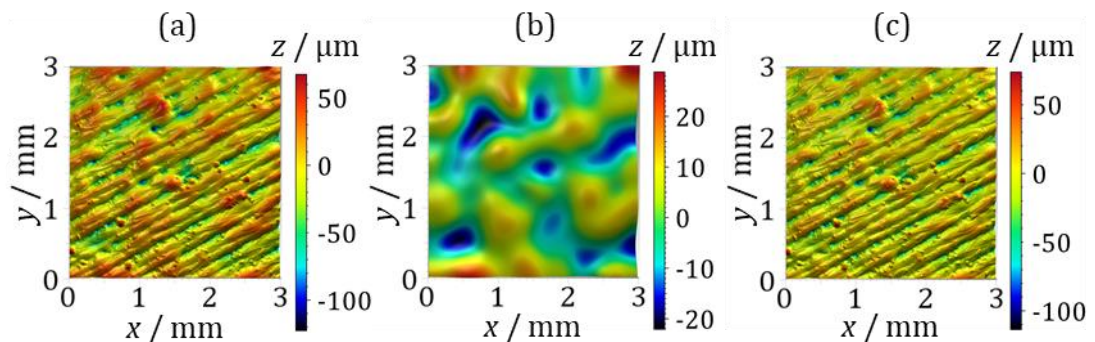


Figure 2.10 Filtering of a metal AM surface topography (a) original topography measured with CSI, (b) S-F surface showing the underlying large-scale waviness and (c) S-L surface showing weld tracks and spatter formations.

Surface texture parameters provide a quantitative value to the measured topography data of a surface, simplifying its description and comparison with other surfaces [25]. Areal surface texture parameters [105] were created as an evolution from profile surface texture parameters (such as R_a and R_q) [108],

extending surface texture characterisation to two-dimensional surface height measurements [109]. The two main classes of areal surface texture parameters are field parameters and feature parameters [25]. Field parameters are defined from all the topography data points on a scale-limited surface, whereas feature parameters are defined from a subset of predefined topographic features on a scale-limited surface [105]. The majority of areal parameters are field parameters, which are categorised in height parameters (e.g. Sa , Sq), spatial parameters (e.g. Sal , Str), hybrid parameters (e.g. Sdq , Sdr) and functional parameters (e.g. Spk , Svk) [79, 105].

The areal surface texture parameters used in this thesis are Sq and Sdq . These parameters were selected to obtain sufficient insight into the topography of the investigated surfaces, regarding not only height but also gradient. The Sq parameter is the root mean square (RMS) height of the scale-limited surface, corresponding to the RMS value of the surface height values $z(x, y)$ within a definition area A , such that

$$Sq = \sqrt{\frac{1}{A} \iint_A z^2(x, y) dx dy}. \quad (2.3)$$

The Sdq parameter is the RMS gradient of the scale-limited surface, given by

$$Sdq = \sqrt{\frac{1}{A} \iint_A \left[\left(\frac{\partial z(x, y)}{\partial x} \right)^2 + \left(\frac{\partial z(x, y)}{\partial y} \right)^2 \right] dx dy}. \quad (2.4)$$

2.2.5 Measurement uncertainty and error

The ‘true value’ of a measurand (i.e. the quantity intended to be measured) is the value that would be obtained by a perfect measurement, however, the true value cannot be determined by measurement as there is always some doubt about the measurement result [110]. The term used for the quantification of the doubt in the result of a measurement is ‘uncertainty’. The International Vocabulary of Metrology (VIM) defines measurement uncertainty as a ‘non-negative parameter characterising the dispersion of the quantity values being attributed to a

measurand, based on the information used' [111]. The parameter may be an estimated standard deviation of the mean called 'standard uncertainty' or a coverage interval having a stated coverage probability (also termed level of confidence). In practice, there are many possible sources of measurement uncertainty, for example:

- Inadequate knowledge of the effects of environmental conditions on the measurement, or imperfect measurement of environmental conditions.
- Finite instrument resolution.
- Inexact values of measurement standards, reference materials, values of constants and other parameters.
- Approximations and assumptions incorporated in the measurement method and procedure.

Measurement uncertainty components can be estimated by two methods: Type A and Type B evaluations. Whereas a Type A evaluation of measurement uncertainty is done by a statistical analysis of measured values obtained under defined measurement conditions, a Type B evaluation of measurement uncertainty is done by means of any other information, e.g. data provided in calibration and other certificates [110, 111].

The terms 'measurement uncertainty' and 'measurement error' are not equivalent. Measurement error is the difference between a measured value and a reference value of the measurand [111]. Every measured value has a measurement error; however, since there is always measurement uncertainty in a measured value, it is not possible to know the exact value of the measurement error. There are two types of measurement errors – random and systematic. Random measurement error is the component of measurement error that in repeated measurements varies in an unpredictable manner. Systematic measurement error is the component of measurement error that in repeated measurements remains constant or varies in a predictable manner [110, 111].

Random measurement errors arise from unpredictable or stochastic temporal and spatial fluctuations of influence quantities, which in turn give rise to variations in repeated measurements of the measurand [110]. An influence

quantity is a quantity that is not the measurand but that affects the result of the measurement. Although it is not possible to compensate for the random error of a measurement result, it can usually be reduced by increasing the number of measurements [110, 111]. The latter will be further discussed in Chapter 6. Systematic measurement error, like random measurement error, cannot be eliminated but it can usually be reduced. If a systematic measurement error arises from a known effect of an influence quantity, the effect can be quantified and a correction can be applied to compensate for it. The estimate of a systematic measurement error is known as the measurement bias [110, 111].

Other terms related to uncertainty and error are ‘measurement accuracy’ and ‘measurement precision’, as illustrated in Figure 2.11. Measurement accuracy is a qualitative term used to describe the closeness of agreement between a measured value and a reference value of a measurand [111]. Although measurement accuracy is not given a numerical value, a measurement result is said to be more accurate when the measurement error is smaller. On the other hand, measurement precision is the closeness of agreement between measured values obtained by repeated measurements under specified conditions [111]. Measurement precision is expressed numerically by measures of dispersion, such as standard deviation or variance and is used to define measurement repeatability and measurement reproducibility.

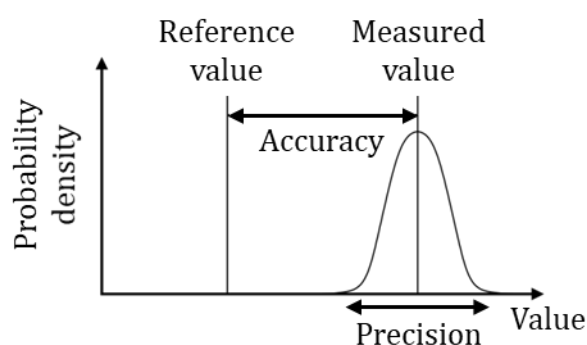


Figure 2.11 Illustration of the difference between accuracy and precision.

Accurate measurement enables quality control of manufacturing processes, compliance with laws and regulations, as well as research and development in science and engineering, therefore, it is essential that the level of accuracy is

appropriate for the intended application [110]. Ensuring measurement accuracy leads to the concepts of 'calibration' and 'metrological traceability'.

Calibration is the comparison of a measuring instrument, artefact or reference against a more accurate one, followed by the application of any necessary corrections to ensure that it is fit for purpose [111]. A calibration may be expressed by a statement, calibration curve, or calibration table. When performing a calibration, it is essential to have confidence in the higher accuracy reference; this confidence is provided by metrological traceability. Metrological traceability is defined by the VIM as the 'property of a measurement result whereby the result can be related to a reference through a documented unbroken chain of calibrations, each contributing to the measurement uncertainty' [111].

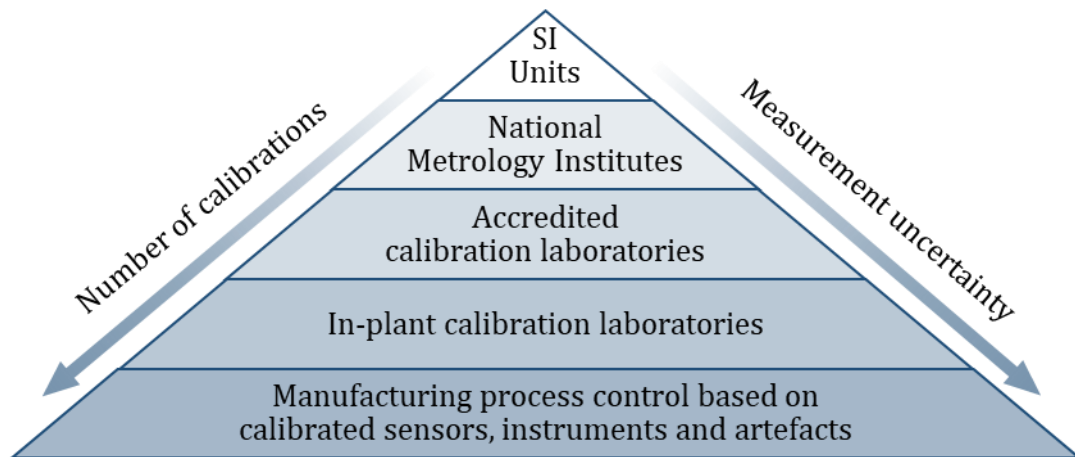


Figure 2.12 Calibration pyramid [112].

The documented unbroken chain of calibrations is often visualised by the calibration pyramid (shown in Figure 2.12), with the International System of Units (SI) located at the top. Usually, the measurement uncertainty and the number of calibrations are increased at every step going down the calibration pyramid [113]. The SI is essential to ensure that everyday measurements remain consistent and accurate throughout the world. The SI covers units for every type of measurement, but at the core of the SI is a set of seven units known as the 'base units'. These base units are: time, length, mass, electric current, thermodynamic temperature, amount of substance and luminous intensity [112].

2.2.6 Metrological characteristics for areal surface topography measurement

Evaluating measurement uncertainty for an areal surface topography measurement is highly complex [89, 114]. Intended to be feasible to apply in industry, the metrological characteristics provide a simplified, standardised approach for calibration and uncertainty evaluation for all (contact and non-contact) areal surface topography measuring instruments [89]. The metrological characteristics for areal surface topography measuring methods are listed in Table 2.1.

Table 2.1 Metrological characteristics in ISO 25178 part 600 [94].

Metrological characteristic	Symbol	Main potential error along
Amplification coefficient	$\alpha_x, \alpha_y, \alpha_z$	x, y, z
Linearity deviation	l_x, l_y, l_z	x, y, z
Flatness deviation	Z_{FLT}	z
Measurement noise	N_M	z
Topographic spatial resolution	W_R	z
x - y mapping deviations	$\Delta_x(x, y), \Delta_y(x, y)$	x, y
Topography fidelity	T_{FI}	x, y, z

As defined in ISO 25178 part 600 [94], a metrological characteristic is a ‘characteristic of measuring equipment, which can influence the results of a measurement’. The metrological characteristics are designed to include all of the factors that can influence a measurement result and they can be determined using appropriate procedures and material measures [113, 115, 116]. After assigning appropriate probability density functions to the metrological characteristics, their resulting statistical values can be propagated through a defined measurement model to evaluate the measurement uncertainty associated with the x , y and z measurements [115]. The ISO 25178 part 6XX series of specification standards describing the nominal characteristics of instruments identify for each type of surface topography measuring method a list of influence quantities and the

metrological characteristics affected by deviations of those influence quantities [19, 21, 23, 96, 101, 117, 118].

The draft ISO/DIS 25178 part 700 standard [119] specifies generic procedures and material measures for the calibration, adjustment and verification of areal topography measuring instruments, and for the determination of the metrological characteristics defined in ISO 25178 part 600. For example, a method for determining the amplification coefficient and the linearity deviation of the z -axis consists in measuring calibrated step height artefacts, while the x - y mapping deviations can be determined by using areal cross grid artefacts. The specifications of the material measures are provided in ISO 25178 part 70 [116]. This standard does not mandate the use of the specified material measures, therefore, users may use any appropriate material measure as long as all relevant details are clearly indicated. The National Physical Laboratory (NPL) has recently developed a single-wafer artefact designed to calibrate areal surface topography measuring instruments [120].

A second application of the metrological characteristics is for instrument performance specification [89, 121]. One of the most important quantifiers for measurement performance is measurement noise [121, 122]. In this thesis, the motivation of the focus on measurement noise is that the ability of an instrument to capture data is significantly affected by noise, therefore, the evaluation of this metrological characteristic becomes highly relevant when investigating new challenging applications, such as in the measurement of AM surfaces. Other metrological characteristics where not considered as instrument calibration and uncertainty analysis are beyond the scope of the presented work.

2.2.6.1 Measurement noise

ISO 25178 part 600 [94] defines measurement noise as the ‘noise added to the output signal occurring during the normal use of the instrument’. Measurement noise includes the instrument noise (i.e. internal noise added to the output signal caused by the instrument if ideally placed in a noise-free environment) as well as components arising from the environment (e.g. vibration, air turbulence, thermal instability, acoustics) and other sources [94]. Figure 2.13 illustrates the typical

sources of noise and the distinction between instrument noise and measurement noise. The instrument noise is approximated by the minimum achievable measurement noise value with an ideal part (the default material measure is an optical flat) under ideal conditions and is often used for instrument performance specification [115, 121]. In CSI, instrument noise has often been confused with the terms ‘axial resolution’ and ‘vertical resolution’. These terms are somehow irrelevant for surface topography measurement, as there are no adjacent points to be resolved in the axial/vertical direction when only the outer surface of a part is of interest.

In practice, measurement noise is expected to be greater than instrument noise due to the contributions from environmental disturbances and effects specific to the optical properties or topographical features of an object surface; therefore, meaningful statements of measurement noise are closely tied to the specifics of the measurement task [110]. Because noise is a bandwidth-related quantity [123], its magnitude also depends on the time over which it is measured or averaged [94]. To allow comparison with other results, any measurement noise values should be accompanied by a data acquisition time or bandwidth, the number of independent data points and any filtering of the surface topography [122, 124].

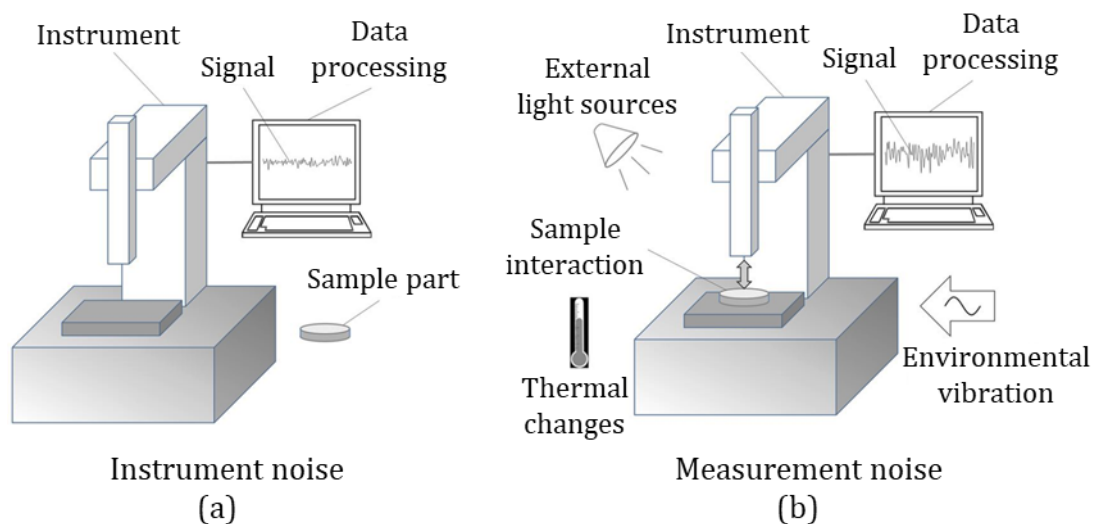


Figure 2.13 Illustration of the distinction between (a) instrument noise and (b) measurement noise, adapted from [94].

The evaluation of the surface topography repeatability is a common approach for estimating measurement noise [94]. The surface topography repeatability

Surface topography measurement for additive manufacturing

provides a measure of the likely agreement between successive measurements of the same surface topography under the same conditions of measurement, normally expressed as a standard deviation [94]. A procedure for estimating the surface topography repeatability using an optically smooth surface is included in ISO 25178 part 604 [19] (although there is no default material measure for measurement noise). This procedure is equivalent to the subtraction method used for the estimation of measurement noise [125-127], which will be described in Chapter 6. Measurement noise can vary significantly with different surface types (in terms of topographies and material reflectance properties), therefore it should be determined using the surface being measured [115].

3 Coherence scanning interferometry

3.1 Introduction to CSI

Interferometry employs the ability of two waves (e.g. light) to interfere with one another provided certain criteria of coherence are met, and it allows a length to be measured in terms of the wavelength of light [128]. Indeed, the definition of the metre, the SI unit of length, can be realised in practice by interferometry. The metre is defined by taking the fixed numerical value of the speed of light in vacuum, c , to be 299 792 458 when expressed in the unit m s^{-1} , where the second is defined in terms of the caesium frequency $\Delta\nu_{\text{Cs}}$. This definition implies that ‘The metre is the length of the path travelled by light in vacuum during a time interval of $1/299\,792\,458$ of a second’, as it was stated in the previous definition of the metre, which was in place since 1983 [112].

In a typical two-beam interferometer, a light beam is split into two light beams, which travel separate paths and then recombine to create interference. The physical distance of the path travelled by a light beam multiplied by the index of refraction of the traversed medium is known as optical path length (OPL) or optical distance. When the optical distances differ by an even number of half-wavelengths, the superposed light beams are in phase and constructive interference will be observed, but when the optical distances differ by an odd number of half-wavelengths, the combined light beams are 180° out of phase and destructive interference will be observed. The resulting interference fringe pattern when viewed on a screen or through a microscope will be defined by the phase difference between the two light beams, which can be used for the measurement of length if the wavelength is known [26, 129, 130].

Interference microscopes used for surface measurement operate by comparing the object surface to a reference surface by two-beam amplitude division interferometry [131]. A fundamental characteristic of interferometric surface measurement is that the measurement sensitivity in the axial direction is

independent of lens magnification (or NA), in contrast to other optical methods relying on focus [28]. This characteristic is related to the use of the wavelength of light as a metric for length measurement, rather than the focus position. The currently dominant interferometric methods for the measurement of areal surface topography are PSI and CSI. While conventional PSI can provide accurate and repeatable measurements of smooth surfaces, it becomes ineffective when measuring rough or discontinuous surfaces because phase detection is inherently ambiguous outside of a 2π range [131]. A defining feature of CSI with respect to PSI is that, by design, interference fringes are only strongly observed over a narrow surface height range, therefore avoiding 2π ambiguity and allowing interferometric measurements for a wider range of surfaces, from smooth to rough, and surfaces that have large height variations or discontinuities [29, 132]. The development of automated three-dimensional measurement of surface topography using CSI began in the 1980s [19]. In 1982, Balasubramanian [133] patented an interferometric system that relies on identifying the maximum contrast of broadband or 'white' light interference fringes corresponding to zero optical path difference (OPD) as a means to determine surface topography. In 1987, Davidson et al. [134] applied the idea of calculating the degree of coherence for each pixel between the object and reference image planes of an interferometric microscope during a vertical scan to produce high-resolution three-dimensional images of smooth surfaces for semiconductor applications. During the 1990s, several researchers demonstrated that CSI was not limited to the measurement of smooth surfaces, but could also be used to measure rough surfaces [135-141]. Today, CSI has evolved to enable highly flexible areal surface topography measurements that would otherwise be beyond the reach of interference microscopy, and its development continues [28].

CSI is also sometimes referred to as white light interferometry, white light scanning interferometry or vertical scanning interferometry, amongst other recognised terms in ISO 25178 part 604 [19]. While modern CSI instruments use a variety of optical configurations and signal processing methods to reconstruct surface topography, the basic idea shared by all CSI instruments is the evaluation of the height-dependent variation in fringe contrast related to optical coherence

in an interferometric microscope [18]. The working principles of CSI are described in the following section.

3.2 Working principles

3.2.1 Configuration

The basic features of a conventional CSI instrument include a light source, an interference objective, an electromechanical scanner, an electronic camera and computer-controlled data acquisition and processing. Figure 3.1 illustrates the typical configuration of a CSI instrument.

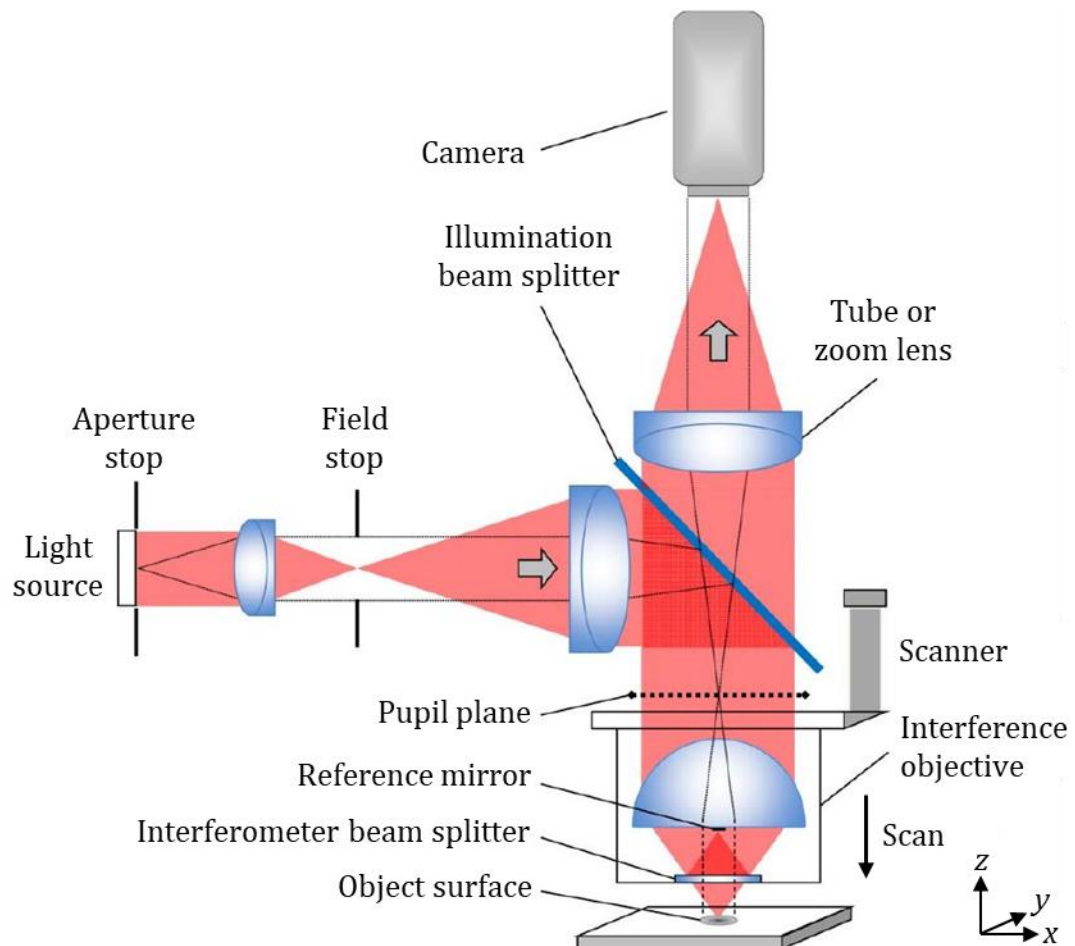


Figure 3.1 Schematic of a CSI instrument, adapted from [29].

CSI uses a spatially extended, spectrally broadband light source, which has a lower temporal coherence than a monochromatic light source. Temporal coherence

characterises how well a wave can interfere with itself at different points along the direction of propagation (i.e. at a different time) [129]. While a classic example is an incandescent lamp such as a tungsten halogen bulb, the most common light source in modern CSI instruments is a light-emitting diode (LED) [18]. Typically, Köhler illumination is used to image the light source into the pupil of an interference objective [19]. CSI instruments generally have adjustable light stops for controlling the size of the illumination field (i.e. field stop) as well as the illumination aperture (i.e. aperture stop), as shown in Figure 3.1. The optics are often arranged to fill the pupil so as to minimise spatial coherence and to maximise lateral resolution [18].

Generally, data acquisition in CSI involves the continuous motion of the position of the interference objective along the z-axis direction. A scanner, such as a piezoelectric transducer, moves the interference objective (see Figure 3.1), synchronising the scan of focus and OPL; in other cases, the object stage moves [19].

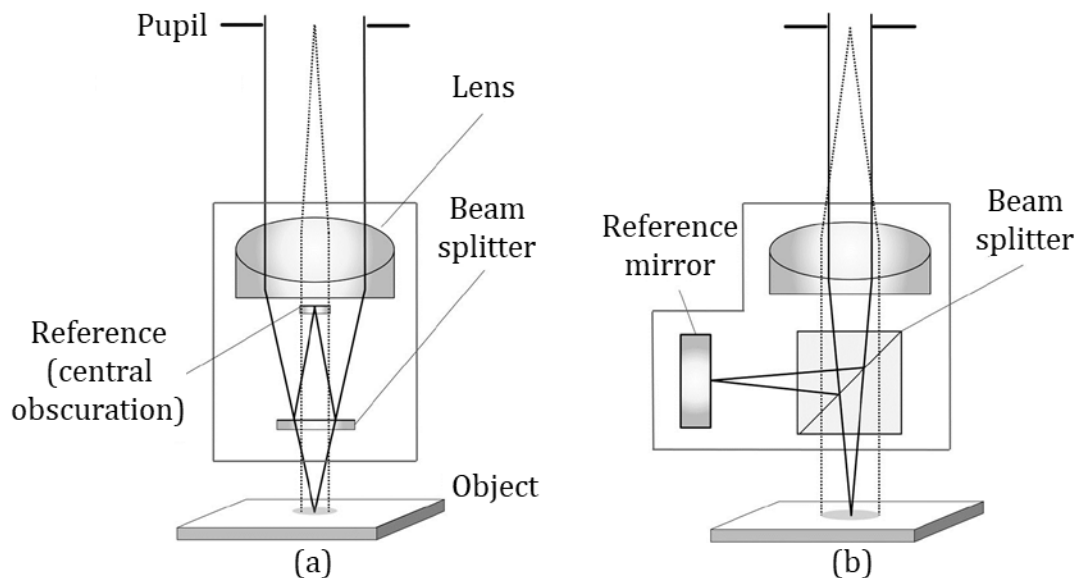


Figure 3.2 Schematic of interference objectives typically used for CSI. (a) Mirau and (b) Michelson type, adapted from [142].

CSI instruments often allow for interchanging interference objectives of various magnifications and types, where two of the most common are of the Mirau and Michelson type [31], shown in Figure 3.2. The interference objectives must have a geometry carefully balanced for minimal dispersion and best focus at the position

of zero OPD [18, 19]. The Mirau interference objective has coaxial lens, beam splitter and reference mirror, where the latter partially obscures the light path. The Mirau design inherently has a compact package and is preferred for high magnification objectives, ranging from 10× to 100×; however, at magnifications lower than 10× (corresponding to smaller NA values) the central obscuration blocks too much of the light [142, 143]. A preferred option for magnifications lower than 10× is the Michelson configuration, which uses a beam-splitting cube prism and a reference path that is orthogonal to the measurement path. Since the Michelson design has no central obscuration as in the case of the Mirau design, it allows for smaller NA values [142, 143].

3.2.2 Signal formation

With reference to Figure 3.1, the light emitted from the broadband light source is directed towards the interference objective lens. The beam splitter in the objective divides the light into two separate beams, one of which is directed towards the object surface while the other is directed towards the reference mirror. The two beams recombine and the recombined light is directed towards the electronic camera [18, 19, 29]. For interference to be observed, the OPL from the beam splitter to the object surface and the OPL from the beam splitter to the reference must be almost equal [18, 25]. The localisation of the interference fringes can be performed by vertically moving the interference objective lens at a constant speed, relative to the object surface (i.e. axial scanning), as illustrated in Figure 3.3.

During the axial scanning, a high interference fringe contrast will be observed for each camera pixel only when the OPD is near to zero, within the coherence length of the broadband light source. The coherence length can be thought as the maximum OPD over which it is still possible to obtain interference [144], sometimes estimated as

$$l_c = \frac{\lambda^2}{\Delta\lambda}, \quad (3.1)$$

where λ is the source effective wavelength and $\Delta\lambda$ is the spectral bandwidth. At the scan position of zero OPD, the fringe contrast is maximum, denoting the height of the corresponding point on the object surface. Moving away from the scan position of zero OPD, the fringe contrast decreases as the OPD increases. A computer records the low-coherence interference signal as a function of the scan position for each pixel in successive camera frames, which can be processed to reconstruct a three-dimensional topography map of the object surface [18, 19, 25].

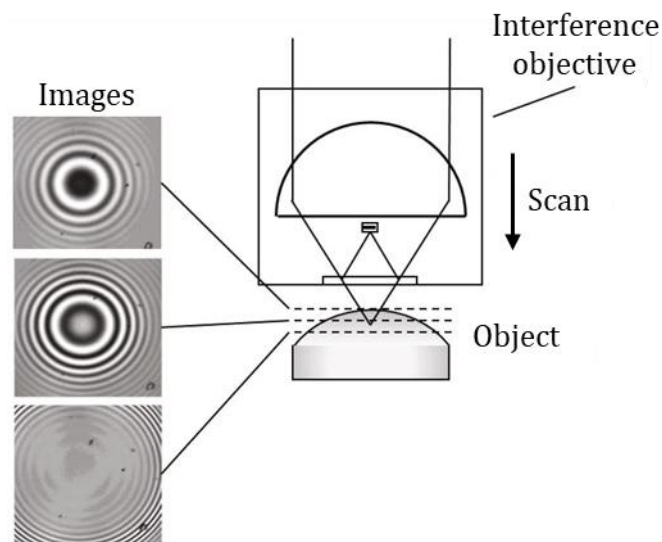


Figure 3.3 Appearance of low-coherence interference fringes during the axial scanning process (adapted from [18, 145]).

A simplified one-dimensional physical model of signal formation assumes a randomly polarised, spatially incoherent illumination and a smooth surface that does not scatter or diffract the incident light [18]. The low-coherence signal results from the incoherent superposition of individual interference contributions spanning a range of wavelengths of all the ray bundles reflecting from the object and reference surfaces and passing through the pupil plane of the objective. As illustrated in Figure 3.4, the peak signal strength is located at the position where all of the individual interference contributions are in phase [146].

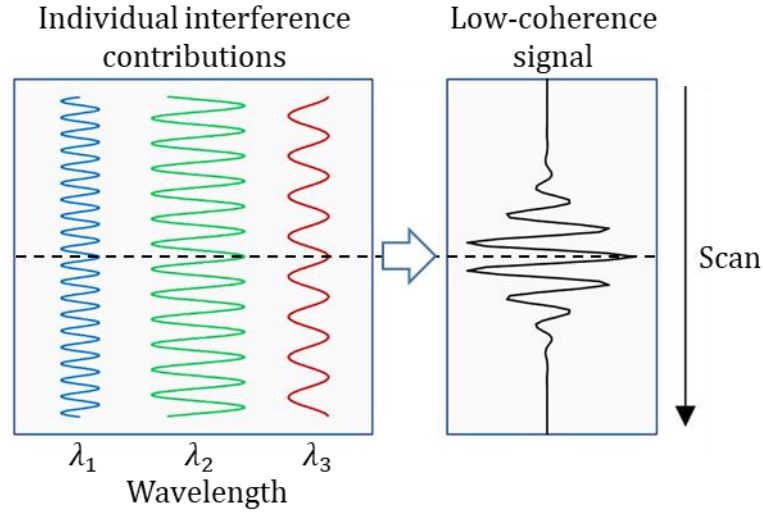


Figure 3.4 Conceptual diagram of the signal formation by incoherent superposition, adapted from [29].

For the ideal case of a flat, unstructured surface that is normal to the optical axis of the instrument and a low NA objective, the intensity of the interference signal along the vertical scanning direction $I(z)$ at a given pixel can be expressed mathematically as

$$I(z) = I_0[1 + \gamma g(z - h) \cos(\tau)], \quad (3.2)$$

where I_0 is a constant offset intensity term, γ is the fringe contrast, $g(z - h)$ is the modulation (or coherence) envelope function related to the spectral distribution of the light source, z is the scan position, h is the height of the object surface and τ is the phase difference between the two interfering beams, given by

$$\tau = K_0(z - h) + \nu, \quad (3.3)$$

where $K_0 = 4\pi/\lambda_0$ is the spatial fringe frequency corresponding to the mean effective wavelength λ_0 and ν is the phase offset related to the effects of dispersion in the optical system and the phase change on reflection introduced by the surface material. For a light source with a Gaussian spectral distribution,

$$g(z - h) = \exp\left[-\left(\frac{z - h}{l_c}\right)^2\right], \quad (3.4)$$

where l_c is the coherence length of the light source. Therefore, Equation (3.2) can be rewritten as

$$I(z) = I_0 + \gamma I_0 \exp \left[- \left(\frac{z - h}{l_c} \right)^2 \right] \cos \left[\frac{4\pi}{\lambda_0} (z - h) + \nu \right]. \quad (3.5)$$

When the phase offset ν is ignored, the peak signal strength occurs at the scan position corresponding to zero OPD. A typical CSI signal for a single camera pixel as a function of the axial scan position of the objective is shown in Figure 3.5.

In general, the formation of the interference fringes not only depends on the light source spectral bandwidth but also on the NA of the objective lens, as in combination they limit both the temporal and spatial coherence [146, 147]. For a high NA, the coherence properties are determined mainly by the light distribution in the pupil plane, rather than by the spectrum of the light source [18].

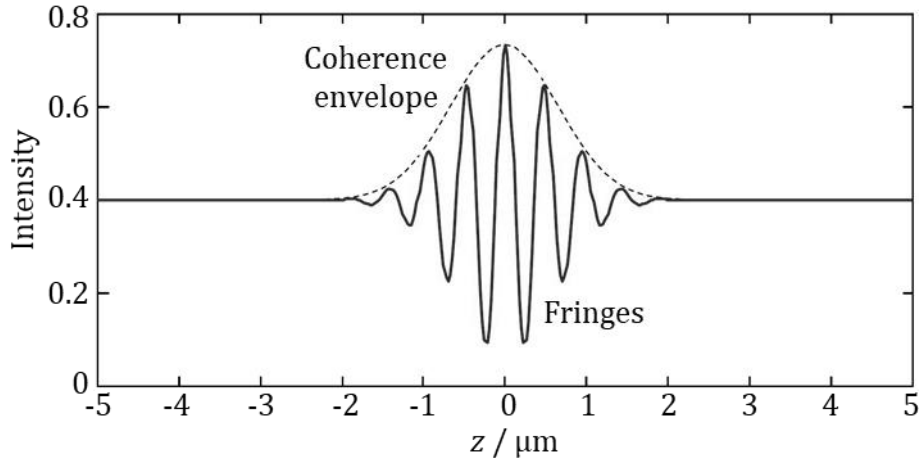


Figure 3.5 CSI signal for a single camera pixel as a function of scan position z showing the coherence envelope (adapted from [28]).

Although the one-dimensional incoherent superposition model does not include the effects of light scattering by the object surface and the effects of aberrations in the optical system, it provides insight into the main characteristics of the interference signal generated in CSI and a starting point for many surface topography reconstruction methods based on coherence envelope detection [18, 146].

As an optical imaging system, the capability of CSI for resolving fine structures of a surface follows the Abbe theory of image formation, i.e. the scattered/diffracted light needs to be captured within the pupil of the objective to provide a resolved image [148, 149]. A two-dimensional elementary Fourier optics (EFO) model for

topography measurement in interference microscopy that includes the imaging properties of optical systems with partially coherent illumination has been recently reported by de Groot and Colonna de Lega [150]. The EFO model can be used for predicting the instrument response to surfaces having topography variations within the depth of field (given by the wavelength divided by the square of the NA), and can be useful for understanding how physical apertures and optical aberrations influence spatial frequency response [148, 150]. CSI models using three-dimensional imaging theory in combination with an appropriate surface scattering model have also been developed [151, 152]. For example, under the Kirchhoff approximation [153] (i.e. the radius of curvature of the surface is much larger than the wavelength), Su et al. [154] have recently demonstrated that image formation in CSI can be characterised by its three-dimensional surface transfer function. The latter provides information about the instrument spatial frequency response and about lens aberrations that can result in measurement errors.

3.2.3 Surface topography reconstruction methods

Various methods have been developed for reconstructing surface topography from the low-coherence interference fringes, each having advantages with different surface types and measurement requirements. Generally, surface height in CSI is determined either by coherence envelope detection [135-141], or a combination of coherence envelope detection with phase estimation [155-160]. For low-coherence interference fringes, the peak contrast corresponds to the position of zero OPD (in an ideal interference objective perfectly compensated for dispersion); hence, a basic approach to determining surface topography is to locate the scan position for which the signal strength or interference fringe contrast is maximum, sectioning surface images according to surface height [133, 134]. Another approach to evaluate fringe contrast is to demodulate the coherence envelope of the interference signal and detect its peak [138]. A Fourier transform technique can be used to filter out the high spatial frequency components to obtain the coherence envelope [140]. Digital filtering to extract the envelope can also be achieved by using a Hilbert transform algorithm [141, 161].

A more robust alternative to the application of a simple peak detection process to the coherence envelope is to estimate the overall signal position using the centroid of the square of the signal derivative [157, 162, 163]. Envelope detection does not require phase information, therefore is free of height range limitations related to 2π ambiguity, making it an effective method for surface topography measurement on both smooth and rough surfaces [138, 140]. However, when applied to smooth surfaces, envelope detection suffers from sensitivity to noise to a greater degree than interference phase techniques (e.g. PSI) [29, 160].

Envelope detection can be combined with phase estimation to achieve a more precise estimate of surface height on smooth surfaces, since the interference fringes themselves have a higher spatial frequency content than their coherence envelope [155-160]. In a combined approach, CSI data is first evaluated using envelope detection to resolve the fringe order, with the phase estimation then being applied to determine the surface height [164]. The coherence-based analysis leads to a first estimate of surface height h' , while the phase analysis provides the interference phase value θ corresponding to the fringe frequency K_0 . The two analysis can then be combined to determine the final surface height value h , in such a way that

$$h = \frac{\theta}{K_0} + \frac{2\pi}{K_0} \text{round} \left(\frac{\phi_G - \langle \phi_G \rangle}{2\pi} \right), \quad (3.6)$$

where ϕ_G is the phase gap between the two different analysis defined as $\phi_G = \theta - K_0 h'$, $\langle \phi_G \rangle$ is the field average of the phase gap ϕ_G and the function $\text{round} ()$ returns the nearest integer value [18, 165].

An alternative method for determining surface topography is to analyse the interference signal $I(z)$ in the spatial frequency domain via a Fourier transform [164-166], such that

$$P(K) = \int_{-\infty}^{\infty} I(z) \exp(-iKz) dz. \quad (3.7)$$

The phase for the corresponding fringe frequency K is then given by

$$\phi(K) = \tan^{-1} \left(\frac{\text{Im}\{P(K)\}}{\text{Re}\{P(K)\}} \right), \quad (3.8)$$

where $\text{Im}\{P(K)\}$ and $\text{Re}\{P(K)\}$ are the imaginary and real values of the Fourier transform $P(K)$, respectively. This approach is known as frequency domain analysis (FDA) [164, 165]. After obtaining the phase values from the Fourier transform, a linear least squares fit weighted by amplitude can be applied to estimate the phase slope, as illustrated in Figure 3.6. Therefore, the surface height value can be determined from the rate of change of phase with fringe frequency $d\phi/dK$.

Whilst the incorporation of phase estimation provides a better resolution of surface height, it can potentially introduce a fringe order ambiguity (i.e. 2π errors) [167]. When measuring rough surfaces at scales less than the lateral resolution of the microscope objective, the phase of the fringe data may not correlate well with the surface profile and consequently random jumps in the fringe data may be observed, leading to a misclassification of fringe order [18, 30]. For this reason, the potential for additional precision in the axial direction provided by phase estimation may not be exploited in the measurement of rough surfaces [29, 30]. The selection of an appropriate surface topography reconstruction method for a given application should be made by choosing the one with the optimal strengths and least weaknesses for the specific measurement task [168, 169].

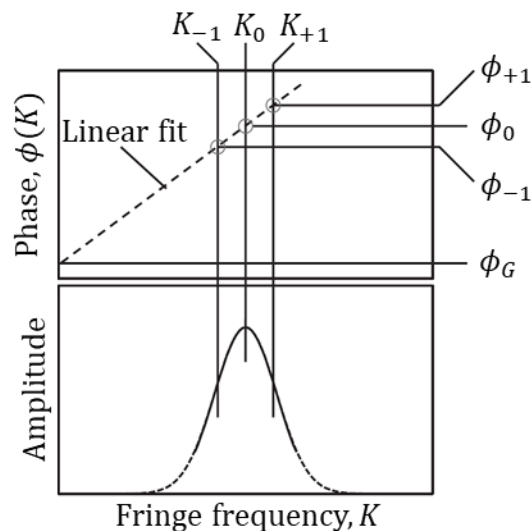


Figure 3.6 Illustration of the FDA method, adapted from [131].

Regardless of the employed fringe analysis method, it is worth highlighting that real fringe data is likely to deviate from the ideal form for reasons including surface tilt, roughness, measurement noise, aberrations and dispersion introduced by the objective lens, different phase changes on reflection and multiple scattering effects, which can lead to measurement errors [30, 170]. The following section describes the aforementioned issues.

3.3 Considerations and characteristic errors

Although CSI can measure flat surfaces with sub-nanometre precision along the direction of surface height [29, 31], the measurement noise may increase when measuring steeply sloped surfaces [171, 172], or surfaces with low reflectance or significant surface roughness [32, 173].

A low signal-to-noise ratio (SNR) may cause data dropout (i.e. missing data points) and is usually a sign that the instrument is working near to (or beyond) the limits of its specification [30]. Typically, data dropout may occur when measuring high slope surface features or weakly reflecting surface regions (common with AM surfaces), as shown in Figure 3.7. More obviously, shadowing effects when measuring re-entrant features or undercuts will cause data dropout. Alternatively, the measurement of such surface features and regions may result in outliers, which fail to be identified as dropouts and result in errors in the reported surface topography [19]. Data dropout and outliers can lead to biased estimates of surface texture parameters [19, 30].

Fringe modulation is expected to decline as a function of surface tilt. For smooth surfaces, the reflected light rays follow a specular behaviour, therefore, as the surface tilt increases, progressively less of the reflected rays are collected by the objective lens; if the surface tilt is beyond the slope angle limit given by the NA, none of the reflected rays will be collected by the objective lens [30]. When light is reflected from a rough surface, the specular behaviour is relaxed and light rays are scattered broadly, hence only a portion of the scattered light will be collected by the objective lens. However, because the light is scattered over a larger range

than the specular reflection angle, it is possible to measure rough surfaces at tilts that exceed the slope limit angle given by the NA of the objective [30].

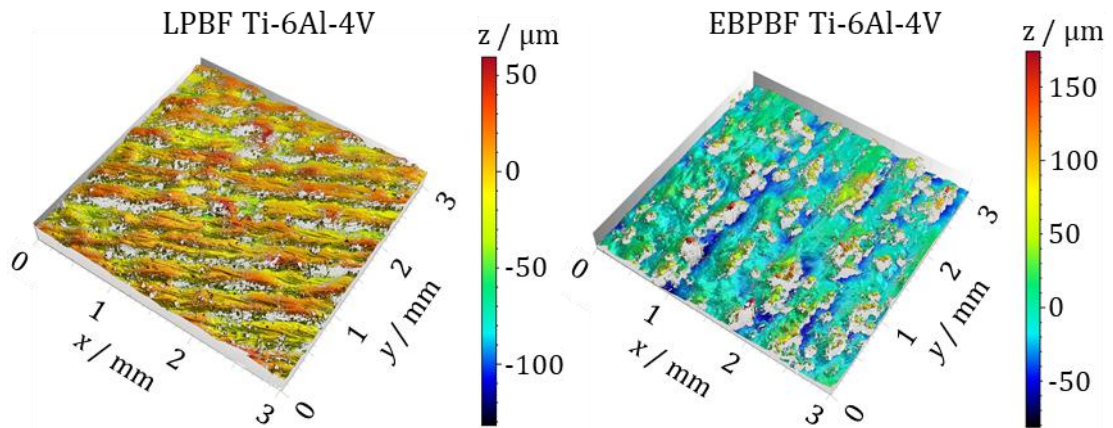


Figure 3.7 CSI measurements of metal AM surfaces with several missing data points over regions featuring high slopes and deep recesses. A $5.5\times$ lens ($0.5\times$ zoom) was used.

Using any particular objective lens will have a consequence on the optical parameters. An objective lens with a higher magnification (usually with higher NA) provides a higher lateral resolution and a higher slope limit [174], but a smaller field of view (FOV) [30, 31]. The camera pixel size divided by the objective lens magnification will determine the lateral sampling interval (i.e. the pixel size on the target surface) [19]. To maximise the diffraction-limited lateral resolution, the lateral sampling interval must match or exceed the optical lateral resolution, otherwise the lateral resolution will be camera limited [19, 131]. The camera array size (i.e. the number of camera pixels) and the lateral sampling interval will determine the overall FOV [131]. From a practical point of view, the measurement of steep slope features, rough surfaces or a higher resolution analysis generally requires higher magnification lenses. In contrast, the measurement of flat and smooth surfaces, a lower resolution analysis or a larger FOV generally requires lower magnification lenses. The measurement of larger areas on the surface can be achieved using a field-stitching function [29, 30].

Typically, CSI instruments employ a broadband light source with a bandwidth of between 50 and 150 nm corresponding to a typical coherence length of $\sim 3\ \mu\text{m}$, which is suitable for acquiring data from most surfaces. However, rough surfaces may cause a CSI instrument to be prone to data dropout (see Figure 3.7), as the

signal strength becomes low if the range of topographical surface heights within the imaging area of a single pixel is larger than the coherence length [30, 144]. Since the bandwidth of the source spectrum is inversely proportional to the coherence length, by narrowing the bandwidth, data lost due to inadequate signal strength may be captured as the coherence length is increased. The bandwidth of the source spectrum can be adjusted either through the use of bandwidth narrowing filters, or through the use of multiple sources of different bandwidths [30]. However, this technique will also broaden the coherence envelope, consequently increasing the measurement uncertainty [30].

The need to perform mechanical scanning (of either the probe head or the object stage) not only limits the measurement speed of CSI, but it can also introduce scanner-induced errors corresponding to departures from the nominal scan speed [18, 167]. Moreover, since CSI measurements rely on data acquisition over time, other time-dependent phenomena such as mechanical vibrations can affect the acquired data, degrading measurement accuracy. Therefore, the environment can be an important contributor to measurement error [18]. Instruments based on interferometry are typically equipped with systems to dampen or isolate unexpected mechanical motions, helping to reduce vibration sensitivity [131, 175]. While low-frequency vibrations are associated with form errors, high-frequency vibrations can contribute to ripple errors [175, 176]. Changes in temperature, pressure and humidity can cause variations in the index of refraction of the air, altering the wavelength of the source and consequently the OPL, which may contribute errors in the measurement if not compensated [30].

The mechanisms responsible for 2π or fringe order errors are varied. Field-dependant dispersion introduced by imperfections in the optical system can cause a varying offset between the phase and envelope peak across the FOV of the system (sometimes referred to as phase gap) [164, 167]. In turn, this effect can cause random jumps to a higher or lower order fringe (i.e. 2π errors), resulting in a discontinuity of approximately one-half the mean effective wavelength of the light source in the estimate of surface height [170, 177, 178]. For surfaces having varying optical properties, e.g. surfaces composed of dissimilar materials, errors in topography measurement can be introduced by different phase changes on

reflection [179, 180]. Moreover, phase changes can combine with dispersive effects and give rise to 2π errors [31].

In addition to dispersion, the retrace error [181, 182], the effects of defocus [183], lateral distortion [184], along with other high order optical aberrations are accountable for tilt-, curvature- and spatial frequency-dependent errors in surface measurement with CSI [154].

The 'batwing effect' is a measurement error that can occur around a step-like discontinuity (e.g. sharp edges) in a surface [30, 170, 185]. This error is referred to as batwing because of its appearance when the measurement result is plotted, and is usually explained as the interference between reflections of waves normally incident on the top and bottom surfaces following diffraction from the discontinuity, causing the envelope of the CSI signal to skew and the peak to shift [185, 186].

Multiple scattering represents a fundamental limitation to CSI [30]. Measurement errors can result when light is scattered more than once from the surface of interest before it is collected by the objective [170]. The effects of multiple scattering are most apparent when measurements are attempted on multifaceted steep sided surfaces such as vee-grooves, sharp edges and re-entrant features [170, 187].

3.4 Applications and technical advances

CSI has found broad applications in the semiconductor, optics, biomedical, energy, automotive, and aerospace industries. Examples of these applications include the characterisation of micro-lenses [188, 189], micro-tools [190], micro-electromechanical devices [191, 192], extreme-ultra violet lithography [193], fuel injection systems [194] (see Figure 3.8), turbine blade surfaces [195], multi-layer drug-delivery structures [196], cartilage cells [197], biomimetic layers [198], additively manufactured components [75, 199-201], as well as applications involving the measurement of transparent films and dissimilar materials [202-204]. With the benefits of recent technical advances, CSI is able to meet the

demanding surface metrology requirements of these industries and an increasing number of new applications [28, 149].

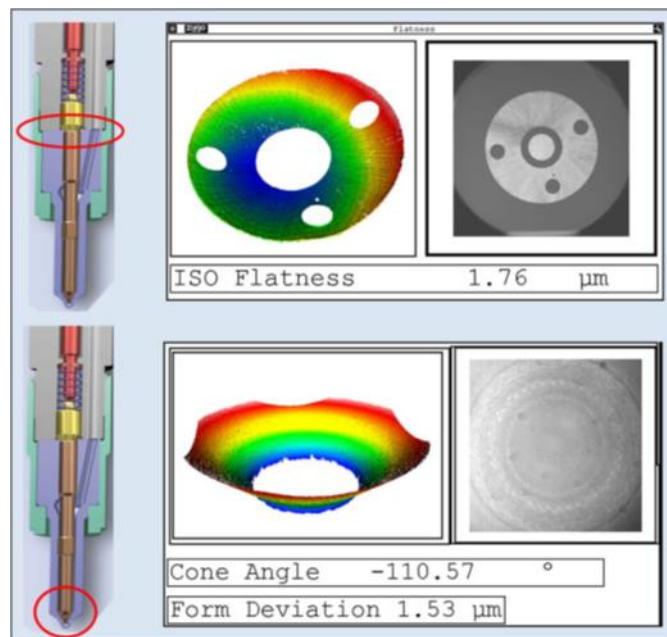


Figure 3.8 Example of an application of CSI for the measurement of automotive fuel injectors. Deviations outside tolerance can lead to reduced fuel efficiency and unacceptable emissions (adapted from [194]).

As mentioned in Section 3.3, a conventional CSI measurement may lose data coverage for surface regions featuring high slopes and low reflectivity; nevertheless, the missing data may be detectable if the measurement is sufficiently sensitive. A technique for enhanced sensitivity consists in sampling at smaller phase increments to increase the number of camera acquisitions over each interference fringe, leading to a dynamic noise reduction [188]. This method is sometimes referred to as oversampling [29]. Increasing the number of camera acquisitions over each fringe can improve the SNR, which in turn can significantly increase the number of valid data points for CSI measurements of surfaces with low reflectance or surfaces presenting high roughness and steep slopes [75].

When performing a CSI measurement, the intensity level of the light source is adjusted to avoid sensor saturation and hence is driven by the highest reflectance region on the investigated surface [30]. However, this strategy may have a negative impact when measuring regions with low reflectance features and high slopes, which are already prone to data dropout due to a weak signal strength. To overcome this issue, Fay et al. [188] proposed to use a high dynamic range (HDR)

measurement strategy. In this HDR approach, multiple exposures are collected in sequence, with either varying light intensity levels or exposure times, and a composite image is created from the image data with the highest SNR, commonly gauged by the contrast that each pixel has in comparison to its neighbours. Therefore, HDR can be used to optimise signal strength when measuring surfaces with a large variation in reflectance and slope, such that the number of missing data points may be reduced [75].

Wiesner et al. [205] proposed a method to reduce the effect of speckle on measurement uncertainty and the number of outliers when measuring rough surfaces. By sequentially switching the direction of the illumination, the camera captures several independent speckle patterns in sequence. From each pattern, only the brightest speckles are evaluated to determine the surface topography, since a bright speckle yields a smaller measurement error than a dark speckle.

With some modifications to the common surface topography reconstruction methods described in Section 3.2.3, several advanced algorithms using data filtering and fitting techniques have been recently developed for better robustness to noise [206-209], to reduce the batwing effect [210, 211] and to improve accuracy when measuring curved or tilted surfaces where errors can occur due to inconsistencies between the phase and envelope peak [212]. One approach developed for robust surface evaluation in the presence of uncorrelated noise is the correlogram correlation method, which consists in searching for the position of optimal fitting of a reference correlogram to the measured correlogram by using a cross-correlation function and then associating the position of maximum correlation with the surface height [213, 214]. Earlier work on the latter approach can be found in references [215, 216].

Various approaches have been developed to simultaneously determine surface topography and thickness of transparent films [217-221]. One approach consists in generating a library of model signals over a range of possible film parameters and comparing these library entries to the experimental signal to find the best match. To determine film thickness unambiguously, this approach requires a priori knowledge of the refractive indices of both film and substrate [202]. Beyond transparent films, model-based CSI can be used to obtain a corrected surface topography for any combination of dissimilar materials with known visible-

spectrum refractive indices [202]. An alternative method for compensating for phase changes on reflection is presented in [222]. In this method, the variation of phase change with the spectral distribution of the light source is estimated through a first-order approximation and then compensated for the measurement errors by performing additional quasi-monochromatic PSI measurements.

The Michelson interference microscope objective has been the standard choice for low magnifications and large FOV, however, for magnifications below $2\times$ its increased physical size and weight due to its beam-splitting cube prism and off-axis reference path can be difficult to manage and limit its use on flexible platforms with turreted objectives [29]. An alternative wide-field interference objective design that is more compact than the Michelson assembly has been described in [142, 143, 223]. This recent design uses coaxial, partially transparent beam splitter and reference plates, as shown in Figure 3.9. A small tilt angle for both plates, from one to two degrees for the beam splitter and twice that amount for the reference, directs unwanted reflections away from the optical axis, where they are blocked by the aperture. The asymmetric design has little effect on imaging quality at NA values less than 0.1, therefore this approach is most convenient for large FOV applications, where the inherently compact design is preferable to an oversized Michelson objective [142].

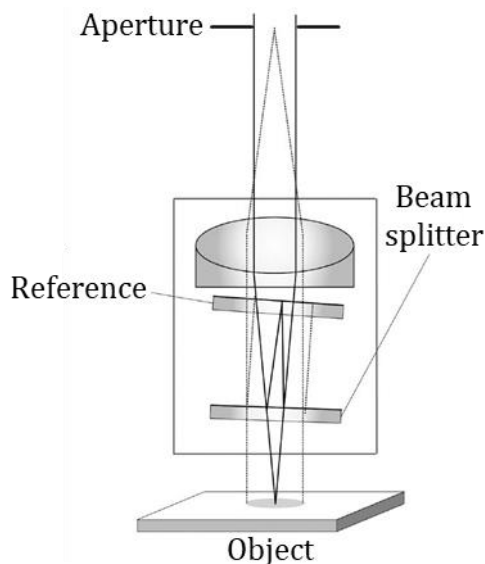


Figure 3.9 Wide-field interference microscope objective for areal surface topography measurement with coaxial, slightly tilted reference and beam splitter plates (adapted from [142]).

In conventional CSI, the spectral information that enables the measurement of surface heights is not used to derive the colour of the object surface, as the latter is generally not required for conventional surface metrology (e.g. the measurement of surface form and texture) [224]. Nonetheless, there are applications where the addition of colour information can be relevant. For example, topography and colour data can be combined to produce true colour images of the object surface, where the colour data can be used to identify material differences or defects such as blemishes that are otherwise unrevealed in a surface topography map. Blemishes and discolouration can be indicative of a variation in the manufacturing process or relate to wear or heating of a component, which may correlate to surface texture [29, 45, 224].

One way to add colour imaging capability to a CSI instrument is to replace the usual monochrome detector array by one equipped with a mosaic of colour filters [29]. However, the implementation of this approach affects the lateral sampling which, if not compensated for, can limit the effective lateral resolution [225]. An alternative to overcome the loss of lateral sampling is to use a multi-detector colour camera [225, 226]. A different approach that does not require replacing the conventional monochrome detector is to use a switchable light source (e.g. a multi-LED illuminator) to synthesise a variety of illumination spectra that enables colour imaging [224]. In this approach, a first data acquisition in conventional CSI mode captures the surface height data. A following data acquisition using a different illumination where red, green and blue colour channels are synthesised provides the colour data. Finally, the surface height data is combined with the multi-channel colour data to give true colour results with full lateral resolution [45, 224].

While LEDs and incandescent lamps are common examples of light sources used in CSI, it is possible to use femtosecond pulsed lasers [227]. The low temporal but high spatial coherence of femtosecond pulsed lasers enables a large FOV with high fringe visibility. Femtosecond lasers can be used for the measurement of step-like structures fabricated on microelectronic components [228] and for the measurement of rough silicon carbide (SiC) surfaces [229].

Methods based on instantaneous phase estimation have been developed to measure dynamic samples and reduce vibration sensitivity. These include the

spatial carrier fringe technique [230, 231] and the use of polarising elements to simultaneously generate and capture a series of phase-shifted interferograms in a single camera frame [232-235].

To increase measurement speed, Jeon et al. [236] recently proposed a CSI system that is not restricted by vertical scanning conditions such as a step size smaller than that determined by the Nyquist sampling limit and equidistant step. This system uses a polarised CMOS camera to apply the spatial phase shifting technique [232, 235].

Coupland and Lobera [187] proposed a method to potentially improve the capability of CSI to measure steep surfaces. In this approach, improved estimates of the surface illumination conditions were obtained by tilting the sample and subsequently using a finite element method to model surface scattering. Thomas et al. [237] recently presented a rigorous model of CSI based on a boundary elements method, where multiple scattering effects are considered.

4 Coherence scanning interferometry for metal additive manufacturing

The work presented in this chapter has been published in [75].

4.1 Introduction

As previously addressed in Section 2.1.1, AM techniques provide additional options to industry and significant advantages for specific applications, relative to conventional manufacturing processes. This is mostly because AM allows the creation of complex geometries and internal features that cannot be produced using subtractive methods due to their inherent tool path restrictions [2]. Other advantages include short product manufacturing cycles and economic low volume production. Standard high-performance engineering and biomedical materials, which include titanium and aluminium alloys, are suitable for AM production [38-40].

Among metal AM processes, PBF has been the process with the greatest economic impact and is the subject of extensive research [36]. PBF is a process in which thermal energy (typically a laser or electron beam) selectively fuses regions of a powder bed [34]. The two most common PBF processes are LPBF (also referred to as selective laser melting) and EBPBF (sometimes referred to as electron beam melting) [44]. The working principles of LPBF and EBPBF are described in Section 2.1.2. LPBF and EBPBF are the processes used to manufacture the metal AM samples used for this thesis.

A current limitation of these metal AM techniques is the poor quality of dimensional tolerance, surface texture, and surface integrity, compared with subtractively manufactured components [8, 38, 73], caused in part by the thermal distortions of a highly energetic process and in part by the irregularity of partially melted particles that adhere to the part surface [10, 40, 44]. PBF has proven to be a difficult process to control since the interactions between the energy beam and

the powder bed/molten pool are very complex [11], however, it has been observed that key process conditions may be identifiable from the specific surface features that these interactions produce [8-10, 48-58]. As such, there is a clear drive to achieve fast and reliable topographic measurement of metal AM surfaces. The caveat is that both LPBF and EBPBF surfaces present significant challenges for any measurement technique: high feature density, large spatial frequency bandwidth, high surface slopes, varying surface texture and reflectivity, frequent discontinuities, and re-entrant features. When used to measure metal AM surfaces, both contact and non-contact measurement methods require careful selection of measurement conditions to minimise a number of common error sources [8].

A number of technologies have recently gained traction as methods of areal topography measurement, most notably using optical techniques [25]. Metrology instruments based on optical imaging are significantly faster than stylus measurements that require mechanical raster scanning to cover a surface area, as previously discussed in Section 2.2.2. While other technologies exist, optical methods currently gaining industrial acceptance include CM [22, 23], CSI [18, 19] and FV [20, 21] (see Section 2.2.3). Height map data acquired using one of these systems can be used to generate areal surface texture parameters (e.g. S_a , S_q) [79, 105], that are considered to be a more complete description of surface structure than the analogous line profile parameters (e.g. R_a , R_q) [95, 108] (see Section 2.2.4).

CSI is a non-contact measurement method that uses a broadband light source and interference to measure surface topography and object geometry (see Section 3.2 for a detailed description of the working principles of CSI). CSI systems can measure smooth surfaces with sub-nanometre precision along the direction of surface height [29, 31]. Nevertheless, as a result of the limited NA of the imaging system, conventional CSI systems can be limited by reduced SNR when measuring high-slope angle surface features and by multiple reflective features common to rough textures [8], resulting in an inability to reliably determine surface heights. As discussed in Section 3.3, the need for high-slope measurement with a conventional CSI instrument often involves using a high magnification objective [174], not because of the need for magnification but because these objectives

usually have high NA. The highest NA objectives commercially available have maximum acceptance angles of approximately 45 deg. Reaching and even surpassing the NA limit requires a significant enhancement of the sensitivity of the instrument [29].

Recent innovations in CSI technology have increased the baseline sensitivity of a measurement (see Section 3.4 for a review on applications and technical advances). This improved sensitivity increases the capability of CSI instruments to measure surface features with high slopes or low reflectance [188], making CSI a potentially valuable tool for process development and quality control of metal AM parts. In 2010, a good practice guide for CSI measurement of rough surfaces was published [30], but the addition of new techniques further expands the range of measurement parameters beyond those outlined in this guide.

This chapter presents an empirical sensitivity analysis of a state-of-the-art CSI system for several metal AM samples made from different materials and possessing large variations in surface features and roughnesses. The goals of this study are to demonstrate the feasibility of using CSI for measuring metal AM surfaces and to evaluate the effectiveness of relevant and advanced CSI measurement functions and settings, such as spectral filtering of the broadband source, HDR lighting levels, oversampling, and robust topography reconstruction algorithms. The basic principles of these functions are described in Section 4.2. The details of the CSI system and the AM samples, as well as the methodology of the experimental design, are given in Section 4.3. The results are shown and discussed in Section 4.4. Finally, recommendations are provided for the optimisation of future measurements of metal AM surfaces using CSI. Recommendations for measurement optimisation balance three aspects: data coverage, measurement area, and measurement time. This study also presents insight into areas of interest for future rigorous examination, such as measurement noise and further development of guidelines for the measurement of metal AM surfaces.

4.2 Advanced functions in CSI

4.2.1 Topography reconstruction method

In CSI, surface topography is derived from the interference fringes that are observed as the objective is scanned in the direction of surface heights. The CSI signal for each pixel appears qualitatively as interference fringes modulated by a coherence envelope corresponding to the spectrally broadband, extended illumination. The position of the envelope function provides a first estimate of height and a determination of the integer fringe order, whereas the fringe phase information refines this estimate [30]. Various methods have been developed for reconstructing surface topography from fringes, such as coherence envelope detection [157], the FDA method [165] and the correlogram correlation method [214-216]. In practice, it is not always possible to perform the second step of evaluating fringe phase, resulting in a loss of precision as the price for greater tolerance of surface texture [31]. When measuring rough surfaces at scales less than the lateral optical resolution of the microscope objective, the phase of the fringe data may not correlate well with the surface profile and random phase jumps may be observed in the fringe data [30]. For this reason, the potential for additional precision in the axial direction provided by phase measurement may not be exploited in the measurement of rough surfaces. In this case, fringe analysis methods based on the coherence envelope, e.g. the centroid or peak position, may provide a similar accuracy and higher robustness.

4.2.2 Filtering of the source spectrum

Commonly, CSI instruments use a broadband source, e.g. a light-emitting diode, with a bandwidth of between 50 and 150 nm corresponding to a coherence length of approximately 3 μm , which is suitable for acquiring data from most surfaces. However, rough surfaces can make a CSI instrument prone to data dropout, as the signal strength declines if the roughness within the imaging area of a single pixel is larger than the coherence length [30, 144]. As the bandwidth of the source

spectrum is inversely proportional to the coherence length, by narrowing down the bandwidth, the lost data due to inadequate signal strength may be captured as the coherence length is increased. The bandwidth of the source spectrum can be adjusted either through the use of bandwidth narrowing filters, which can be introduced into the optical path, or by using multiple sources of different bandwidths [30]. However, reducing the bandwidth of the source spectrum will also broaden the coherence envelope, and, consequently, the measurement uncertainty will increase [30].

4.2.3 Oversampling

A conventional CSI measurement may lose data coverage for surface regions featuring high slopes and low reflectivity. The missing data may be detectable if the measurement is sufficiently sensitive. One technique for enhancing the sensitivity is sampling at smaller phase increments to increase the number of camera acquisitions over each interference fringe. This method is sometimes referred to as oversampling [29, 188]. Oversampling leads to a dynamic noise reduction. Increasing the oversampling factor, i.e. increasing the number of camera acquisitions over each fringe, can improve the SNR and has been recently included by some commercial CSI systems, aiming to extract very weak signals from challenging surfaces [29], such as those found in metal AM parts, which often feature a large roughness or steep slopes.

4.2.4 HDR lighting levels

When performing conventional CSI measurements, the intensity level of the light source is adjusted to avoid sensor saturation and hence is driven by the highest reflectance region on the investigated surface [30]. However, this strategy may have a negative impact over the measurement of regions with low reflectance features and/or high slopes, which already are prone to data dropout due to the low signal strength. When an HDR measurement is used, multiple exposures are collected in sequence, with either varying light intensity levels or exposure times,

and a composite image is formed from the image data with the highest SNR, commonly gauged by the contrast that each pixel has to its neighbours [188]. Therefore, the HDR function can be used to optimise the signal strength when measuring surfaces with a large variation in reflectance and/or slope, such that the number of missing data points may be reduced. Nevertheless, the total measurement time is increased by the number of lighting levels that have been used.

4.3 Method

4.3.1 Instrument

A ZYGO NewView™ 8300 CSI system [238] was used for this work. The instrument was located in a facility with a controlled temperature of (20 ± 1) °C, isolated from noise and dust. Four different objective lenses, with magnifications of 1.4× [142], 5.5×, 20×, and 50× were investigated and combined with 0.5× and 1× zoom lenses. The specifications of the objective lenses are shown in Table 4.1.

Table 4.1 Optical parameters for different objective lenses [239].

Magnification	1.4×	5.5×	20×	50×
NA	0.04	0.15	0.40	0.55
Optical resolution / μm	7.13	1.90	0.71	0.52
FOV (0.5× zoom) / (mm × mm)	12.09	3.02	0.84	0.34
FOV (1× zoom) / (mm × mm)	6.00	1.50	0.42	0.17

A lens with a lower magnification provides a larger FOV but a lower lateral resolution [122]. Usually a large FOV is desired when measuring AM parts because the surface areas are often large and rough, and form information can be obtained without using stitching of many single measurements. Consequently, the measurement takes less time if using a lens with a large FOV for the same surface since fewer individual measurements are required. A lens that offers a small FOV but a high NA may become very useful when high-resolution local details of the

surface topography are desired or when the surface contains a large number of high-slope areas.

In the NewView system, the source spectrum can be controlled by manually changing the filter in the instrument between a neutral density (attenuating) filter and a 40 nm bandpass filter. The number of camera acquisitions over each fringe can be controlled using the 'signal oversampling' function in the software, where an integer multiple of the unit camera acquisition number (here referred to as 'oversampling factor') can be selected. A higher SNR, as well as a longer measurement time, is expected and is proportional to the selected integer number. By enabling the HDR function, two or three different lighting levels may be used to optimise the measurement.

4.3.2 Samples

Ti-6Al-4V exhibits good strength-to-weight ratios, high resistance to fatigue and corrosion, and high-temperature performance, leading to many aerospace applications [47, 240]. Ti-6Al-4V is also biocompatible, making it an ideal candidate for biomedical applications [3]. Al-Si-10Mg also has good strength, corrosion resistance, low density, and high-thermal conductivity compared with other alloys and is often found in aerospace and automotive components, as well as in functional prototypes [241]. For these reasons, both materials were selected to build three customised artefacts to be used as samples for this study, from the LPBF and EBPBF metal AM processes described in Section 2.1.2.

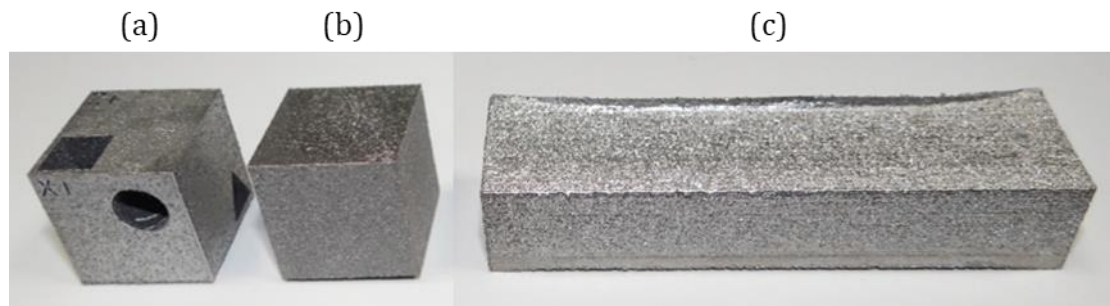


Figure 4.1 Pictures of the metal AM samples: (a) Al-Si-10Mg, (b) Ti-6Al-4V LPBF cubes, and (c) Ti-6Al-4V EBPBF rectangular prism.

The first and second artefacts consist of 20 mm Al-Si-10Mg and Ti-6Al-4V LPBF cubes, shown in Figure 4.1(a) and Figure 4.1(b), respectively. The third sample is a 20 mm × 15 mm × 75 mm Ti-6Al-4V EBPBF rectangular prism, shown in Figure 4.1(c).

4.3.3 Experimental design

The experimental work conducted through this study is designed to provide evidence as to whether CSI is suitable for measuring metal AM surfaces, to demonstrate the effects of implementing the selected advanced functions and settings of a modern CSI system for measuring metal AM surfaces, and to provide good practice guidelines for using CSI to measure metal AM surfaces.

Experiments were performed using metal AM samples with reasonably large variations in materials and surface topography features, and measurement parameters were chosen to reveal the most important and interesting aspects of the performance of a state-of-the-art CSI system. Further investigations could have been performed using additional samples and measurement parameters with diminishing returns, but the experiments were limited to minimise redundancy and to maintain concision. Experiments include (1) five common metal AM surfaces that cover a large range of surface roughness, slope distribution, and characteristic topography and (2) a series of measurements performed using a combination of four objective lenses and two optical zoom settings, two spectral filters, five oversampling settings, and two HDR lighting levels. For each surface, the optimised measurements are suggested in terms of data coverage, measurement area, and time.

Data coverage is used as a performance indicator that shows how many data points are accepted in a measurement. This indicator plays a key role both for the assessment of surface texture and for the characterisation of localised topographic features. In this investigation, data coverage is calculated as the ratio between the number of accepted data points and the number of total pixels in the camera (a 1024 × 1024 array). In general, the acceptance of a data point depends on the SNR. The latter can be evaluated for an individual pixel, for example, by calculating the ratio between the signal strength and the noise level. In this study,

missing data was not filled, just omitted. The fringe analysis method based on the coherence envelope (obtained using the FDA method) was used for this study because it is more robust when the SNR is low due to high roughness of the surface (as discussed in Section 4.2.1); thus, the data coverage can be optimised.

4.4 Results

4.4.1 Areal surface texture measurements

The surfaces were evaluated using the ISO 25178-2 areal surface texture parameters Sq and Sdq [79, 105]. As described in Section 2.2.4, the Sq parameter is a height parameter calculated from the RMS of the ordinate values within a defined area, while the Sdq parameter is a hybrid parameter calculated from the RMS of the surface gradient within a defined area. These parameters were selected to provide sufficient insight into the topography of the investigated surfaces, regarding not only height but also gradient.

Limited data coverage was found to bias the surface texture parameters, having a significant impact on Sdq , while Sq is less affected. This results from Sdq accounting for the slope information, which may be challenging to measure when in the presence of high-slope angle surface features that meet or surpass the NA limit of the imaging system of a CSI. Therefore, Sdq and Sq were calculated only from measurement results with a data coverage above 99%.

Table 4.2 Results of the areal surface texture parameters.

Surfaces	$Sq / \mu\text{m}$	Sdq
S1 LPBF Al-Si-10Mg cube, top surface	18 ± 1	0.6 ± 0.1
S2 LPBF Al-Si-10Mg cube, side surface	19 ± 1	0.9 ± 0.1
S3 LPBF Ti-6Al-4V cube, top surface	21 ± 2	1.1 ± 0.1
S4 EBPBF Ti-6Al-4V rectangular prism, top surface	33 ± 2	1.6 ± 0.2
S5 ^a LPBF Ti-6Al-4V cube, side surface	16 ± 2	10 ± 1

^aS-filter with a nesting index of $1 \mu\text{m}$ and an L-filter with a nesting index of $100 \mu\text{m}$.

The values of the parameters shown in Table 4.2 were taken using a 5.5× objective lens at a 1× zoom. An S-filter with a nesting index of 5 μm and an L-filter with a nesting index of 1000 μm were applied [106]. Filtering of the surface was performed to bandwidth match [98] data while removing only high-frequency noise and long-scale waviness/form, with the intention of maximising the examined measurement bandwidth. For AM surfaces, filtering may be driven by the need to characterise the surface functional performance, which requires knowledge about the scales of the topographic features that contribute to function, or to investigate signature features left by the manufacturing process, which requires knowledge about the expected sizes of the signature features of interest. It should be noted that filters do not produce a clear cut in wavelength removal but rather introduce an attenuation effect that alters several spatial wavelengths close to the cut-off by differing amounts [13].

Given the complexity of the metal AM surfaces used in this study, the variations of the texture parameters across the surface were considered by measuring ten different areas across the investigated surface and then calculating the standard deviations of Sq and Sdq . The standard deviations are listed in Table 4.2. The measured topographies of the corresponding sample surfaces are shown in Figure 4.2, where the topography of S1 obtained by the 1.4× objective lens is also included to show the advantage of wide-field topography measurement (see Figure 4.2(a)).

Absolute accuracies of the surface topography measurements are complex to evaluate [77, 114, 242], as previously discussed in Section 2.2.6. Evaluations of measurement noise (which is surface-tilt dependent [172]) and surface topography repeatability for very rough and irregular surfaces are also complex, and relevant information is rare in the literature. It is well known that CSI can measure smooth, flat surfaces with sub-nanometre measurement noise [31]. However, in the preliminary results it was found that the measurement noise for the investigated metal AM surfaces was considerably higher (up to a sub-micrometre level). Measurement noise values were determined from the difference of two repeated measurements, in accordance with ISO/DIS 25178 part 700. Using the 5.5× objective lens at a 1× zoom and the instrument's default measurement settings, the measurement noise value for S1 was 0.04 μm, for S2

was $0.06 \mu\text{m}$, for S3 was $0.21 \mu\text{m}$ and for S4 was $0.38 \mu\text{m}$ (S5 was not considered for the evaluation of measurement noise due to poor data coverage). This finding prompted further research on the evaluation and reduction of measurement noise for a wide range of applications, which is presented in Chapter 6.

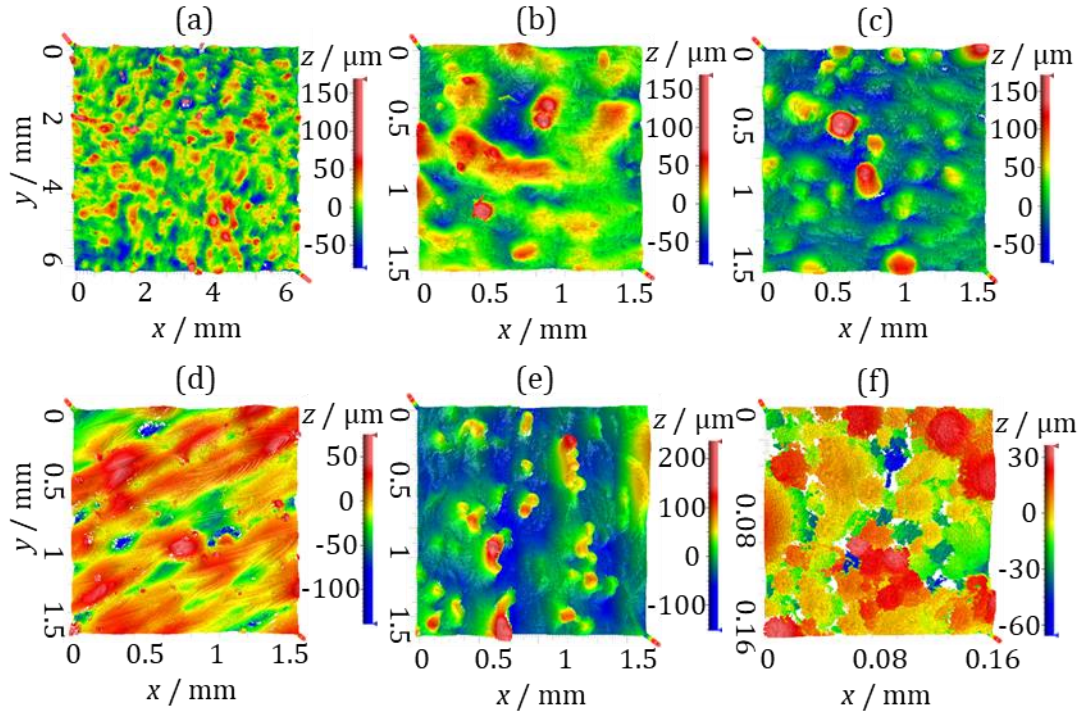


Figure 4.2 CSI measurements of metal AM surfaces: (a–b) LPBF Al-Si-10Mg cube top surfaces, (c) LPBF Al-Si-10Mg cube side surface, (d) LPBF Ti-6Al-4V cube top surface, (e) EBPF Ti-6Al-4V rectangular prism top surface, and (f) LPBF Ti-6Al-4V cube side surface. The $1.4\times$ objective lens ($1\times$ zoom) was used for (a), the $5.5\times$ objective lens ($1\times$ zoom) was used for (b–e), and the $50\times$ objective lens ($1\times$ zoom) was used for (f).

4.4.2 Effects of measurement functions and settings on data coverage

4.4.2.1 Effects of spectral filtering

The surfaces S1 to S4 were measured using the $5.5\times$ objective lens ($1\times$ zoom) and different source spectrum filters. The filters used for this study are neutral density filters that provide bandwidths of ~ 100 and 40 nm , respectively. The data coverage of each dataset is plotted against the corresponding Sq and Sdq parameters in Figure 4.3. The result shows that the data coverage values inversely

correlate with these surface parameters, i.e. data coverage decreases when surfaces are rougher.

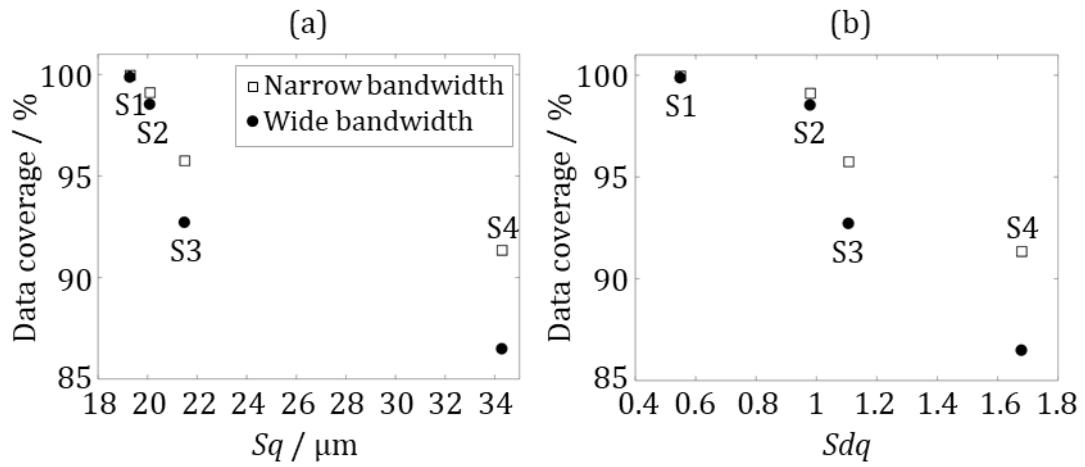


Figure 4.3 Effects of spectral filtering on data coverage. The data coverage is plotted against (a) Sq and (b) Sdq . The $5.5\times$ objective lens ($1\times$ zoom) was used.

In addition, it is observed that data coverage is improved using the source spectrum with a relatively narrow bandwidth, and the degree of improvement correlates with the roughness and slope parameters, i.e. the improvement is more pronounced for a surface with large Sq and Sdq values. The result agrees with the theory discussed in Section 4.2.2.

4.4.2.2 Effects of oversampling

Increasing the oversampling factor improves the SNR and has been shown to be useful in expanding data coverage as the latter is directly related to the SNR of each data point (see Section 4.3.3 for a description of data coverage). As shown in Figure 4.4, this effect is more evident for surfaces with larger values of Sq and Sdq . Nevertheless, using a substantial oversampling factor will increase the total measurement time by the same factor.

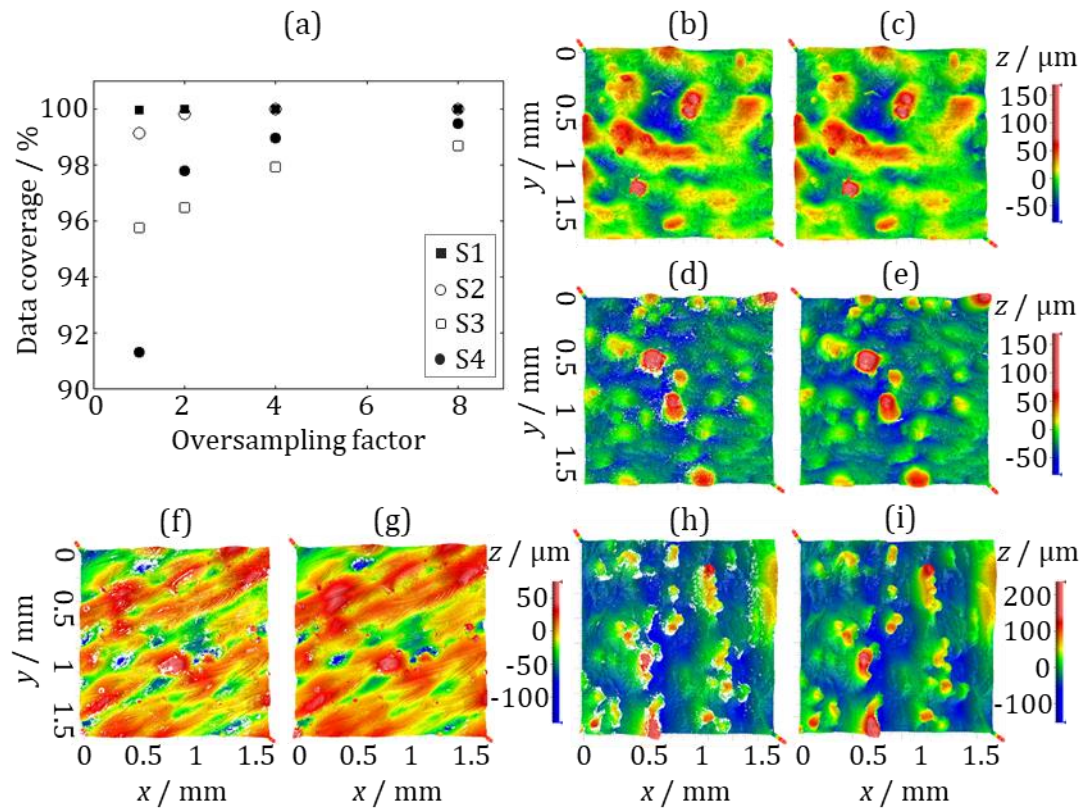


Figure 4.4 Effects of oversampling on data coverage. (a) Data coverage plotted against oversampling factor where the factor number equal to one means oversampling is not used; (b), (d), (f) and (h) measured topography maps of S1, S2, S3 and S4 without using oversampling, respectively; (c), (e), (g) and (i) measured topography maps of S1, S2, S3 and S4 using 8 \times oversampling, respectively. The 5.5 \times objective lens (1 \times zoom) and the 40 nm bandwidth spectrum were used.

For rougher surfaces, such as the EBPBF Ti-6Al-4V rectangular prism top surface (S4), significant improvements were achieved, as shown in Figure 4.4(i). Regions presenting steep slopes, peaks, and pits that previously caused the instrument to gather scarce data were almost fully covered using 8 \times oversampling.

The LPBF Ti-6Al-4V cube side surface (S5) features multilevel hills and dales, presumably formed by loose powder and poorly melted particles during the manufacturing process, creating a significant measurement challenge. Despite these complex topographic features, reasonably good measurements (in terms of data coverage) can be achieved using objective lenses with higher NA in addition to the oversampling function (see Figure 4.5).

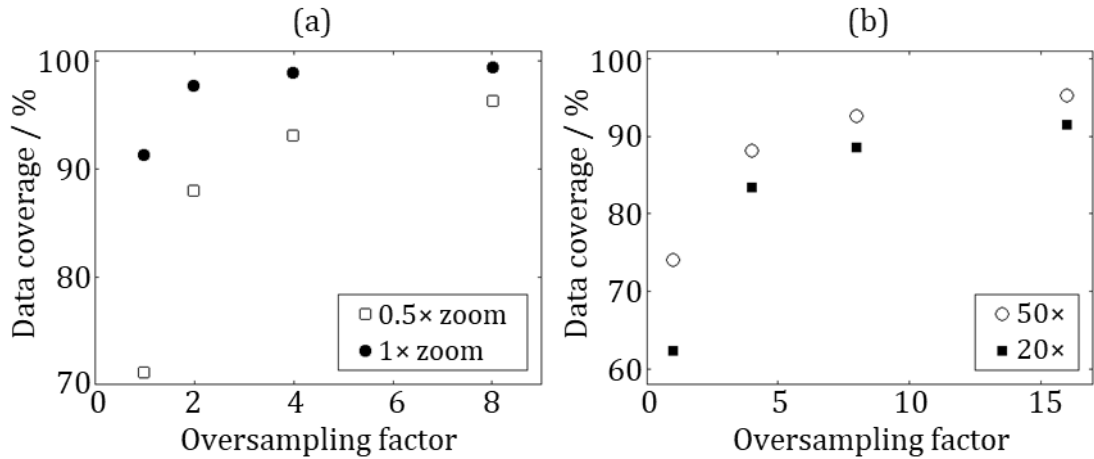


Figure 4.5 Effects of oversampling on data coverage for (a) EBPBF Ti-6Al-4V rectangular prism top surface (S4) using the 5.5 \times objective lens (0.5 and 1 \times zoom) and (b) LPBF Ti-6Al-4V cube side surface (S5) using the 20 \times and 50 \times objective lenses (1 \times zoom). The 40 nm bandwidth spectrum was used.

4.4.2.3 Effects of HDR of lighting levels

Enabling the HDR function for lighting levels can enhance data coverage, as shown in Figure 4.6. Measurement time will be doubled if two lighting levels are used; thereby, it makes sense to compare the results with those obtained using 2 \times oversampling. For rough surfaces featuring a large number of high slopes and relatively dark regions, HDR generated better results than those obtained using oversampling, given that the total measurement time is equal (twice the time of a single scan). In the case of smoother surfaces, using 2 \times oversampling provided similar or slightly better data coverage compared with HDR. It is clearly shown that both of these advanced functions provide improved measurements, particularly in the case of very rough surfaces.

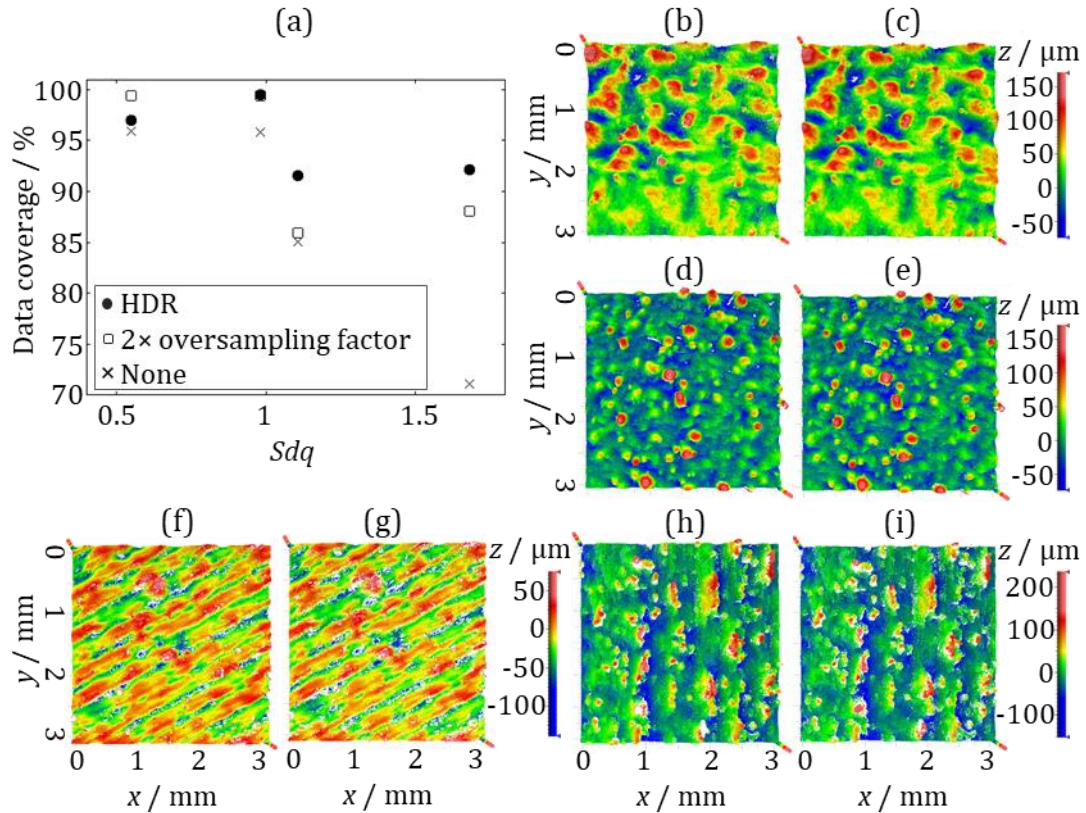


Figure 4.6 Comparison of performance between HDR (two lighting levels) and oversampling (2 \times). (a) The data coverage is plotted against Sdq . The result of the original measurement without using any of the advanced functions is shown as the crosses; (b), (d), (f) and (h) measured topography maps of S1, S2, S3 and S4 using HDR, respectively; (c), (e), (g) and (i) measured topography maps of S1, S2, S3 and S4 using 2 \times oversampling, respectively. The 5.5 \times objective lens (0.5 \times zoom) and the 40 nm bandwidth spectrum were used.

4.4.3 Recommendations for the optimisation of the measurement

Results presented in Section 4.4.2 show that progressively increasing the oversampling factor, using HDR of lighting and a narrow bandwidth source spectrum (after properly adjusting the most basic settings of a CSI instrument, e.g. tilt and scan length), will improve the SNR and, therefore, increase data coverage without sacrificing measurement area due to the usage of a high NA lens; however, the measurement time may be compromised. In this section, recommendations are provided for optimising the CSI measurements for metal AM surfaces, in terms of measurement time and area within acceptable levels of data coverage. Recommendations are given in Table 4.3 by considering a data coverage level of

at least 95%. Higher data coverage, above 99%, (marked with superscript ‘b’ in Table 4.3) may be achieved for some measurements at the cost of increased measurement time. Some examples of the optimised measurements are shown in Figure 4.2.

Table 4.3 Measurement optimisations for metal AM surfaces in terms of measurement time and FOV (95% minimum data coverage by default).

	S1/S2	S3	S4	S5
Sample surfaces	LPBF Al-Si-10Mg top/side	LPBF Ti-6Al-4V top	EBPBF Ti-6Al-4V top	LPBF Ti-6Al-4V side
Spectral filtering	Narrow (40 nm bandpass filter)			
Fringe analysis	Coherence envelope method			
Objective lens ^a	1.4× ^b	5.5×	5.5×	50×
Oversampling factor	—	— or 4 ^b	2 or 8 ^b	16

^a1× zoom lens.

^bFor data coverage > 99 %.

Relatively smooth metal AM surfaces, e.g. LPBF Al-Si-10Mg (S1 and S2), can be easily measured using low magnification objectives, e.g. the 1.4× wide-field lens, without the need of additional advanced functions. Rougher metal AM surfaces, e.g. LPBF and EBPBF Ti-6Al-4V top surfaces (S3 and S4), can still be measured with 95% data coverage using low-magnification objectives, without significantly increasing the measurement time. For even more challenging metal AM surfaces, a high NA objective lens should be used to measure high slopes, and a much larger oversampling factor is needed. Consequently, the measurement area will be reduced and the measurement time will be increased significantly. However, with a few stitched fields of view it is possible to get a big enough measurement area to assess appropriately.

4.5 Conclusion

Metal AM surfaces have high roughness and contain a large number of high slopes and loose particles. Thus, it is very difficult to accurately measure surface

topography at a high resolution. The CSI technique was originally designed to measure relatively smooth surfaces (e.g. optics and semiconductor applications). This technique has previously not been considered feasible for measuring AM surfaces. However, recent progress in the development of the CSI technique allows a significantly enhanced detection sensitivity through the use of advanced measurement functions, such as filtering of the source spectrum, HDR lighting levels, adjustable number of camera acquisitions over each interference fringe (i.e. oversampling), and robust topography reconstruction algorithms.

In this chapter, the effects of advanced CSI measurement functions on the measurements of several typical metal AM surfaces have been demonstrated and analysed systematically. Recommendations are provided for optimisation of measurement for metal AM surfaces in terms of time, measurement area, and data coverage. Results show that the CSI technique can provide adequate surface topography measurements for metal AM surfaces with various roughness levels and slope distributions.

In a similar way to the work presented here, a study regarding the development of guidelines for the optimal measurement of metal AM surfaces was carried out for the case of using the FV technique [76]. This study investigated the effects of various measurement parameters, such as vertical resolution, lateral resolution and illumination. The experimental campaign was created through full factorial design of experiments, and regression models were used to link the selected measurement parameters to the measured quality indicators. The results of this work indicate that while measurement settings have little influence on surface texture parameters such as S_a , other measurement quality indicators such as local repeatability error and the percentage of non-measured points are significantly affected.

In a later investigation carried out by colleagues from the Manufacturing Metrology Team, a region of interest on a metal AM surface was inspected using different optical topography measurement technologies, including CSI and FV [74]. Several smaller regions were extracted from the original topography maps to isolate relevant metal AM surface features, such as weld ripples, particles, recesses and weld tracks. The results of this study showed that CSI reconstructions returned a high number of clearly discernible weld ripples,

whereas the presence of ripples was reported in the FV topography maps to a lesser extent, as most of the small-scale detail was lost. It was also observed that CSI better captured the sphere-like nature of particles. Given that FV operates by finding the maximum contrast within a region of observed image pixels, it can experience difficulties when a surface is locally very bright or otherwise uniform because of its smoothness, as is the case with the sphere-like particles. However, it must be noted that results are highly dependent on instrument make and model, measurement settings, and specific conditions related to the measured sample.

5 Process-surface analysis in polymer additive manufacturing

The work presented in this chapter has been published in [201].

5.1 Introduction

AM technologies are currently able to fabricate parts made of metals, ceramics and polymers, the latter being the most widely used material class in AM [36] (an overview of AM technologies is presented in Section 2.1.1). Due to its low cost and flexibility, ink-jet printing is considered to be one of the key technologies in the field of controlled micro- and nanoscale deposition of polymers [63, 64]. In ink-jet printing, a print head ejects droplets of liquid phase material (e.g. a polymer ink) at precise coordinates onto the substrate; the deposited ink droplets dry to form a film and, by printing sequential layers, three-dimensional parts can be formed [2, 60-62] (as previously described in Section 2.1.3). Applications of ink-jet printing include the fabrication of polymer transistor circuits [65], light-emitting polymer displays [66-68], polymer solar cells [69], as well as polymer sensors and actuators [70, 71].

AM parts in general, have suffered until recently from a lack of understanding of the mechanisms of the underlying processes [9]. As discussed in Section 2.1.4, the measurement and characterisation of surface topography can allow a manufacturer to better understand how the features of a given topography were formed, and ultimately how these features relate to the manufacturing process that created that surface [17, 48]. There is scarce knowledge regarding how some fluoropolymers, in this case THV, can be ink-jet printed. A quantitative analysis of the micro-scale areal surface topography can provide a better understanding of the characteristic textures that result from the ink-jet printing process of this polymer. Most THV applications include multilayer parts, where a thin layer can be used as a protective coating, or to provide enhanced barrier properties to other

layers [72, 243, 244]. The demand for nanometre-thick films is constantly increasing and ink-jet printing can address this level of miniaturisation due to its high resolution and precision [36].

This chapter presents an investigation into the characteristics of the topography of ink-jet printed THV surfaces. Several THV samples were ink-jet printed, covering a variety of structures with basic geometric shapes, such as dots and films. The sizes of the polymer structures ranged from a few nanometres to tens of micrometres in thickness (i.e. height), and from tens of micrometres to a few millimetres in spatial wavelength (i.e. lateral width). To produce the polymer structures, relevant printing parameters were selected and varied, which included polymer concentration, drop spacing and number of layers. The goal of this study is to assess the feasibility of ink-jet printing THV and to provide a better understanding of the features and characteristic textures that result from the ink-jet printing process. This investigation also provides an insight into how to control and optimise the quality of THV ink-jet printed parts.

5.2 Materials and methods

5.2.1 THV 221

THV 221 is a transparent fluoroplastic comprised of 51.4% tetrafluoroethylene (TFE), 10.4% hexafluoropropylene (HFP) and 38.2% vinylidene fluoride (VDF) [245]. Fluoroplastics are polymers with multiple carbon-fluorine bonds [246]. This family of polymers have been widely used in the automotive, electrical and chemical industries, as well as in medical devices and aircrafts [244, 247], since their properties allow wide service temperatures and high resistance to chemicals, sunlight, flames and weathering. Fluoroplastics are probably most recognised for their use as a coating for non-stick cookware, i.e. polytetrafluoroethylene (PTFE), or for insulating wire and cable [244].

Despite the relatively low melting temperature of 115 °C, the decomposition temperature of THV 221 is around 410 °C [245]. The properties of THV include high transparency, bondability to itself and other substrates, high flexibility, low

flammability, high chemical and permeation resistance, low refractive index as well as efficient electron beam cross-linking [243, 247].

Most THV applications include multilayer parts, where a thin layer is used as a protective coating or to provide enhanced barrier properties to other layers [72]. The THV film formation processes, such as drop casting and electrospinning, are described elsewhere [245, 248]. THV has been used in medical applications, such as for coronary stents [249], due to its high biocompatibility and low drug permeability. THV can also be used in microfluidic devices due to its transparency, thermal resistance and chemical resistance [250, 251].

Ink-jet printing can benefit existing and potential applications that require miniaturisation due to its high resolution and precision (the smallest achievable resolution depends on the drop size, which is normally around 50 μm [252]). The literature about the ink-jetting of fluoropolymers is relatively limited and mainly focused on polyvinylidene fluoride (PVDF) [70, 71]. With the exception of PTFE and polyvinyl fluoride (PVF), all fluoropolymers are melt processable [247] but only a few are soluble in common solvents at room temperature, such as PVDF and THV 221 (THV is available in several grades but only THV 221 is soluble in conventional solvents [245]).

5.2.2 Ink-jet printing of THV 221

Fujifilm Dimatix™ DMP-2850 [253] and Nordson EFD PICO Pulse® [254](23) ink-jet deposition systems were used to print the THV 221 inks on glass substrates. The printers were located in a laboratory with a controlled temperature of (21.0 \pm 1.0) °C. Printer settings such as waveform, frequency and jetting voltage were adjusted following the manufacturer's guidelines.

As ink-jet printing requires relatively low viscosities, polymers can only be deposited from dilute solution [63]. Common solvents used to dissolve THV are acetone, ethyl acetate, methyl isobutyl ketone (MIBK) and dimethyl acetamide (DMAc) [249] (see Table 5.1). MIBK was selected as the main solvent because of its vapour pressure, which would allow a fast evaporation of the THV 221 inks, but not so fast that it could lead to blockages in the nozzles of the printers.

Table 5.1 Vapour pressure and viscosity at 20 °C for the solvents used to dissolve THV [255].

Solvent	Vapour pressure / mmHg	Viscosity / (mPa·s)	Boiling temperature / °C
Acetone	184.5	0.4	56.3
Ethyl acetate	73.0	0.5	77.1
MIBK	16.0	0.6	117.4
DMAc	1.3	2.1	166.1

The shear viscosity of the formulated THV 221 inks was measured using a rheometer at a shear rate of 100 s⁻¹ (see Table 5.2). The shear viscosity for inkjet applications is usually measured at a shear rate of 100 s⁻¹, as standard rheometers cannot reach the actual shear rates of jetting [62, 252]. In this thesis, the polymer concentration of the inks is expressed in weight percent (wt. %) and the solvent ratio is expressed in volume percent (vol. %).

Table 5.2 Viscosity of THV 221 inks (mean of three measurements) at different temperatures.

THV 221 ink formulation	Viscosity / mPa·s		
	22 °C	35 °C	45 °C
1 wt. % in MIBK	0.9	0.8	--
10 wt. % in MIBK	73.3	44.7	36.1
20 wt. % in 50–50 vol. % in MIBK–acetone	1088.0	848.8	680.1

Due to the relatively high polymer concentration of the THV 221 20 wt. % ink, acetone was added to MIBK at a 1:1 ratio by volume (i.e. 50–50 vol. % MIBK–acetone) to enhance dissolution. The THV 221 1 wt. % in MIBK ink was printed using the Dimatix system with a nominal nozzle diameter of 21 µm and a nozzle temperature of 28 °C, which corresponds to the minimum adjustable nozzle temperature of the printer. The THV 221 10 wt. % in MIBK and the THV 221 20 wt. % in 50–50 vol. % MIBK–acetone inks were printed using the PICO Pulse system with a nominal nozzle diameter of 150 µm and a nozzle temperature of 30 °C and 50 °C, respectively. The PICO printer allows the jetting of inks with higher

viscosities. Single and multiple layers of dots and films were ink-jet printed. The thickness of the printed parts ranged from a few nanometres to tens of micrometres.

5.2.3 Surface-measuring coherence scanning interferometry

CSI is a non-contact optical technique for measuring areal surface topography [19]. The detailed working principle of CSI is presented in Section 3.2. CSI can measure a variety of surface types, including applications that incorporate the measurement of metal AM parts (see Chapter 4), as well as transparent film structures and dissimilar materials [202, 203]. CSI has been used for the quality assurance of ink-jet printed polymer layers of drug-delivery systems [196] and for the characterisation of polymer coatings in silicon micro-electromechanical systems [256].

CSI has the advantage of being faster than contact methods and it is well suited for this application since it can measure transparent materials with high precision and without any potential damage to the investigated surfaces [29]. It has been identified elsewhere that contact stylus measurements are liable to damage polymer AM surfaces [15]. Another optical technique that has recently been used for the measurement of AM parts is FV, however, since this technique relies on analysing the variation of contrast, it is only applicable to surfaces where the contrast varies sufficiently during the vertical scanning process.

A Zygo NewView™ 8300 CSI system was used in this study. The instrument was located in a metrology laboratory with a controlled temperature of $(20.0 \pm 0.5) ^\circ\text{C}$. The specifications of the employed objective lenses are shown in Table 5.3. An objective lens with a lower magnification and zoom provides a larger FOV but a lower lateral resolution, as previously discussed in Section 3.3. However, a larger FOV is convenient when measuring the ink-jet printed surfaces because form information can be obtained without using stitching of many single measurements. A lens with a high NA is useful when the surface contains steep slopes that can cause a reduction of the intensity of the interferometric signal and consequently result in lost data points, or when high-resolution local details of the surface topography are desired [29]. Oversampling was enabled to enhance the

SNR [188], as the material is transparent. By using oversampling, the number of valid topography data points can be significantly increased, as shown in Chapter 4.

Table 5.3 CSI instrument specification.

Objective lens magnification	5.5×	20×
NA	0.15	0.40
0.5× zoom lateral sampling distance / μm	2.95	0.82
1× zoom lateral sampling distance / μm	1.47	0.41
0.5× FOV / mm	3.02×3.02	0.84×0.84
1× FOV / mm	1.50×1.50	0.42×0.42

5.2.4 Surface topography analysis

The thickness calculation was performed in a commercial surface analysis software [257], in a similar way to the calculation of a step height, using the following method. The central thickness T_c for each investigated ink-jet printed THV sample was determined as the height difference between the mean height values of the top surface \bar{h}_{top} (central region) and the glass substrate surface \bar{h}_{glass} . The topography data was levelled by subtracting the mean least-squares plane corresponding to the glass substrate surface. In a following step, an area of $(100 \times 100) \mu\text{m}$ around the centre of the top surface of the sample was selected and then a horizontal plane was obtained by averaging the height values located within the selected area. Similarly, a second horizontal plane was defined by the mean surface height value corresponding to the glass substrate. T_c was then calculated as the axial distance between these two parallel planes:

$$T_c = \bar{h}_{top} - \bar{h}_{glass}. \quad (5.1)$$

The edge thickness T_e of the printed drops was estimated as the height difference between the mean height value of the peaks localised at the edge of the drops \bar{h}_p (this feature will be described in Section 5.3.1) and the glass substrate:

$$T_e = \bar{h}_p - \bar{h}_{glass}. \quad (5.2)$$

In this study, the film measurement method described in [202, 203] to calculate thickness was not used, instead, thickness was measured like a step height (see Figure 5.1). In the film measurement method, a library of model signals is generated over a range of known film parameters, which then are compared to the experimental signal to find the best match. The step height approach was taken because the film measurement method requires accurate information of the refractive index of the films; otherwise, measurement uncertainty could be increased. Furthermore, the measurement of edge thickness (T_e) may not be possible using the film measurement method as the edges are essentially thin walls.

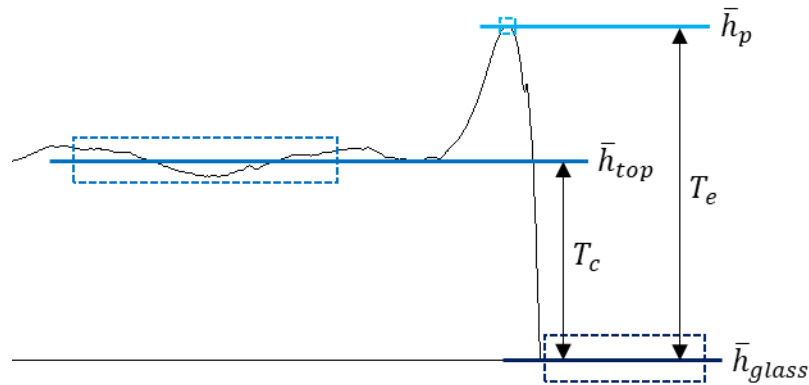


Figure 5.1 Diagram of thickness calculation.

For the printed drops, the variation of T_c and T_e was considered by measuring ten samples and then calculating the standard deviation, respectively. For the printed films, the variation of T_c was estimated as the standard deviation of five results (where each result corresponds to a different measured sample).

The surface texture of the ink-jet printed THV films was evaluated using the areal surface texture parameter Sq [105] – the RMS surface height deviation within a defined area. Levelling was applied using least-squares mean plane subtraction. An S-filter with a nesting index of $2.5 \mu\text{m}$ and an L-filter with a nesting index of $250 \mu\text{m}$ were applied to remove high-spatial frequency noise and long-scale waviness/form [107] (see Section 2.2.4 for a review on areal surface texture characterisation).

5.3 Results

5.3.1 THV 1 wt. % in MIBK

Single-layer drops of THV 1 wt. % in MIBK formed nanometre thickness films that showed polymer accumulation at the edges (see Figure 5.2(a)), having $T_c = 2$ nm and $T_e = (8 \pm 2)$ nm (T_c is the central thickness and T_e is the edge thickness, estimated using Equations (5.1) and (5.2), respectively).

The observed polymer accumulation at the edges of the drops is the result of a phenomenon known as the ‘coffee ring effect’ [258, 259], and refers to the solutes or dispersed particles in a solution that accumulate at the perimeter of an evaporating drop (or film), caused by outward capillary flows due to uneven solvent evaporation rates. The higher amount of solute at the edge or perimeter causes the formation of a ring that can be significantly thicker than the centre of the evaporated drop [259]. In the absence of the coffee ring effect, the solutes of an evaporating drop are evenly distributed, resulting in a uniform thickness.

Two-layer drops of THV 1 wt. % in MIBK (see Figure 5.2(b)) showed $T_c = (8 \pm 1)$ nm and $T_e = (50 \pm 9)$ nm. In this case, two edges were present, where the higher edge corresponded to the double-layer drop, which had a smaller width than the single-layer drop.

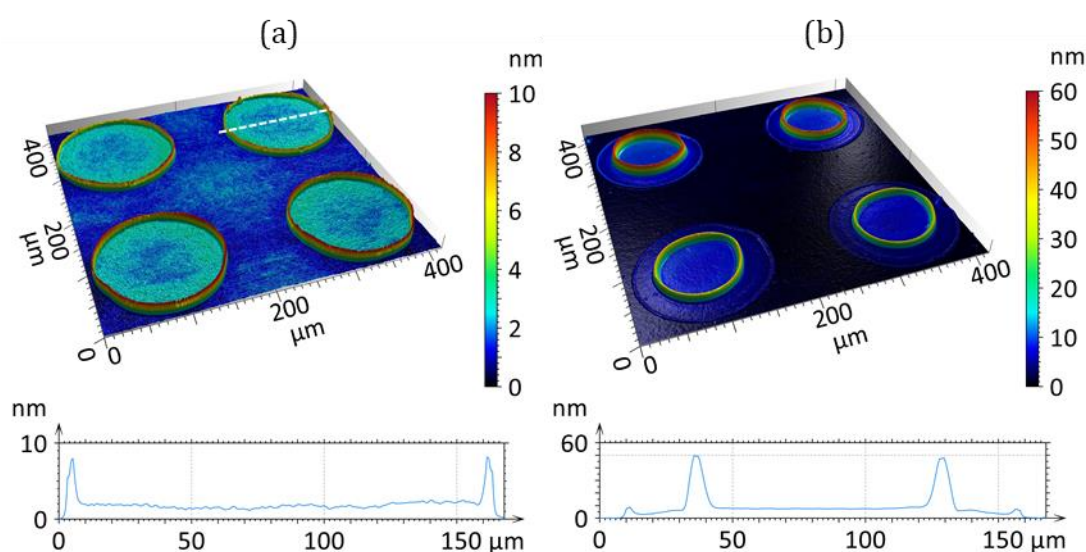


Figure 5.2 Surface topography and profiles corresponding to (a) one and (b) two-layer ink-jet printed drops of THV 1 wt. % in MIBK.

The observed decrease in drop width while printing on a previous layer is caused by a higher contact angle of the THV 1 wt. % in MIBK ink when it is deposited on a THV coated glass substrate, which was $(60 \pm 0.5)^\circ$, relative to when the ink is deposited on an uncoated glass substrate, which was $(18 \pm 1.4)^\circ$. The contact angle was determined by pendant and sessile drop analysis at a room temperature of 22 °C, considering the mean value and standard deviation of five repeated measurements. The contact angle is defined as the angle between the substrate surface and the tangent at the edge of the droplet's ovate shape, and it provides a measure of the ability of the ink to wet the surface of a substrate [260].

The thickness evolution with increased number of layers of the ink-jet printed drops of THV 1 wt. % in MIBK is shown in Figure 5.3. The thickness at the edges of the drops (T_e) increased at a ratio that was approximately ten times greater than the increase ratio at the centre (T_c).

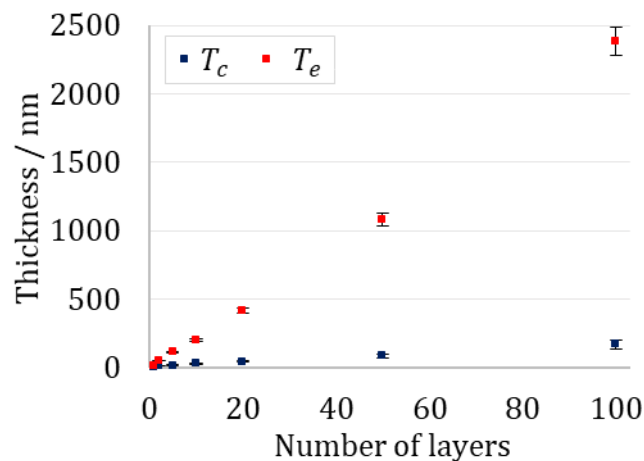


Figure 5.3 Thickness for the centre (T_c) and edge (T_e) of ink-jet printed drops of THV 1 wt. % in MIBK with increased number of layers.

Single-layer films were printed at drop spacings of 60 μm , 80 μm , 100 μm and 120 μm . The highest-quality results were obtained with a drop spacing of 80 μm , which generated smooth and uniform films, as shown in Figure 5.4. The films had $T_c = (8 \pm 1)$ nm, with $Sq < 1$ nm calculated over an area of (300×300) μm at the centre of the film.

Multiple layers were printed with a drop spacing of 80 μm , however, unexpected topography patterns started to appear. To further investigate the cause of the

observed topography patterns, drop spacings of 100 μm and then 120 μm were used to print 2, 5, 10, 20 and 50 layers.

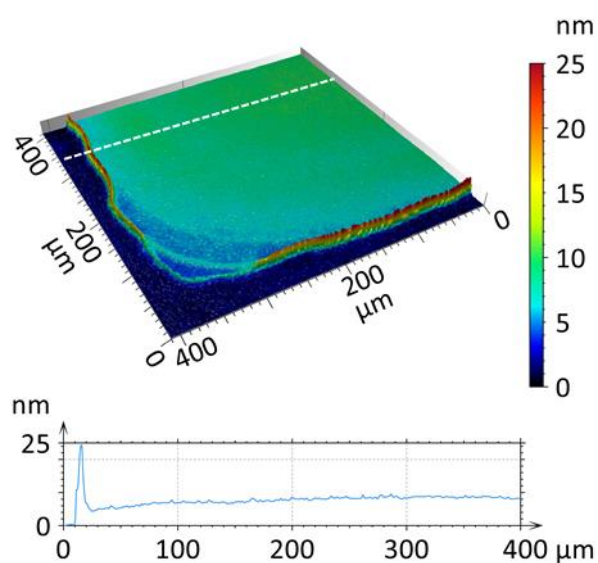


Figure 5.4 Surface topography and profile of a one-layer ink-jet printed film of THV 1 wt. % in MIBK.

With a drop spacing of 100 μm , bump-like features appeared between the positions of the jetted drops after the second layer. The formation of the bumps was counterintuitive, as they did not form in the centre of the printed drops; instead, they formed in between the drops. This effect was likely caused by the coffee ring effect. After 5 layers, the bumps increased in size, as shown in Figure 5.5(a), and after 10 layers, the bumps became smoother and partially joined together with the neighbouring bumps, forming craters with the shape of the drops (see Figure 5.5(b)). After 20 layers, the bumps fully joined together, and the craters became well defined (Figure 5.5(c)). After 50 layers, the craters were higher than the regions between the jetted drops (Figure 5.5(d)).

When a drop spacing of 120 μm was used, a similar trend was observed, but in this case, the drops did not touch as much as in the previous case. Peaks were formed by the overlapping regions of the contours of neighbouring drops likely caused by the coffee ring effect. With a smaller drop spacing the peaks would join in the centre between neighbouring drops, explaining the formation of bumps observed with a drop spacing of 100 μm .

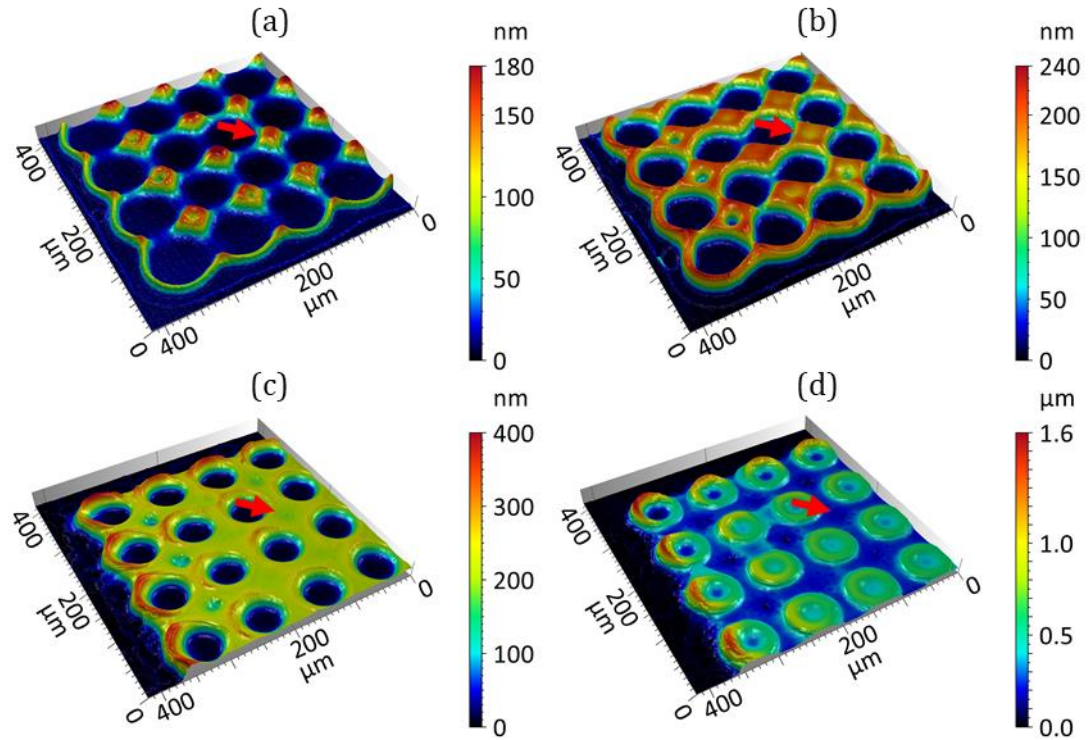


Figure 5.5 Surface topography corresponding to (a) five-layer, (b) ten-layer, (c) twenty-layer and (d) fifty-layer ink-jet printed films of THV 1 wt. % in MIBK.

5.3.2 THV 10 wt. % in MIBK

The optimal nozzle temperature for ink-jet printing THV 10 wt. % in MIBK was 30 °C, as splashing was observed with higher nozzle temperatures. The coffee ring effect was present when drops were printed, as can be observed in Figure 5.6(a–b), nevertheless, the effect was not as strong as in the case of THV 1 wt. % in MIBK. Single-layer drops of THV 10 wt. % in MIBK had $T_c = (1.52 \pm 0.11) \mu\text{m}$ and $T_e = (2.40 \pm 0.20) \mu\text{m}$. Double-layer drops gave $T_c = (2.29 \pm 0.21) \mu\text{m}$ and $T_e = (5.61 \pm 0.31) \mu\text{m}$. The decrease in drop width on the second layer was consistent with the observed results for the THV 1 wt. % in MIBK ink, which is explained by the difference in the contact angle with different substrate surfaces, i.e. uncoated glass or THV coated glass.

Films of THV 10 wt. % in MIBK were ink-jet printed using a drop spacing of 500 μm (approximately 20% of overlapping). The printed films did not show the coffee ring effect, as can be observed in Figure 5.6(c–d). The measured surface

topographies of the films exposed the presence of a slipping pattern towards the edges, likely caused by the non-pinning of the film edge on the substrate.

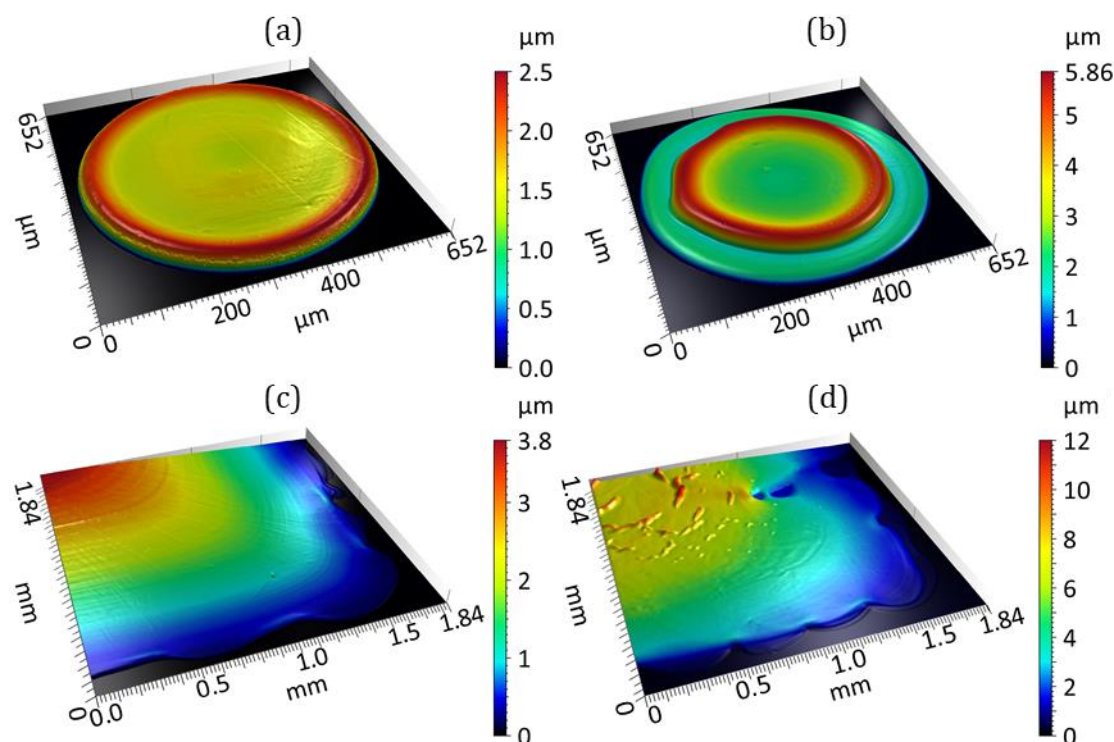


Figure 5.6 Surface topography corresponding to (a) a one-layer drop, (b) a two-layer drop, (c) a one-layer film and (d) a two-layer film of ink-jet printed THV 10 wt. % in MIBK.

Single-layer films had $T_c = (3.53 \pm 0.29) \mu\text{m}$, showing a texture of $Sq = (40 \pm 5) \text{nm}$. Double-layer films had $T_c = (7.21 \pm 0.60) \mu\text{m}$ and $Sq = (727 \pm 186) \text{nm}$, and showed the presence of wrinkle-like features on the surface (see Figure 5.6(d)). Sq was calculated over an area of $(1 \times 1) \text{mm}$ at the centre of the films. The wrinkle-like features were likely formed by the swelling of regions of the underlying THV film during the drying process, followed by a sudden and violent expansion of poorly dissolved regions [261, 262].

5.3.3 THV 20 wt. % in 50-50 vol. % MIBK-acetone

The optimal nozzle temperature for ink-jet printing THV 20 wt. % in 50-50 vol. % MIBK-acetone was found to be $50 \text{ }^\circ\text{C}$, as higher temperatures caused splashing,

while lower temperatures decreased splashing but made the ink-jetting process less reliable (e.g. faulty drop ejection).

The coffee ring effect was almost absent for the case of the ink-jet printed drops, as can be observed in Figure 5.7(a–b). Single-layer printed drops of THV 20 wt. % in 50–50 vol. % MIBK–acetone had $T_c = (5.91 \pm 0.21) \mu\text{m}$ and $T_e = (6.40 \pm 0.21) \mu\text{m}$. Double-layer drops showed $T_c = (11.84 \pm 0.34) \mu\text{m}$ and $T_e = (12.52 \pm 0.34) \mu\text{m}$.

Films of THV 20 wt. % in 50–50 vol. % MIBK–acetone were ink-jet printed using a drop spacing of $600 \mu\text{m}$, corresponding to a 50% of overlapping. The printed films did not show the coffee ring effect, instead, a slipping pattern was present (see Figure 5.7(c–d)), similarly to the case when THV 10 wt. % in MIBK was used to print films. Single-layer films had $T_c = (14.04 \pm 0.52) \mu\text{m}$, showing a smooth texture with $Sq = (71 \pm 8) \text{nm}$, while double-layer films had $T_c = (28.01 \pm 0.11) \mu\text{m}$ and $Sq = (428 \pm 98) \text{nm}$. Sq was calculated over an area of $(1 \times 1) \text{mm}$ at the centre of the films.

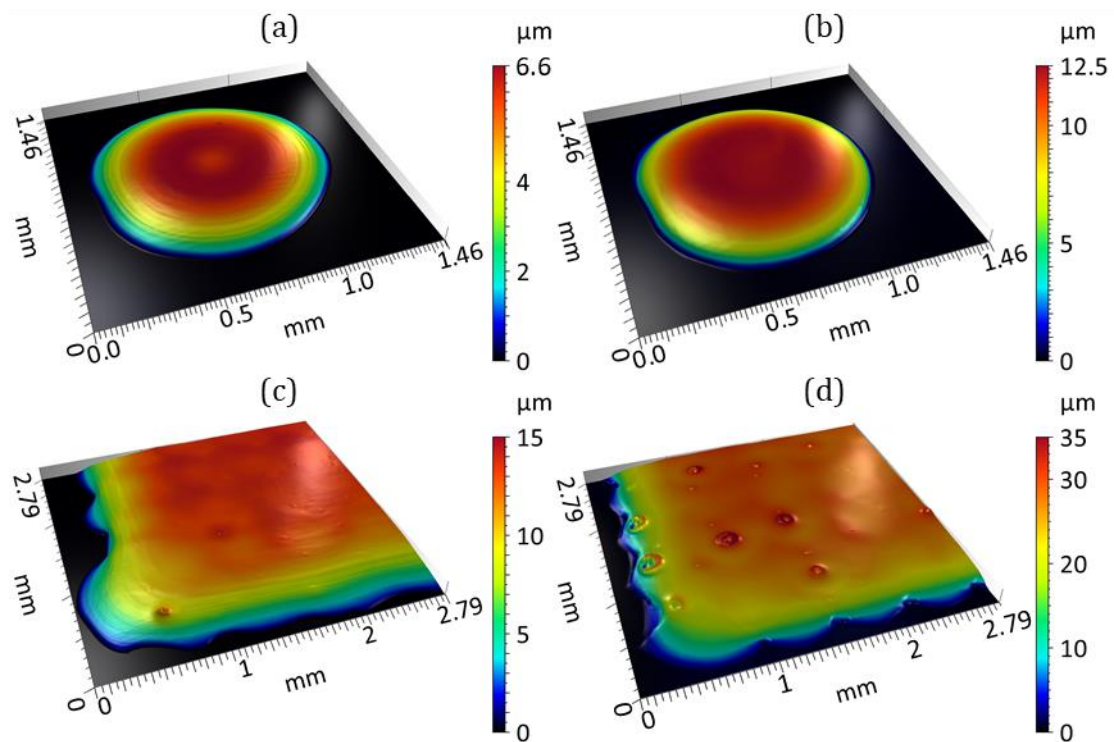


Figure 5.7 Surface topography corresponding to (a) a one-layer drop, (b) a two-layer drop, (c) a one-layer film and (d) a two-layer film of ink-jet printed THV 20 wt. % in 50–50 vol. % MIBK–acetone.

Unlike the case when the THV 10 wt. % in MIBK ink was used, double-layer films of THV 20 wt. % in 50–50 vol. % MIBK–acetone did not show the formation of wrinkle-like features. Instead, the surface topography maps revealed the presence of local cone-shape features (see Figure 5.7(d)), likely caused by the swelling of regions of the previous THV layer during evaporation. Acetone has a faster dissolution rate for THV than MIBK, meaning that less regions would be insufficiently dissolved and, therefore, minimising the formation of wrinkles.

Defects on the surface of multi-layer films can be corrected by subjecting the sample to a heat treatment in a subsequent step. After being heated in an oven at 170 °C for 40 minutes, a ten-layer film with $T_c = (138 \pm 2.35) \mu\text{m}$ showed a smooth texture with $Sq = (84 \pm 9) \text{nm}$ (see Figure 5.8). The latter Sq value is similar to the single-layer result.

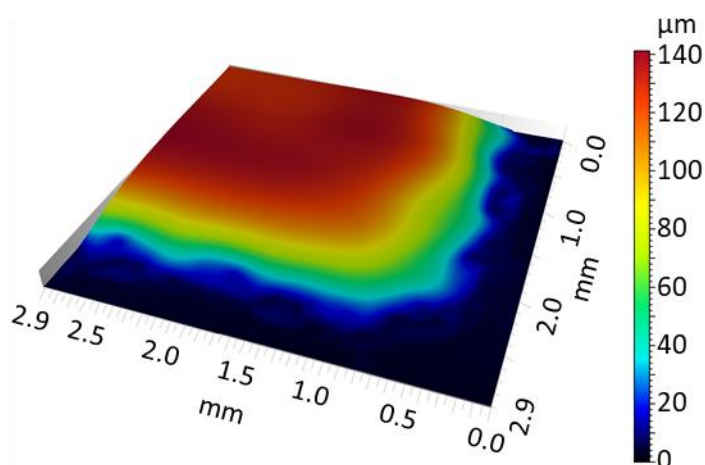


Figure 5.8 Surface topography corresponding to a heat-treated ten-layer film of ink-jet printed THV 20 wt. % in 50–50 vol. % MIBK–acetone.

5.4 Conclusion

This study showed that THV can be ink-jet printed at low and high polymer concentrations, from 1 wt. % to 20 wt. %, to produce protective layers or membranes with thickness of a few nanometres to several micrometres, which may be used to encapsulate drugs and manufacture microfluidic devices. Ink-jet printing of THV also has the potential to be applied to the fabrication of microchannels used in biochips or lab-on-a-chip devices to mix, pump, or control a

biochemical environment. The combination of different printers could allow for both high throughput and high resolution.

This investigation has demonstrated solutions to minimise the coffee ring effect and the formation of wrinkle-like features on the surface when ink-jet printing THV, which should allow the production of films with uniform thickness and surface texture. One way to suppress the coffee ring effect when ink-jet printing THV is to increase the polymer concentration, which consequently increases the viscosity of the ink. A high viscosity slows down the diffusion of particles towards the edges by moderating the outward capillary flow [263]. The latter effect allowed a more even distribution of the solute, as the edges of the drop or film kept receding during evaporation. An alternative way to counter the coffee ring effect and the formation of wrinkle-like features on the surface when ink-jet printing THV is to change the evaporation profile of the ink by using a combination of solvents, as the coffee ring effect is caused by the higher evaporation rate at the edge of the drop or film.

CSI offers sub-nanometre precision along the direction of surface height and sub-micrometre lateral resolution areal surface topography measurement of ink-jet printed transparent polymer parts without any potential damage to the surface. The acquired surface information is essential for providing feedback to the manufacturing process and for quality control of the product.

6 Noise reduction in coherence scanning interferometry

The work presented in this chapter has been published in [264].

6.1 Introduction

As previously discussed in Chapter 3, CSI can measure a variety of surface types, from optically smooth to rough, and surfaces that have large height variations or discontinuities without the 2π ambiguity that can occur with PSI [29, 132]. CSI has found broad applications in the semiconductor, optics, biomedical, automotive, and aerospace industries, including applications that incorporate the characterisation of transparent films and dissimilar materials [202, 203], as well as the surface measurement of additively manufactured components [75, 201]. Reducing measurement noise in CSI is an important consideration when dealing with AM surfaces and other highly complex surfaces, in particular when the ability to capture data is compromised by insufficient signal-to-noise ratios. Surface measurements with nanometre or even sub-nanometre accuracy are required in some applications, as is the case for extreme-ultra violet lithography [193]. In other applications, it is also desirable to measure the surface of a part directly on or close to the production line in the shop floor, e.g., on-machine and in-process surface metrology, such as the precision manufacturing of micro lenses [265]. CSI is a wide-field imaging technique. The images that contain interferograms are sequentially recorded by a camera during the axial scanning process. Each pixel of the camera records a low-coherence interference signal, from which the surface height is calculated corresponding to the lateral position defined by that pixel. Noise in the interferogram at each pixel is translated into height variations in the measured surface topography and is an influence factor that contributes to the uncertainty of surface measurement [89, 94]. Weak signals below the digitization limit can also result in lost or missing data points.

Random topographic measurement noise in CSI in an ideal environment is ultimately limited by the electronic noise in the camera [266, 267]. In practice, it is also important to consider environmental noise generated by floor vibrations, air turbulence, temperature fluctuations, and acoustics [94, 125], as previously discussed in Section 2.2.6.1. Other sources of noise originate from the positioning uncertainty of the piezoelectric scanner [167] and from intensity fluctuations [268]. Although CSI can measure flat surfaces with sub-nanometre precision along the direction of surface height [31], the topographic measurement noise may increase when measuring steeply sloped surfaces [171, 172], or surfaces with low reflectance or significant surface roughness [32, 173]. Low-pass, field-averaging filters can reduce topography noise; however, this practice compromises lateral resolution, and filtering is ineffective at recovering lost data points attributable to weak signals [121].

This study focuses on two physical methods to improve the signal strength and to reduce topographic measurement noise in CSI at the expense of longer data acquisition times: (1) averaging a sequence of repeated surface topography measurements [125], here simply called averaging, and (2) sampling the raw signal data more densely during a single data acquisition, here referred to as oversampling [29, 188]. Although the averaging and oversampling methods are established techniques, there is currently scarce quantitative information available in the literature to guide users as to when to use one or the other of these techniques. The literature is equally silent as to the expectations for improvement for specific environments and part types. It can come as a surprise, for example, that under certain conditions, oversampling of the interferometry signal has no tangible effect on the random noise in the final topography map. In other situations, averaging the topography improves the noise level but does little to capture more information from weakly reflecting surface areas.

The goal of the present investigation is to fill a gap between the theoretical benefits of noise reduction methods and the practical application of these methods in real-world circumstances. An effective illustration of the differences between averaging and oversampling is obtained by measuring a flat surface at different tilt angles. This chapter provides an explanation for the different behaviours observed in the two noise reduction methods when the surface is

tilted. A simple method has been developed to model the effects of averaging and oversampling, where the environment-induced vibration is considered. The results of this study provide guidance for CSI users to choose the appropriate method to reduce measurement uncertainty for a wide range of applications.

6.2 Methods

6.2.1 Topography averaging

A measured surface topography map M as a function of the spatial coordinates (x, y) contains the topographic information $S(x, y)$ and the noise contribution to surface height $f_n(x, y)$, i.e.

$$M(x, y) = S(x, y) + f_n(x, y). \quad (6.1)$$

Here, it is assumed that the systematic measurement errors are either negligible or can be completely corrected, and the distribution of $f_n(x, y)$ has a zero mean. Moreover, the surface measurement is assumed to be an ergodic random process, which means the ensemble average and time average are equal.

The averaging method is based on the creation of a mean surface topography map $\bar{M}(x, y)$ from a sequence of N repeated surface topography measurements $M_i(x, y)$, each acquired at the same position on the sample, one after another in quick succession:

$$\bar{M}(x, y) = \frac{\sum_{i=1}^N M_i(x, y)}{N}. \quad (6.2)$$

Substituting Equation (6.1) into Equation (6.2), and considering that the surface is unchanged during the measurement, gives

$$\bar{M}(x, y) = S(x, y) + \frac{\sum_{i=1}^N f_{n_i}(x, y)}{N}. \quad (6.3)$$

The variance of the difference between the mean surface map \bar{M} and the true topography S gives the variance of the residual surface height deviation,

$$\text{Var}[\bar{M}(x, y) - S(x, y)] = \text{Var}\left[\frac{\sum_{i=1}^N f_{n_i}(x, y)}{N}\right]. \quad (6.4)$$

Assuming the noise is unchanged, it follows that

$$\text{Var}\left[\frac{\sum_{i=1}^N f_{n_i}(x, y)}{N}\right] = \frac{\text{Var}[f_n(x, y)]}{N}. \quad (6.5)$$

This result can be understood by referring to the central limit theorem [269]. Taking the square root of Equation (6.5), the measurement noise of the mean surface topography is calculated as the standard deviation of the residual surface height deviation,

$$\sigma = \frac{\sigma_n}{\sqrt{N}} \quad (6.6)$$

where $\sigma_n = \sqrt{\text{Var}[f_n(x, y)]}$ is the topographic noise of a single surface measurement, i.e. $N = 1$. The topographic measurement noise decreases by the square root of the number of measurements [270].

Since the total data acquisition time for a given averaged measurement is equal to the acquisition time t_0 for a single data acquisition multiplied by N , the topographic measurement noise will be reduced at the expense of longer data acquisition times. Consequently, the topographic noise σ will have an inverse square root dependence on the data acquisition time, i.e.

$$\sigma \propto \frac{1}{\sqrt{t}} \quad (6.7)$$

where $t = N \cdot t_0$ is the total data acquisition time. This behaviour has already been observed in PSI [268] and is a well-known characteristic of position measuring sensors [271, 272].

6.2.2 Oversampling

In CSI, a digital camera captures the height-dependent interference data during an axial scan of the interference objective with respect to the object surface. A

typical interferogram recorded by a pixel is shown in Figure 6.1(a). Usually, four sample points are used for sampling a fringe [157], equivalent to four camera frames per fringe and a sampling distance of $\lambda/8$.

When using oversampling, the number of camera frames per fringe along the axial direction is increased by sampling the fringe at smaller phase increments (see Figure 6.1(b)) [29]. Reducing the sampling distance means a slower scan speed. In the case of oversampling, the integer N is the “oversampling factor” and increases the total data acquisition time in such a way that $t = N \cdot t_0$. The number of camera frames per fringe is then N times the number of camera frames corresponding to a data acquisition that takes t_0 to complete.

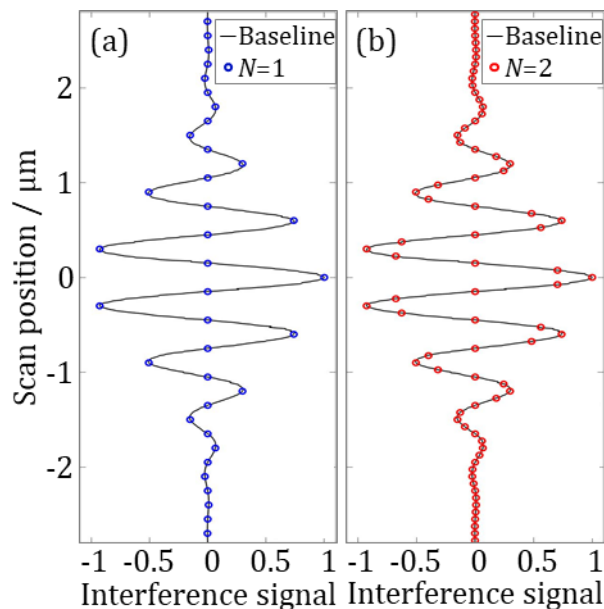


Figure 6.1 CSI signal acquired (a) with a typical sampling rate of four camera frames per fringe and (b) with oversampling at eight frames per fringe ($N = 2$).

Sampling the interferogram with more sample points means the signal can be reconstructed with lower uncertainty, according to the central limit theorem. As with averaging, the measurement noise is expected to be reduced. More importantly, oversampling in CSI enhances the signal-to-noise ratio [188], which can significantly increase the number of valid data points for CSI measurements of surfaces with low reflectance or high roughness and steep slopes, as shown in Chapter 4.

6.2.3 Instrument and materials

A Zygo NexView™ NX2 interference microscope performed the measurements presented in this work. The instrument was located in a metrology laboratory with a controlled temperature of (20 ± 1) °C. The specifications of the investigated objective lenses are shown in Table 6.1.

Table 6.1 Optical parameters for the investigated objective lenses.

Magnification	5.5×	20×
NA	0.15	0.40
Lateral sampling distance / μm	1.56	0.43
FOV / mm	1.56×1.56	0.43×0.43

The object surface for evaluating the measurement noise was a SiC reference flat with a certified RMS roughness of 0.1 nm over a 40 mm aperture. The reference flat was measured at θ tilt angles, where $\theta = 0^\circ, 2^\circ, 4^\circ$. The axial scan range was 100 μm for all the measurements. The data acquisition was completed in approximately 7.5 s at the nominal scan speed of 13.4 $\mu\text{m/s}$. The surface topography was reconstructed using the frequency domain analysis method that uses both the coherence envelope and the phase of the interference fringes to locate the surface [29, 132].

6.2.4 Evaluation of measurement noise

In order to minimise the impact of other systematic errors in CSI, such as lateral distortion [184] and retrace error [181], the central areas of the surface topography maps were extracted for noise evaluation. The size of the extracted area is defined by (500×500) image points, corresponding to (779×779) μm for the case of the 5.5× lens, and (217×217) μm for the case of the 20× lens.

The topographic measurement noise was estimated by the subtraction method [125, 127]. The subtraction method requires two surface topography maps, M_1 and M_2 , respectively, each acquired at the same position on the sample with the

shortest possible time difference between measurements. The resulting difference topography map $\Delta M = M_1 - M_2$ should only contain information about the measurement noise. A high-pass areal Gaussian filter [107] with a cut-off spatial wavelength of 80 μm is applied to ΔM to reduce the residual systematic form errors. The experimental topographic measurement noise σ_e is calculated as the standard deviation of ΔM , which is then divided by the square root of two, thus

$$\sigma_e = \frac{1}{\sqrt{2}} \sqrt{\frac{1}{L_i L_j} \sum_{i=1}^{L_i} \sum_{j=1}^{L_j} \Delta M(x_i, y_j)^2}, \quad (6.8)$$

where $L_{i,j}$ is the total number of image points in x and y directions.

When the averaging method was used, sixteen individual measurements were performed at the nominal scan speed of the instrument. N measured surfaces were averaged to calculate the mean measurement, where $N = 2, 3, \dots, 8$. Two sets of mean measurements were generated to evaluate measurement noise using Equation (6.8). When the oversampling method was used, a series of values for the factor N were considered, where $N = 2, 3, \dots, 8$. For each oversampling factor, two repeated measurements were taken and the topographic measurement noise was evaluated using Equation (6.8).

6.2.5 Noise density

By using the concept of noise density for surface measurement, it is possible to evaluate performance independently of the scan speed and areal filtering [124, 273]. The noise density is defined as

$$\eta_M = \frac{\sigma_e}{\sqrt{P/t}}, \quad (6.9)$$

where σ_e is the topographic measurement noise that can be obtained using Equation (6.8), P is the number of uncorrelated image points in the field of view and t is the total data acquisition time. If a 3×3 pixel denoising filter is used, the nine neighbouring pixels will be correlated, and the number of uncorrelated

image points P will be reduced by a factor of nine. From Equation (6.9), it follows that

$$\sigma = \frac{\beta_M}{\sqrt{t}}, \quad (6.10)$$

where $\beta_M = \eta_M \sqrt{P}$. The coefficient β_M and noise density η_M have the same unit nm/ $\sqrt{\text{Hz}}$. This is a familiar specification for position sensors with nanometre resolution [272].

6.3 Results over a range of surface tilts

6.3.1 Noise as a function of data acquisition time

To begin with, the SiC flat was measured at a 0° tilt angle. The topographic measurement noise showed an inverse square root dependence on the data acquisition time (see Figure 6.2) for both averaging and oversampling methods, in agreement with the result recently reported by de Groot and DiSciaccia [124]. The measurement noise for both objectives when $N = 1$ is of the order of 0.2 nm. The observed measurement noise levels are almost the same for both averaging and oversampling methods.

The surface topography repeatability specification of the CSI instrument is 0.12 nm for the scan speed of $7.2 \mu\text{m/s}$, 1 million image points, with a 3×3 pixel denoising filter engaged. A consistent comparison between this performance specification and our results expressed in terms of noise density η_M is shown in Table 6.2. The small difference in noise level between $5.5\times$ and $20\times$ lenses is likely to be attributable to the differences in instrument setup and in the characteristics of the two lenses, including for example, the fringe contrast.

In this study, the default 3×3 denoising filter of the instrument was disengaged. In principle, a 3×3 filter reduces random pixel noise by a factor of three. Therefore, the noise density for our results is approximately three times the noise density of the manufacturer's specification.

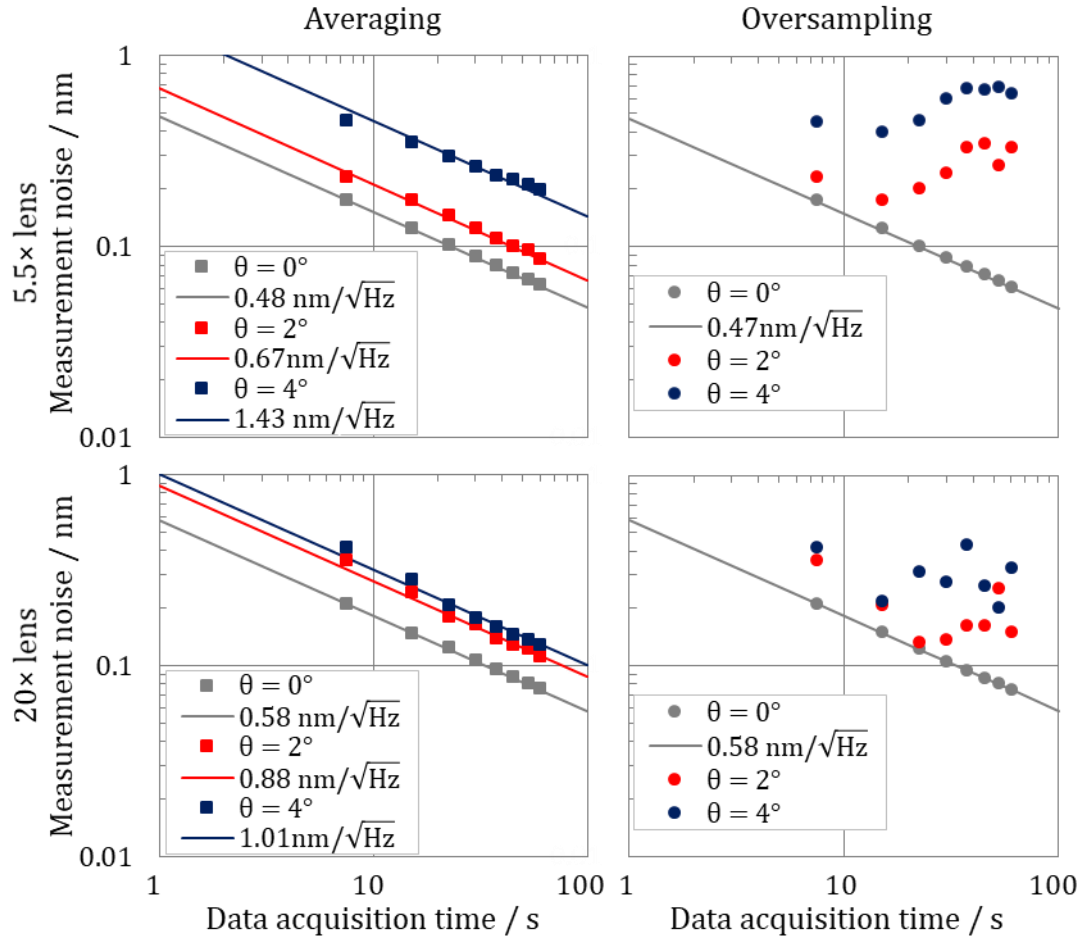


Figure 6.2 Experimental results: measurement noise for the SiC flat measured at a 0° , 2° and 4° tilt angles. Each line corresponds to the least squares fit using Equation (6.10). The coefficient β_M for each fitted line is shown in the legend.

Table 6.2 Noise density for the SiC flat measured at a 0° tilt angle.

Case	σ_e / nm^a	P	$\eta_M / (\text{nm} / \sqrt{\text{Hz}})$
Instrument specification	0.12	110000	0.362×10^{-3}
5.5× lens, averaging	0.48	250000	0.960×10^{-3}
5.5× lens, oversampling	0.47	250000	0.940×10^{-3}
20× lens, averaging	0.58	250000	1.160×10^{-3}
20× lens, oversampling	0.58	250000	1.160×10^{-3}

^aEquivalent to the surface topography repeatability on the instrument specification by definition; σ_e is obtained for data acquisition time $t = 1$ s.

When measuring the flat at a 2° and 4° tilt angles using simple averaging, the measurement noise shows a similar inverse square root dependence on the data

acquisition time relative to the 0° tilt scenario, although at a slightly higher level. In contrast, when using oversampling in place of averaging with the flat at tilted positions, the measurement noise no longer follows the trend of improving with measurement time. The observed phenomena will be discussed further in the following section.

6.3.2 Correlated and uncorrelated noise

The discrepancy in the results for averaging and oversampling are best understood by examining the difference topography maps (i.e. ΔM). Figure 6.3(a) shows the result of subtracting two successive individual images with an oversampling factor $N = 8$, with the sample flat at 0° tilt. Figure 6.3(b) shows the difference map for the same data acquisition parameters but with 4° tilt along the horizontal axis. Figure 6.3(a) shows essentially random noise from pixel to pixel, whereas Figure 6.3(b) shows stripes that are clearly correlated. While the random noise might be expected to be reduced with oversampling, the patterns in Figure 6.3(b) for a tilted flat are unlikely to be reduced and are the result of a disturbance to the scanning motion caused by vibration, acoustics or air turbulence. To test this hypothesis, the vibration was measured separately and the results were simulated.

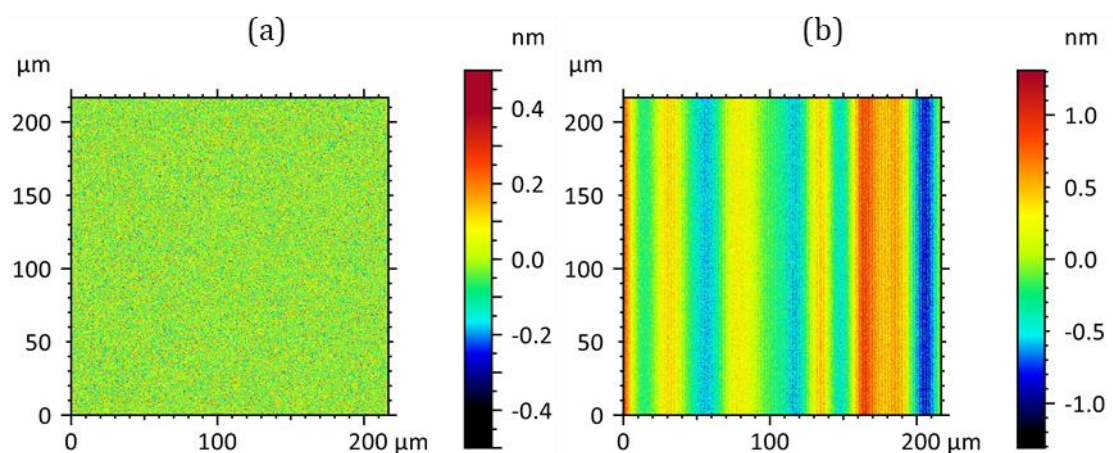


Figure 6.3 Difference between two successive individual measurements acquired using oversampling for the SiC flat at a (a) 0° tilt angle and a (b) 4° tilt angle along the horizontal axis.

6.3.3 Evaluation of environment-induced vibration

The environment-induced vibration was evaluated using the SiC flat as the reference surface. By nulling the fringes and using a carrier fringe technique [230, 231] built into the instrument, the instantaneous position of the reference surface is determined as a function of time. The fastest camera mode available in the instrument was used for the evaluation, which allows a sampling frequency of 800 Hz.

In total, forty repeated tests were performed at the beginning and at the end of each experimental measurement session. Each test consisted of 1024 sampling intervals, recording a time lapse of 1.28 s, as shown in Figure 6.4(a–c). The Fourier transforms of the environment-induced vibration profiles in the time domain provide the corresponding vibration amplitude spectra (see Figure 6.4(d–f)). The vibration amplitude spectra show a resonance spike at 84 Hz which corresponds to the vibration produced by the cooling fans of other systems in the laboratory. Lower spikes were identified at 18 Hz, 198 Hz and 336 Hz, possibly corresponding to the vibration of motorised equipment and machinery operating in the building.

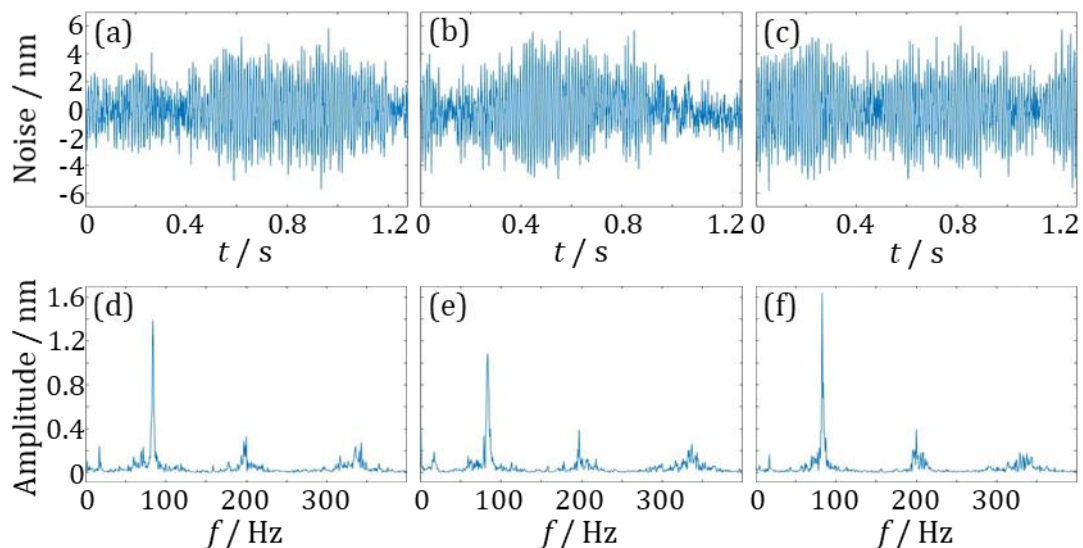


Figure 6.4 Evaluation of the environment-induced vibration. (a–c) Examples of measured environment-induced vibration profiles; (d–f) their corresponding amplitude spectra.

6.3.4 Simulation of surface measurement and environment-induced vibration

The surface measurement is simulated by considering the measured environment-induced vibration to verify the observed different behaviours of the averaging and oversampling methods for tilted surfaces. As a first step, the mean vibration amplitude spectrum is calculated by averaging the forty vibration amplitude spectra (see Figure 6.5(a)). Assuming there are no significant low frequency contributions, the mean vibration amplitude spectrum is interpolated. Then, a random phase (distributed between $-\pi$ and π) is given to each frequency component of the interpolated spectrum. The inverse Fourier transform of the complex-valued spectrum gives a simulated environment-induced vibration profile with increased length in the time domain. This process is repeated to generate a series of simulated environment-induced vibration profiles which have the same spectrum but are different in the time domain.

The simulated environment-induced vibration profile in the time domain is then converted to a spatial signal by multiplying with the axial scan speed of $13.4 \mu\text{m/s}$, to obtain the environment-induced vibration profile as a function of the axial scan position z (Figure 6.5(b)).

To simulate the surface measurement, the nominal surface profile is defined by a sequence of coordinate points (x, z) along the horizontal and vertical axes, respectively. For a flat surface, $z = ax$, where a is the slope and equal to $\tan \theta$. Then, the environment-induced vibration profile is added to the nominal surface profile (see Figure 6.5(c)). The areal surface measurement is simulated by synthesising the replicated simulated profiles along the y direction (see Figure 6.5(d)). Here, it is assumed that the surface points at the same height position experience the same environment-induced vibration.

The difference between the two methods is perhaps best understood by emphasising the difference between noise contributions that are fully random between image points, which is the case for example by the noise contribution from the camera, and noise that is correlated over many pixels. The environment-induced vibration tends to generate correlated noise that may not be improved by lateral filtering or oversampling.

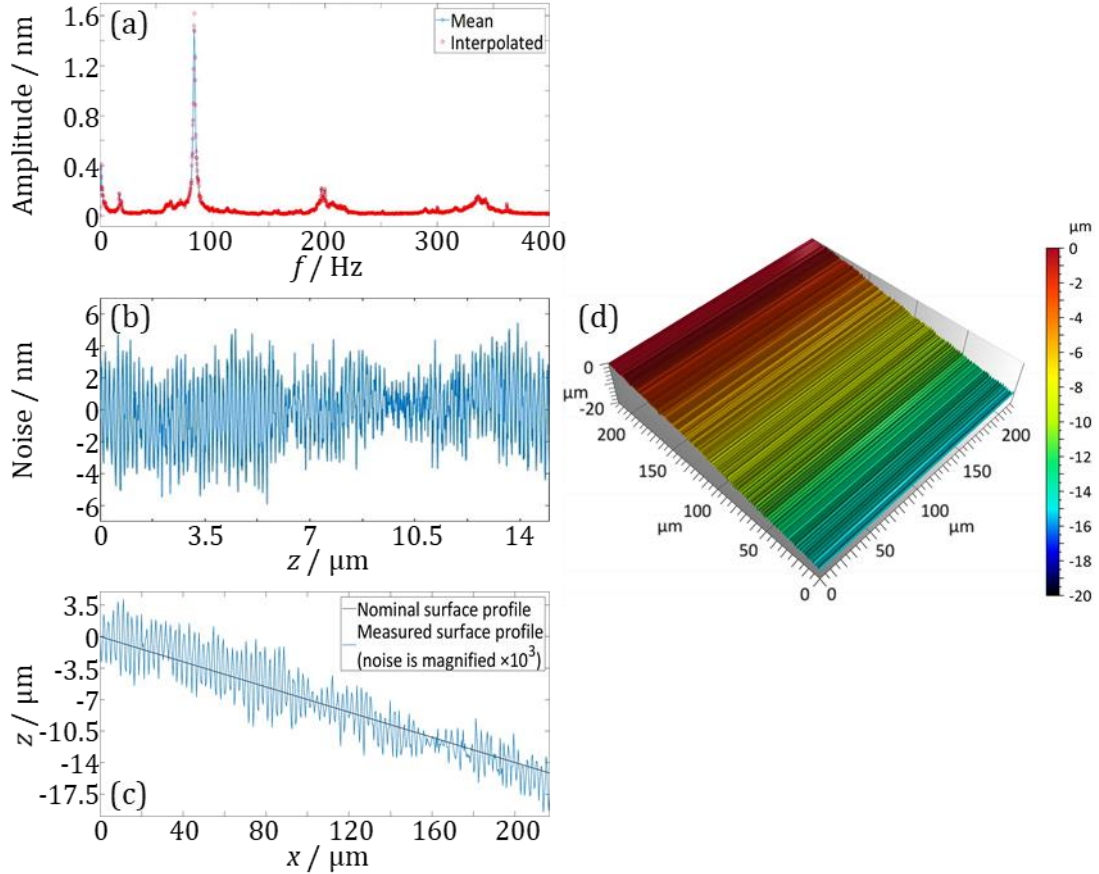


Figure 6.5 Simulation of surface measurement. (a) The mean and interpolated vibration amplitude spectra; (b) an arbitrary simulated environment-induced vibration profile; (c) the (simulated) measured surface profile; (d) the (simulated) areal surface topography measurement.

The averaging and oversampling methods were evaluated using the simulated surface measurement. The simulation is helpful to understand the phenomena that was observed in Section 6.3.1. To keep the simulation consistent with the experimental method, (500×500) surface points were considered, corresponding to $(779 \times 779) \mu\text{m}$ for the case of the $5.5\times$ lens, and $(217 \times 217) \mu\text{m}$ for the case of the $20\times$ lens. The same high-pass areal Gaussian filter (i.e. with a cut-off spatial wavelength of $80 \mu\text{m}$) was applied to the resulting difference topography maps (i.e. ΔM) before using Equation (6.8) for the evaluation of measurement noise.

In the case of a non-tilted flat (i.e. $\theta = 0^\circ$), the nominal surface height would have a constant height value, e.g. $z = 0$, and the simulated environment-induced vibration would also have a constant z value, since it is a function of the vertical scan position z . Disregarding the effects of camera electronic noise, the surface

topography measurement noise would be zero in the simulation of a non-tilted flat.

When simulating the averaging method for a 2° and 4° tilted flat (see Figure 6.6), the measurement noise results show an inverse square root dependence on the data acquisition time, in good agreement with the experimental results. When simulating the oversampling method, the measurement noise does not follow the inverse square root dependence on the data acquisition time, again similar to the experimental results.

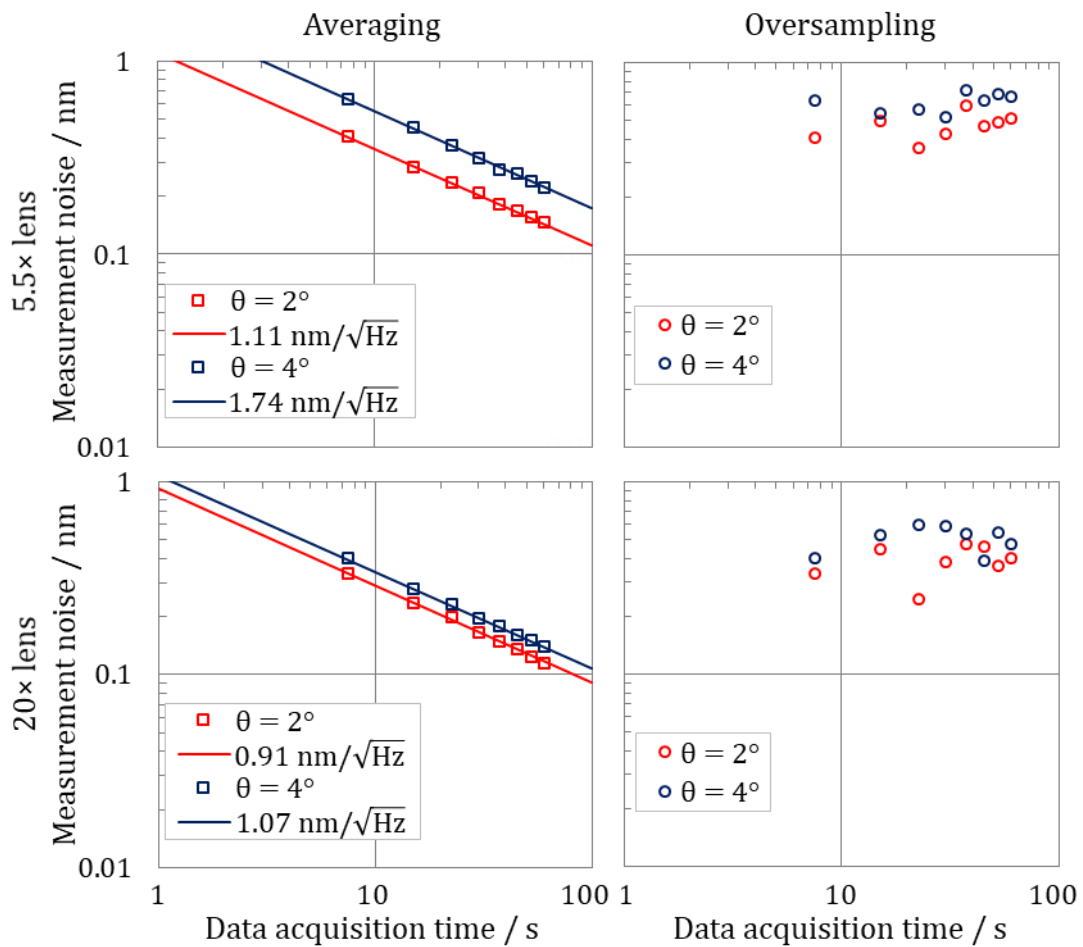


Figure 6.6 Simulation results: measurement noise for a flat surface measured at 2° and 4° tilt angles. Each line corresponds to the least squares fit using Equation (6.10). The coefficient β_M for each fitted line is shown in the legend.

6.4 Conclusion

This investigation contributes to the understanding of the mechanisms of the two noise reduction methods and compares their effects on surface topography measurement in the presence of environmental vibration. It is clear from both experimental and simulation results that the measurement noise levels rise with increasing surface tilt and height variation.

In a recent publication, a comparison of measurement noise was made for a wide range of areal surface topography measurements [274]. The findings of this study show that the measurement noise in a practical measurement may be considerably higher than the noise for a levelled smooth flat, and it may vary significantly over the surface. In the definition of measurement noise, it is somehow implied that its value is constant over the surface. For smooth flat surfaces, this is usually the case, however, for more complex surfaces, the noise may be significantly higher in regions on the surface having irregularities or slopes, causing the measurement noise value to increase.

The topography averaging method is effective for reducing all sources of noise, such as environment-induced vibration and camera noise, regardless of surface tilt. The experiments and simulations presented in this chapter confirm that the noise can be reduced at a rate given by the square root of the number of averages, or equivalently, by the square root of the total data acquisition time. The oversampling method has the same noise reduction effect, but in the presence of vibration, this conclusion is valid only when the part is a flat with zero tilt.

However, these two methods are not simply competing ways to reduce measurement noise. The averaging method reduces noise, but does little to capture more data points. The oversampling method allows to pull weak signals out of noise for each individual data acquisition, e.g. for surfaces with high slopes and roughness, and materials with low reflectivities (as demonstrated in Chapter 4 for the measurement of metal AM parts). Although for such surfaces (or even a tilted flat) the noise reduction effect is compromised for the oversampling method, the benefit of capturing weak signals is preserved. Figure 6.7 illustrates the results of a CSI measurement using oversampling on a metal AM surface

having steep slopes, deep recesses, high aspect-ratio features, as well as regions with a large variation in reflectance. Improvements in signal-to-noise ratios by oversampling can broaden the range of applications to reach those in which the surface structure has previously been considered beyond the capabilities of CSI [124, 188].

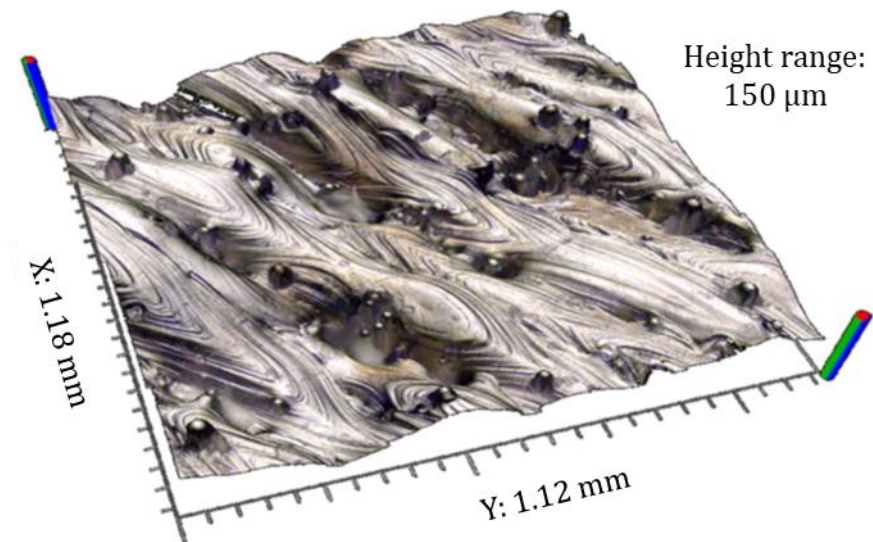


Figure 6.7 True colour surface topography measurement for a Ti-6Al-4V LPBF sample measured with CSI. The measurement represents a 4×4 laterally stitched 3D image for a $50\times$ lens ($NA = 0.55$). Adapted from [45, 124].

7 Conclusions and future work

7.1 Concluding remarks

Typical as-built metal AM surfaces have significant texture and feature a large number of local high slopes and loose particles. In the case of polymer AM, surfaces are often translucent or have low reflectivity. Because of these characteristics, it is challenging for any technique to accurately measure the topography of metal and polymer AM surfaces. Obtaining accurate and repeatable surface topography measurements of manufactured parts is highly important for quality control and manufacturing process improvement.

Due to its significant advantages such as non-contact operation, high precision and high resolution, CSI is regarded as one of the most effective surface topography measurement techniques. However, previous CSI technologies have been challenged when measuring AM surfaces. Recent progress in the development of CSI allows a significantly enhanced detection sensitivity through the use of advanced measurement techniques, such as filtering of the source spectrum, HDR lighting levels, adjustable number of camera acquisitions over each interference fringe (i.e. oversampling), and sophisticated topography reconstruction algorithms.

In this thesis, the effects of advanced measurement functions on the measurement of typical as-built AM surfaces have been empirically investigated and systematically analysed. Guidelines have been provided for the optimisation of the measurement of AM surfaces by considering the total data acquisition time, the size of the measurement area, and the percentage of data coverage. The results reported in Chapter 4 demonstrate that CSI can effectively provide surface topography measurements for AM surfaces with various texture levels and slope distributions.

The detailed surface topography information captured with the use of CSI is essential for providing feedback to the manufacturing process and for quality control of the product. To validate this, a challenging case study has been considered. The feasibility of ink-jet printing a fluoropolymer material (in this case, THV) to produce films of a few nanometres to several micrometres in thickness has been assessed using CSI. The investigation presented in Chapter 5 demonstrates solutions to minimise the 'coffee ring' effect and the formation of undesired wrinkle-like features on the surface when ink-jet printing THV. An effective strategy to suppress the coffee ring effect when ink-jet printing THV is to increase the polymer concentration, which in turn increases the viscosity of the polymer ink. A high viscosity showed to slow down the diffusion of particles towards the edges by moderating the outward capillary flow. The latter effect allowed a more even distribution of the solute, as the edges of the deposited drop or film kept receding during evaporation. Another strategy to mitigate the coffee ring effect and the formation of wrinkle-like features on the surface when ink-jet printing THV is to change the evaporation profile of the ink by using a combination of solvents, as the coffee ring effect is caused by the higher evaporation rate at the edge of the drop or film.

Chapter 5 contributes to the field of polymer AM by providing insight into how to control and optimise the quality of ink-jet printed parts with the aid of surface metrology. In particular, the findings of the research presented in this chapter provide guidance for the ink-jet printing of THV coatings or membranes with uniform thickness and surface texture. Inkjet-printing of THV may be used to encapsulate drugs and to manufacture microfluidic systems, such as biochips or lab-on-a-chip devices to control a biochemical environment.

Reducing measurement noise in CSI is highly important when measuring AM surfaces, particularly when the ability to capture data is affected by poor signal-to-noise ratios. The work presented in Chapter 6 contributes to the understanding of the mechanisms of measurement noise reduction methods and compares their effects when measuring surface topography in the presence of environmental vibration. Both experimental and simulation results have shown with clarity that measurement noise levels exacerbate with increasing surface tilt and height variation. The topography averaging method proved to be successful for reducing

all sources of noise, such as environmental vibration and camera noise, regardless of surface tilt. The experiments and simulations confirm that measurement noise can be effectively reduced at a rate given by the square root of the number of averages, or equivalently, by the square root of the total data acquisition time. On the other hand, the oversampling method has the same measurement noise reduction effect, but in the presence of vibration, this conclusion is valid only when the measured part is a flat with zero tilt.

Nevertheless, the averaging and oversampling methods are not simply competing ways to reduce measurement noise. The averaging method reduces measurement noise, but does little to capture more data points. The oversampling method allows to pull weak signals out of noise for each individual data acquisition, e.g. for surfaces with high slopes and roughness, and materials with low reflectivities. As demonstrated in Chapter 4, oversampling has proven to be a very effective approach for increasing data coverage when measuring AM surfaces. Although for highly irregular or tilted surfaces the noise reduction effect is compromised when implementing the oversampling method, the benefit of capturing weak signals is preserved.

7.2 Areas for future work

The scope of the work presented in this thesis is to demonstrate applications of CSI in AM, not only to determine the feasibility of using CSI for measuring AM surfaces but to show that CSI is a valuable tool for quality control and process optimisation in AM. Although this thesis contributes to the development of guidelines for the measurement of AM surfaces with CSI (see Chapter 4), more efforts are needed towards further expanding these guidelines and establishing comprehensive good practice in how to optimise a measurement.

An area that still offers plenty of opportunities to carry out relevant research is the correlation of surface topography with AM processing parameters [275-277]. As demonstrated in Chapter 5, topographic information can be used to provide feedback to the manufacturing process.

The results presented in Chapter 6 showed that the difference between successive measurements on complex surfaces may have correlated errors over the FOV and over time. While measurement noise is usually modelled as completely random, it is clear from the aforementioned observation that measurement noise values will be strongly dependent on the specific measurement conditions, such as surface texture, surface slope, environmental vibration, thermal drifts and other influence factors affecting the measurement result. Therefore, another relevant area for potential future work is the empirical evaluation of the performance of CSI (as well as other surface metrology instruments) in real-world applications, i.e. measuring the actual part of interest, in the actual environment in which the instrument is intended to be used. Such evaluations can be done through the implementation of gauge repeatability and reproducibility (GR&R) studies [278, 279]. Along the way, other metrological characteristics (e.g. amplification coefficient, linearity deviation and topography fidelity) could be considered in order to achieve a more comprehensive measurement performance verification and traceability framework for the calibration of CSI.

Finally, despite the significant progress and developments during the past two decades in CSI technology, there are still challenges to meet the ever-increasing measurement requirements in noise robustness, accuracy and speed, particularly in on-machine and in-situ measurement conditions. On-machine surface metrology for AM [280] and conventional manufacturing is an area of great interest since it allows immediate surface measurement after (or before) the manufacturing process without removing or repositioning the workpiece, replacing the traditional post-process inspection carried on a stand-alone surface measuring instrument. The term 'on-machine' refers to the measurement of the workpiece surface directly on the machine where the workpiece has been manufactured, whereas the term 'in-situ' refers to the measurement of the workpiece surface within the same work floor, without isolating the workpiece from the manufacturing environment [265]. In both cases, the measurement process can suffer from significant environmental disturbances, requiring the development of adequate methods to effectively mitigate the influence of such.

References

1. Thompson, M. K., Moroni, G., Vaneker, T., Fadel, G., Campbell, R. I., Gibson, I., Bernard, A., Schulz, J., Graf, P., Ahuja, B. and Martina, F., *Design for Additive Manufacturing: Trends, opportunities, considerations, and constraints*. CIRP Annals, 2016. **65**(2): p. 737-760.
2. Gibson, I., Rosen, D. and Stucker, B., *Additive manufacturing technologies : 3D printing, rapid prototyping, and direct digital manufacturing*. 2015, Springer: New York, NY. p. 1 online resource (xxi, 498 pages).
3. Sidambe, A. T., *Biocompatibility of Advanced Manufactured Titanium Implants-A Review*. Materials (Basel), 2014. **7**(12): p. 8168-8188.
4. Tepylo, N., Huang, X. and Patnaik, P. C., *Laser-Based Additive Manufacturing Technologies for Aerospace Applications*. Advanced Engineering Materials, 2019. **21**(11).
5. Mellor, S., Hao, L. and Zhang, D., *Additive manufacturing: A framework for implementation*. International Journal of Production Economics, 2014. **149**: p. 194-201.
6. Petrovic, V., Haro Gonzalez, J. V., Jordá Ferrando, O., Delgado Gordillo, J., Blasco Puchades, J. R. and Portolés Griñan, L., *Additive layered manufacturing: sectors of industrial application shown through case studies*. International Journal of Production Research, 2010. **49**(4): p. 1061-1079.
7. Achillas, C., Aidonis, D., Iakovou, E., Thymianidis, M. and Tzetzis, D., *A methodological framework for the inclusion of modern additive manufacturing into the production portfolio of a focused factory*. Journal of Manufacturing Systems, 2015. **37**: p. 328-339.
8. Townsend, A., Senin, N., Blunt, L., Leach, R. K. and Taylor, J. S., *Surface texture metrology for metal additive manufacturing: a review*. Precision Engineering, 2016. **46**: p. 34-47.
9. Leach, R. K., Bourell, D., Carmignato, S., Donmez, A., Senin, N. and Dewulf, W., *Geometrical metrology for metal additive manufacturing*. CIRP Annals, 2019. **68**(2): p. 677-700.
10. Khairallah, S. A., Anderson, A. T., Rubenchik, A. and King, W. E., *Laser powder-bed fusion additive manufacturing: Physics of complex melt flow and formation mechanisms of pores, spatter, and denudation zones*. Acta Materialia, 2016. **108**: p. 36-45.

11. DebRoy, T., Wei, H. L., Zuback, J. S., Mukherjee, T., Elmer, J. W., Milewski, J. O., Beese, A. M., Wilson-Heid, A., De, A. and Zhang, W., *Additive manufacturing of metallic components – Process, structure and properties*. Progress in Materials Science, 2018. **92**: p. 112-224.
12. Pellegrino, J., Makila, T., McQueen, S. and Taylor, E., *Measurement Science Roadmap for Polymer-Based Additive Manufacturing*, in *Advanced Manufacturing Series 100-5*. 2016, National Institute of Standards and Technology: Columbia, Maryland.
13. Leach, R. K. and Carmignato, S., *Precision Metal Additive Manufacturing*. 2020, Milton, UNITED KINGDOM: Taylor & Francis Group.
14. Saxon, D. *In praise of Lord Kelvin*. Physics World, 2007. **Stars and Solar Physics**.
15. Launhardt, M., Wörz, A., Loderer, A., Laumer, T., Drummer, T., Hausotte, T. and Schmidt, M., *Detecting surface roughness on SLS parts with various measuring techniques*. Polymer Testing, 2016. **53**: p. 217-226.
16. Ligon, S. C., Liska, R., Stampfl, J., Gurr, M. and Mulhaupt, R., *Polymers for 3D Printing and Customized Additive Manufacturing*. Chem Rev, 2017. **117**(15): p. 10212-10290.
17. de Pastre, M.-A., Thompson, A., Quinsat, Y., Albajez García, J. A., Senin, N. and Leach, R. K., *Polymer powder bed fusion surface texture measurement*. Measurement Science and Technology, 2020. **31**(5).
18. de Groot, P., *Coherence scanning interferometry*, in *Optical Measurement of Surface Topography*, R. Leach, Editor. 2011, Springer-Verlag: Berlin, Heidelberg. p. 187-208.
19. ISO 25178-604:2013 *Geometrical product specifications (GPS)—surface texture: areal—part 604: nominal characteristics of non-contact (coherence scanning interferometry) instruments*. International Organisation for Standardisation, Geneva.
20. Helmlí, F., *Focus Variation Instruments*, in *Optical Measurement of Surface Topography*, R. K. Leach, Editor. 2011, Springer-Verlag: Berlin, Heidelberg. p. 131-166.
21. ISO 25178-606:2015 *Geometrical product specifications (GPS)—surface texture: areal—part 606: nominal characteristics of non-contact (focus variation) instruments*. International Organisation for Standardisation, Geneva.
22. Artigas, R., *Imaging Confocal Microscopy*, in *Optical Measurement of Surface Topography*. R. K. Leach, Editor. 2011, Springer-Verlag: Berlin, Heidelberg. p. 237-286.

23. ISO 25178-607:2019 *Geometrical product specifications (GPS)—surface texture: areal — part 607: nominal characteristics of non-contact (confocal microscopy) instruments*. International Organisation for Standardisation, Geneva.
24. Leach, R. K., *Optical Measurement of Surface Topography*. 2011, Springer-Verlag: Berlin, Heidelberg.
25. Leach, R. K., *Fundamental principles of engineering nanometrology*, in *Micro & nano technologies series*. 2014, Elsevier: Oxford.
26. Hariharan, P., *Optical Interferometry*. 2nd ed. 2003: Academic Press.
27. de Groot, P., *Phase Shifting Interferometry*, in *Optical Measurement of Surface Topography*, R. K. Leach, Editor. 2011, Springer-Verlag: Berlin. p. 167-86.
28. de Groot, P., *A review of selected topics in interferometric optical metrology*. Rep Prog Phys, 2019. **82**(5): p. 056101.
29. de Groot, P., *Principles of interference microscopy for the measurement of surface topography*. Advances in Optics and Photonics, 2015. **7**(1).
30. Petzing, J., Coupland, J. and Leach, R. K., *The measurement of rough surface topography using coherence scanning interferometry*, in *NPL measurement good practice guide no.116*. 2010, National Physical Laboratory: Teddington.
31. Leach, R. K., Brown, L., Xiangqian, J., Blunt, R., Conroy, M. and Mauger, D., *Guide to the measurement of smooth surface topography using coherence scanning interferometry*, in *NPL measurement good practice guide no. 108*. 2008, National Physical Laboratory: Teddington.
32. Liu, M., Cheung, C. F., Ren, M. and Cheng, C. H., *Estimation of measurement uncertainty caused by surface gradient for a white light interferometer*. Appl Opt, 2015. **54**(29): p. 8670-7.
33. ISO/ASTM 52900:2015 *Additive manufacturing—general principles—terminology*. International Organisation for Standardisation, Geneva.
34. ISO 17296-2:2015 *Additive manufacturing—general principles—part 2: overview of process categories and feedstock*. International Organisation for Standardisation, Geneva.
35. Bourell, D., Kruth, J.-P., Leu, M., Levy, G., Rosen, D., Beese, A. M. and Clare, A., *Materials for additive manufacturing*. CIRP Annals, 2017. **66**(2): p. 659-681.
36. Campbell, I., Diegel, O., Huff, R., Kowen, J., Wohlers, T., Bourell, D., Fidan, I. and Sander, P., *Wohlers report 2020 : 3D printing and additive manufacturing global state of the industry*. 2020, Fort Collins, Colorado.: Wohlers Associates, Inc. 343 pages.

37. Ahuja, B., Karg, M. and Schmidt, M., *Additive manufacturing in production: challenges and opportunities*. SPIE LASE. Vol. 9353. 2015: SPIE.
38. Energetics Incorporated, *Measurement Science Roadmap for Metal-Based Additive Manufacturing*. 2013, National Institute of Standards and Technology: Columbia, Maryland.
39. Frazier, W. E., *Metal Additive Manufacturing: A Review*. Journal of Materials Engineering and Performance, 2014. **23**(6): p. 1917-1928.
40. Herzog, D., Seyda, V., Wycisk, E. and Emmelmann, C., *Additive manufacturing of metals*. Acta Materialia, 2016. **117**: p. 371-392.
41. Leal, R., Barreiros, F. M., Alves, L., Romeiro, F., Vasco, J. C., Santos, M. and Marto, C., *Additive manufacturing tooling for the automotive industry*. The International Journal of Advanced Manufacturing Technology, 2017. **92**(5-8): p. 1671-1676.
42. Weissmann, V., Drescher, P., Seitz, H., Hansmann, H., Bader, R., Seyfarth, A., Klinder, A. and Jonitz-Heincke A., *Effects of Build Orientation on Surface Morphology and Bone Cell Activity of Additively Manufactured Ti6Al4V Specimens*. Materials (Basel), 2018. **11**(6).
43. Huang, S., Sing, S. L., de Looze, G., Wilson, R. and Yeong, W. Y., *Laser powder bed fusion of titanium-tantalum alloys: Compositions and designs for biomedical applications*. J Mech Behav Biomed Mater, 2020. **108**: p. 103775.
44. Sames, W. J., List, F. A., Pannala, S., Dehoff, R. R. and Babu, S. S., *The metallurgy and processing science of metal additive manufacturing*. International Materials Reviews, 2016. **61**(5): p. 315-360.
45. DiSciacca, J., Gomez, C., Thompson, A., Lawes, S., Leach, R. K., Colonna de Lega, X. and de Groot, P., *True-color 3D surface metrology for additive manufacturing using interference microscopy*. in *Special Interest Group Meeting: Dimensional Accuracy and Surface Finish in Additive Manufacturing*. 2017. Leuven, Belgium.
46. Aboulkhair, N. T., Everitt, N. M., Ashcroft, I. and Tuck, C., *Reducing porosity in AlSi10Mg parts processed by selective laser melting*. Additive Manufacturing, 2014. **1-4**: p. 77-86.
47. Liu, S. and Shin, Y. C., *Additive manufacturing of Ti6Al4V alloy: A review*. Materials & Design, 2019. **164**.
48. Senin, N., Thompson, A. and Leach, R. K., *Feature-based characterisation of signature topography in laser powder bed fusion of metals*. Measurement Science and Technology, 2018. **29**(4).
49. Thijs, L., Kempen, K., Kruth, J.-P. and Humbeeck, J. V., *Fine-structured aluminium products with controllable texture by selective laser melting of pre-alloyed AlSi10Mg powder*. Acta Materialia, 2013. **61**(5): p. 1809-1819.

50. Scharowsky, T., Bauereiß, A. and Körner, C., *Influence of the hatching strategy on consolidation during selective electron beam melting of Ti-6Al-4V*. The International Journal of Advanced Manufacturing Technology, 2017. **92**(5-8): p. 2809-2818.
51. Matthews, M. J., Guss, G., Khairallah, S. A., Rubenchik, A. M., Depond, P. J. and King, W. E., *Denudation of metal powder layers in laser powder bed fusion processes*. Acta Materialia, 2016. **114**: p. 33-42.
52. Simonelli, M., Tuck, C., Aboulkhair, N. T., Maskery, I., Ashcroft, I., Wildman, R. D. and Hague, R., *A Study on the Laser Spatter and the Oxidation Reactions During Selective Laser Melting of 316L Stainless Steel, Al-Si10-Mg, and Ti-6Al-4V*. Metallurgical and Materials Transactions A, 2015. **46**(9): p. 3842-3851.
53. Mumtaz, K. and Hopkinson, N., *Top surface and side roughness of Inconel 625 parts processed using selective laser melting*. Rapid Prototyping Journal, 2009. **15**(2): p. 96-103.
54. Safdar, A., He, H. Z. and Wei, L.-Y., *Effect of process parameters settings and thickness on surface roughness of EBM produced Ti-6Al-4V*. Rapid Prototyping Journal, 2012. **18**(5): p. 401-408.
55. Strano, G., Hao, L., Everson, R. M. and Evans, K. E., *Surface roughness analysis, modelling and prediction in selective laser melting*. Journal of Materials Processing Technology, 2013. **213**(4): p. 589-597.
56. Cabanettes, F., Joubert, A., Chardon, G., Dumas V., Rech, J., Grosjean, C. and Dimkovski, Z., *Topography of as built surfaces generated in metal additive manufacturing: A multi scale analysis from form to roughness*. Precision Engineering, 2018. **52**: p. 249-265.
57. Fox, J. C., Moylan, S. P. and Lane, B. M., *Effect of Process Parameters on the Surface Roughness of Overhanging Structures in Laser Powder Bed Fusion Additive Manufacturing*. Procedia CIRP, 2016. **45**: p. 131-134.
58. Tian, Y., Tomus, D., Rometsch, P. and Wu, X., *Influences of processing parameters on surface roughness of Hastelloy X produced by selective laser melting*. Additive Manufacturing, 2017. **13**: p. 103-112.
59. Chen, Z., Wu, X., Tomus, D. and Davies, C. H. J., *Surface roughness of Selective Laser Melted Ti-6Al-4V alloy components*. Additive Manufacturing, 2018. **21**: p. 91-103.
60. Zhang, Y., Jarosinski, W., Jung, Y.-G. and Zhang, J., *Additive manufacturing processes and equipment*, in *Additive Manufacturing*. 2018. p. 39-51.
61. Martin, G. D., Hoath, S. D. and Hutchings, I. M., *Inkjet printing - the physics of manipulating liquid jets and drops*. Journal of Physics: Conference Series, 2008. **105**.

62. Guo, Y., Patanwala, H. S. and Bogner, B., *Inkjet and inkjet-based 3D printing: connecting fluid properties and printing performance*. Rapid Prototyping Journal, 2017. **23**(3): p. 562-576.
63. Tekin, E., de Gans, B.-J. and Schubert, U. S., *Ink-jet printing of polymers - from single dots to thin film libraries*. Journal of Materials Chemistry, 2004. **14**(17).
64. Yun, Y. H., Kim, J. D., Lee, B. K. and Cho, Y. W., *Polymer inkjet printing: Construction of three-dimensional structures at micro-scale by repeated lamination*. Macromolecular Research, 2009. **17**(3): p. 197-202.
65. Sirringhaus, H., Kawase, T., Friend, R. H., Shimoda, T., Inbasekaran, M., Wu, W. and Woo, E. P., *High-resolution inkjet printing of all-polymer transistor circuits*. Science, 2000. **290**(5499): p. 2123-6.
66. Shimoda, T., Morii, K., Seki, S. and Kiguchi, H., *Inkjet Printing of Light-Emitting Polymer Displays*. MRS Bulletin, 2011. **28**(11): p. 821-827.
67. Haskal, E. I., Büchel, M., Duineveld, P. C., Sempel, A. and van de Weijer, P., *Passive-Matrix Polymer Light-Emitting Displays*. MRS Bulletin, 2011. **27**(11): p. 864-869.
68. Lan, L., Zou, J., Jiang, C., Liu, B., Wang, L. and Peng, J., *Inkjet printing for electroluminescent devices: emissive materials, film formation, and display prototypes*. Frontiers of Optoelectronics, 2017. **10**(4): p. 329-352.
69. Hoth, C. N., Choulis, S. A., Schilinsky, P. and Brabec, C. J., *High Photovoltaic Performance of Inkjet Printed Polymer:Fullerene Blends*. Advanced Materials, 2007. **19**(22): p. 3973-3978.
70. Thuau, D., Kallitsis, K., Dos Santos, F. D. and Hadziioannou, G., *All inkjet-printed piezoelectric electronic devices: energy generators, sensors and actuators*. Journal of Materials Chemistry C, 2017. **5**(38): p. 9963-9966.
71. Haque, R. I., Vié, R., Germainy, M., Valbin, L., Benaben, P. and Boddaert, X., *Inkjet printing of high molecular weight PVDF-TrFE for flexible electronics*. Flexible and Printed Electronics, 2015. **1**(1).
72. Wiley-VCH, *Ullmann's polymers and plastics: products and processes*. 2016, Wiley-VCH: Weinheim. p. 1 online resource.
73. Tato, W., Blunt, L., Llavori, I., Aginagalde, A., Townsend, A. and Zabala, A., *Surface integrity of additive manufacturing parts: a comparison between optical topography measuring techniques*. Procedia CIRP, 2020. **87**: p. 403-408.
74. Senin, N., Thompson, A. and Leach, R. K., *Characterisation of the topography of metal additive surface features with different measurement technologies*. Measurement Science and Technology, 2017. **28**(9).

75. Gomez, C., Su, R., Thompson, A., DiSciacca, J., Lawes, S. and Leach, R. K., *Optimization of surface measurement for metal additive manufacturing using coherence scanning interferometry*. *Optical Engineering*, 2017. **56**(11): p. 111714.
76. Newton, L., Senin, N., Gomez, C., Danzl, R., Helml, F., Blunt, L. and Leach, R. K., *Areal topography measurement of metal additive surfaces using focus variation microscopy*. *Additive Manufacturing*, 2019. **25**: p. 365-389.
77. Thompson, A., Senin, N., Giusca, C. L. and Leach, R. K., *Topography of selectively laser melted surfaces: A comparison of different measurement methods*. *CIRP Annals*, 2017. **66**(1): p. 543-546.
78. Leach, R., Weckenmann, A., Coupland, J. and Hartmann, W., *Interpreting the probe-surface interaction of surface measuring instruments, or what is a surface?* *Surface Topography: Metrology and Properties*, 2014. **2**(3).
79. Leach, R. K., *Characterisation of areal surface texture*, R. K. Leach, Editor. 2013, Springer-Verlag: Berlin, Heidelberg.
80. Leach, R. K., *Surface Texture*, in *CIRP Encyclopedia of Production Engineering*, L. Laperrière, and G. Reinhart, Editors. 2014, Springer: Berlin, Heidelberg. p. 1-4.
81. Reason, R. E., *Stylus methods of surface measurement*. *Physics Bulletin*, 1973. **24**(10): p. 587-589.
82. Whitehouse, D. J., *Surfaces and their measurement*. 2002, London: Hermes Penton Science.
83. Whitehouse, D. J., *Handbook of Surface and Nanometrology*. 2010, Baton Rouge, UNITED STATES: Taylor & Francis Group.
84. Leach, R. K., *Terms and definitions*, in *Advances in Optical Surface Texture Metrology*. 2020.
85. Griffiths, B., *Manufacturing surface technology : surface integrity & functional performance*. 2001, London: Penton.
86. Jawahir, I. S., Brinksmeier, E., M'Saoubi, R., Aspinwall, D. K., Outeiro, J. C., Meyer, D., Umbrello, D. and Jayal, A. D., *Surface integrity in material removal processes: Recent advances*. *CIRP Annals*, 2011. **60**(2): p. 603-626.
87. Coblas, D. G., Fatu, A., Maoui, A. and Hajjam, M., *Manufacturing textured surfaces: State of art and recent developments*. *Proceedings of the Institution of Mechanical Engineers, Part J: Journal of Engineering Tribology*, 2014. **229**(1): p. 3-29.
88. Bodschwinn, H. and Seewig, J., *Topography of Engineering Surfaces*, in *Encyclopedia of Tribology*, Q.J. Wang and Y.-W. Chung, Editors. 2013, Springer US: Boston, MA. p. 3701-3706.

89. Leach, R. K., Giusca, C. L., Haitjema, H., Evans, C. and Jiang X., *Calibration and verification of areal surface texture measuring instruments*. CIRP Annals, 2015. **64**(2): p. 797-813.
90. ISO 25178-6:2010 *Geometrical product specifications (GPS)—surface texture: areal—part 6: classification of methods for measuring surface texture*. International Organisation for Standardisation, Geneva.
91. ISO 3274:1998 *Geometrical product specifications (GPS)—surface texture: profile method—nominal characteristics of contact (stylus) instruments*. International Organisation for Standardisation, Geneva.
92. Eastman, J. and Zavislan, J., *A New Optical Surface Microprofiling Instrument*. 27th Annual Technical Symposium. Vol. 0429. 1983: SPIE.
93. Berglund, J., Söderberg, R., Wärmefjord, K., Leach, R. K. and Morse, E., *Functional tolerancing of surface texture – a review of existing methods*. Procedia CIRP, 2020. **92**: p. 230-235.
94. ISO 25178-600:2019 *Geometrical product specifications (GPS)—surface texture: areal—part 600: metrological characteristics for areal topography measuring methods*. International Organisation for Standardisation, Geneva.
95. Leach, R. K., *The measurement of surface texture using stylus instruments, in NPL measurement good practice guide no. 37*. 2014, National Physical Laboratory: Teddington.
96. ISO 25178-601:2010 *Geometrical product specifications (GPS)—surface texture: areal—part 601: nominal characteristics of contact (stylus) instruments*. International Organisation for Standardisation, Geneva.
97. Song, J., Renegar, T. B., Soons, J., Muralikrishnan, B., Villarrubia, J., Zheng, A. and Vorburger, T. V., *The effect of tip size on the measured Ra of surface roughness specimens with rectangular profiles*. Precision Engineering, 2014. **38**(1): p. 217-220.
98. Leach, R. K. and Haitjema, H., *Bandwidth characteristics and comparisons of surface texture measuring instruments*. Measurement Science and Technology, 2010. **21**(3).
99. McCool, J. I., *Assessing the Effect of Stylus Tip Radius and Flight on Surface Topography Measurements*. Journal of Tribology, 1984. **106**(2): p. 202-209.
100. Smith, W. J., *Modern optical engineering : the design of optical systems*. 4th ed. ed. 2008, New York: New York : McGraw-Hill.
101. ISO 25178-603:2013 *Geometrical product specifications (GPS)—surface texture: areal—part 603: nominal characteristics of noncontact (phase-shifting interferometric microscopy) instruments*. International Organisation for Standardisation, Geneva.

102. Mignot, C., *Color (and 3D) for Scanning Electron Microscopy*. Microscopy Today, 2018. **26**(3): p. 12-17.
103. Thompson, A., Maskery, I., and Leach, R. K., *X-ray computed tomography for additive manufacturing: a review*. Measurement Science and Technology, 2016. **27**(7).
104. Jiang, X. and Scott, P. J., *Surface Texture Filtering*, in *CIRP Encyclopedia of Production Engineering*, S. Chatti, et al., Editors. 2019, Springer Berlin Heidelberg: Berlin, Heidelberg. p. 1674-1685.
105. ISO 25178-2:2012 *Geometrical product specifications (GPS)—surface texture: areal—part 2: terms, definitions and surface texture parameters*. International Organisation for Standardisation, Geneva.
106. ISO 25178-3:2012 *Geometrical product specifications (GPS)—surface texture: areal—part 3: specification operators*. International Organisation for Standardisation, Geneva.
107. ISO 16610-61:2015 *Geometrical product specification (GPS)—filtration—part 61: linear areal filters—gaussian filters*. International Organisation for Standardisation, Geneva.
108. ISO 4287:1998+A1:2009 *Geometrical product specifications (GPS)—surface texture: profile method—terms, definitions and surface texture parameters*. International Organisation for Standardisation, Geneva.
109. Blunt, L. and Jiang, X., *Numerical Parameters for Characterisation of Topography*, in *Advanced Techniques for Assessment Surface Topography*, L. Blunt and X. Jiang, Editors. 2003, Kogan Page Science: Oxford. p. 17-41.
110. JCGM 100:2008 *Evaluation of measurement data — Guide to the expression of uncertainty in measurement*. Joint Committee for Guides in Metrology, Geneva.
111. JCGM 200:2012 *International vocabulary of metrology – Basic and general concepts and associated terms (VIM)*. Joint Committee for Guides in Metrology, Geneva.
112. BIPM. *SI Brochure 2019: The International System of Units (SI)*. 2020/08/20. 9th edition: (Available from: <https://www.bipm.org/en/publications/si-brochure/>).
113. Carmignato, S., De Chiffre, L., Bosse, H., Leach, R. K., Balsamo, A. and Estler, W. T., *Dimensional artefacts to achieve metrological traceability in advanced manufacturing*. CIRP Annals, 2020.
114. Haitjema, H., *Uncertainty in measurement of surface topography*. Surface Topography: Metrology and Properties, 2015. **3**(3).

115. Leach, R., Haitjema, H., Su, R. and Thompson, A., *Metrological characteristics for the calibration of surface topography measuring instruments: a review*. Measurement Science and Technology, 2021. **32**(3).
116. ISO 25178-70:2014 *Geometrical product specification (GPS)—surface texture: areal part 70: material measures*. International Organisation for Standardisation, Geneva.
117. ISO 25178-602:2010 *Geometrical product specifications (GPS)—surface texture: areal—part 602: nominal characteristics of non-contact (confocal chromatic probe) instruments*. International Organisation for Standardisation, Geneva.
118. ISO 25178-605:2011 *Geometrical product specifications (GPS)—surface texture: areal—part 605: nominal characteristics of non-contact (point autofocus probe) instruments*. International Organisation for Standardisation, Geneva.
119. ISO-DIS 25178-700:2020 *Geometric Product Specifications (GPS) — Surface texture: Areal — Part 700: Calibration, adjustment and verification of areal topography measuring instruments*. International Organisation for Standardisation.
120. Nimishakavi, L.P.J., C. W.; Giusca, C. L. *NPL Areal Standard: a multi-function calibration artefact for surface topography measuring instruments*. in *Proc. Lamdamap XIII*. 2019. Sheffield, UK.
121. de Groot, P., *Progress in the specification of optical instruments for the measurement of surface form and texture*, in *Dimensional Optical Metrology and Inspection for Practical Applications III*, K. Harding, T. Yoshizawa, and S. Zhang, Editors. 2014.
122. de Groot, P., *The meaning and measure of vertical resolution in optical surface topography measurement*. Applied Sciences, 2017. **7**(1).
123. Usher, M. J., *Noise and bandwidth*. Journal of Physics E: Scientific Instruments, 1974. **7**(12): p. 957-961.
124. de Groot, P. and DiSciaccia, J., *Definition and evaluation of topography measurement noise in optical instruments*. Optical Engineering, 2020. **59**(06).
125. Giusca, C. L., Leach, R. K., Helary, F., Gutauskas, T. and Nimishakavi, L., *Calibration of the scales of areal surface topography-measuring instruments: part 1. Measurement noise and residual flatness*. Measurement Science and Technology, 2012. **23**(3).
126. Creath, K. and Wyant, J. C., *Absolute measurement of surface roughness*. Applied Optics, 1990. **29**(26): p. 3823-3827.
127. Verein Deutscher Ingenieure/Verband der Elektrotechnik, Elektronik und Informationstechnik, *VDI/VDE 2655 Part 1.1 Optical measurement and*

- microtopographies; calibration of interference microscopes and depth measurement standards for roughness measurement*. 2008, Beuth-Verlag: Berlin.
128. Born, M. and Wolf, E., *Principles of Optics: Electromagnetic Theory of Propagation, Interference and Diffraction of Light*. 7 ed. 1999, Cambridge: Cambridge University Press.
 129. Hecht, E., *Optics*. 2017, Pearson Education Limited,: Harlow, England. p. 1 online resource (729 pages).
 130. Page, D., *Interferometry*, in *Handbook of Optical Metrology : Principles and Applications*, T. Yoshizawa, Editor. 2015, Taylor & Francis Group: Baton Rouge, USA.
 131. de Groot, P., *Interference microscopy for surface structure analysis*, in *Handbook of Optical Metrology: Principles and Applications*, T. Yoshizawa, Editor. 2015, CRC Press: Boca Raton. p. 38.
 132. Schmit, J., *White-Light Interference 3D Microscopes*, in *Handbook of Optical Dimensional Metrology*, K. Harding, Editor. 2013, CRC Press: Boca Raton. p. 395-418.
 133. Balasubramanian, N., *Optical system for surface topography measurement*. 1982: United States.
 134. Davidson, M., Kaufman, K., Mazor, I. and Cohen, F., *An Application Of Interference Microscopy To Integrated Circuit Inspection And Metrology*. Microlithography Conferences. Vol. 0775. 1987: SPIE.
 135. Lee, B. S. and Strand, T. C., *Profilometry with a coherence scanning microscope*. *Appl. Opt.*, 1990. **29**(26): p. 3784-8.
 136. Dresel, T., Häusler, G. and Venzke, H., *Three-dimensional sensing of rough surfaces by coherence radar*. *Applied Optics*, 1992. **31**(7): p. 919-925.
 137. Häusler, G. and Neumann, J., *Coherence radar: an accurate 3D sensor for rough surfaces*. *Applications in Optical Science and Engineering*. Vol. 1822. 1993: SPIE.
 138. Caber, P. J., *Interferometric profiler for rough surfaces*. *Applied Optics*, 1993. **32**(19): p. 3438-3441.
 139. Deck, L. and de Groot. P., *High-speed noncontact profiler based on scanning white-light interferometry*. *Appl Opt*, 1994. **33**(31): p. 7334-8.
 140. Kino, G. S. and Chim, S. S., *Mirau correlation microscope*. *Appl Opt*, 1990. **29**(26): p. 3775-83.
 141. Chim, S. S. and Kino, G. S., *Three-dimensional image realization in interference microscopy*. *Appl. Opt.*, 1992. **31**(14): p. 2550-3.

142. de Groot, P. and Biegen, J., *Interference microscope objectives for wide-field areal surface topography measurements*. Optical Engineering, 2016. **55**(7).
143. de Groot, P. and Biegen, J., *A new class of wide-field objectives for 3D interference microscopy*. SPIE Optical Metrology. Vol. 9525. 2015: SPIE.
144. Roth, J. and de Groot, P., *Wide-field scanning white light interferometry of rough surfaces*. in *Spring Topical Meeting on Advances in Surface Metrology*. 1997. Annapolis, Maryland: ASPE.
145. Schmit, J., *White Light Interferometry*, in *Encyclopedia of Modern Optics*, R.D. Guenther, Editor. 2005, Elsevier: Oxford. p. 375-387.
146. de Groot, P. and Colonna de Lega, X., *Signal modeling for low-coherence height-scanning interference microscopy*. Applied Optics, 2004. **43**(25): p. 4821-4830.
147. Sheppard, C. J. R. and Larkin, K. G., *Effect of numerical aperture on interference fringe spacing*. Appl Opt, 1995. **34**(22): p. 4731-4.
148. de Groot, P., Colonna de Lega, X., Su, R., Leach, R. K., Novak, E. and Trolinger, J. D., *Does interferometry work? A critical look at the foundations of interferometric surface topography measurement*, in *Applied Optical Metrology III*. 2019.
149. Su, R., *Coherence scanning interferometry*, in *Advances in Optical Surface Texture Metrology*, R.K. Leach, Editor. 2020, IOP Publishing.
150. de Groot, P. and Colonna de Lega, X., *Fourier optics modeling of interference microscopes*. Journal of the Optical Society of America A, 2020. **37**(9).
151. Coupland, J., Mandal, R., Palodhi, K. and Leach, R. K., *Coherence scanning interferometry: linear theory of surface measurement*. Appl Opt, 2013. **52**(16): p. 3662-70.
152. Su, R., Coupland, J., Sheppard, C. and Leach, R. K., *Scattering and three-dimensional imaging in surface topography measuring interference microscopy*. Journal of the Optical Society of America A, 2021. **38**(2).
153. Beckmann, P. and Spizzichino, A., *The scattering of electromagnetic waves from rough surfaces*. 1987.
154. Su, R., Thomas, M., Liu, M., Drs, J., Bellouard, Y., Pruss, C., Coupland, J. and Leach, R. K., *Lens aberration compensation in interference microscopy*. Optics and Lasers in Engineering, 2020. **128**.
155. Ai, C. and Caber, P., *Combination of white-light scanning and phase-shifting interferometry for surface profile measurements*. 1995: United States.
156. Harasaki, A., Schmit, J. and Wyant, J. C., *Improved vertical-scanning interferometry*. Appl. Opt., 2000. **39**(13): p. 2107-15.

157. Larkin, K. G., *Efficient nonlinear algorithm for envelope detection in white light interferometry*. Journal of the Optical Society of America A, 1996. **13**(4): p. 832-843.
158. Sandoz, P., Devillers, R., and Plata, A., *Unambiguous profilometry by fringe-order identification in white-light phase-shifting interferometry*. Journal of Modern Optics, 1997. **44**(3): p. 519-534.
159. Sandoz, P., *Wavelet transform as a processing tool in white-light interferometry*. Opt. Lett., 1997. **22**(14): p. 1065-1067.
160. Caber, P., Martinek, S. and Niemann, R., *New interferometric profiler for smooth and rough surfaces*. Laser Dimensional Metrology: Recent Advances for Industrial Application. Vol. 2088. 1993: SPIE.
161. Pavliček, P. and Michálek, V., *White-light interferometry—Envelope detection by Hilbert transform and influence of noise*. Optics and Lasers in Engineering, 2012. **50**(8): p. 1063-1068.
162. Ai, C. and Novak, E., *Centroid approach for estimating modulation peak in broad-bandwidth interferometry*. 1997: United States.
163. Chen, S., Palmer, A. W., Grattan, K. T. V. and Meggit, B. T., *Digital signal-processing techniques for electronically scanned optical-fiber white-light interferometry*. Appl Opt, 1992. **31**(28): p. 6003-10.
164. de Groot, P., Colonna de Lega, X., Kramer, J. and Turzhitsky, M., *Determination of fringe order in white-light interference microscopy*. Applied Optics, 2002. **41**(22): p. 4571-4578.
165. de Groot, P. and Deck, L., *Surface profiling by analysis of white-light interferograms in the spatial frequency domain*. Journal of Modern Optics, 1995. **42**(2): p. 389-401.
166. de Groot, P. and Deck, L., *Three-dimensional imaging by sub-Nyquist sampling of white-light interferograms*. Opt Lett, 1993. **18**(17): p. 1462-4.
167. Schmit, J. and Olszak, A., *Challenges in white-light phase-shifting interferometry*. International Symposium on Optical Science and Technology. Vol. 4777. 2002: SPIE.
168. Wu, D., Liang, F., Kang, C. and Fang, F., *Performance Analysis of Surface Reconstruction Algorithms in Vertical Scanning Interferometry Based on Coherence Envelope Detection*. Micromachines (Basel), 2021. **12**(2).
169. Wu, D. and Fang, F., *Development of surface reconstruction algorithms for optical interferometric measurement*. Frontiers of Mechanical Engineering, 2020.

170. Gao, F., Leach, R. K., Petzing, J. and Coupland, J., *Surface measurement errors using commercial scanning white light interferometers*. Measurement Science and Technology, 2008. **19**(1).
171. Berger, R., Sure, T., and Osten, W., *Measurement errors of mirrorlike, tilted objects in white-light interferometry*. Optical Metrology. Vol. 6616. 2007: SPIE.
172. Su, R., Wang, Y., Coupland, J. and Leach, R. K., *On tilt and curvature dependent errors and the calibration of coherence scanning interferometry*. Opt Express, 2017. **25**(4): p. 3297-3310.
173. Pavliček, P. and Hybl, O., *White-light interferometry on rough surfaces—measurement uncertainty caused by surface roughness*. Appl Opt, 2008. **47**(16): p. 2941-9.
174. Lehmann, P. and Xie, W., *Signal formation in depth-scanning 3D interference microscopy at high numerical apertures*. in *SPECKLE 2015: VI International Conference on Speckle Metrology*. 2015. Guanajuato, Mexico: SPIE.
175. de Groot, P., *Vibration in phase-shifting interferometry*. Journal of the Optical Society of America A, 1995. **12**(2): p. 354-365.
176. Troutman, J., Evans, C., Ganguly, V. and Schmitz, T. L., *Performance evaluation of a vibration desensitized scanning white light interferometer*. Surface Topography: Metrology and Properties, 2013. **2**(1).
177. Pförtner, A. and Schwider, J., *Dispersion error in white-light Linnik interferometers and its implications for evaluation procedures*. Appl. Opt., 2001. **40**(34): p. 6223-6228.
178. Lehmann, P., Kühnhold, P. and Xie, W., *Reduction of chromatic aberration influences in vertical scanning white-light interferometry*. Measurement Science and Technology, 2014. **25**(6).
179. Doi, T., Toyoda, K. and Tanimura, Y., *Effects of phase changes on reflection and their wavelength dependence in optical profilometry*. Appl. Opt., 1997. **36**(28): p. 7157-7161.
180. Harasaki, A., Schmit, J. and Wyant, J. C., *Offset of coherent envelope position due to phase change on reflection*. Appl Opt, 2001. **40**(13): p. 2102-6.
181. Hovis, C., Shahinian, H. and Evans, C., *Observations on the effect of retrace error in scanning white light interferometry of smooth optical surfaces, in Optical Design and Fabrication 2019 (Freeform, OFT)*. 2019.
182. Baer, G., Schindler, J., Pruss, C., Siepmann, J. and Osten, W., *Calibration of a non-null test interferometer for the measurement of aspheres and free-form surfaces*. Opt Express, 2014. **22**(25): p. 31200-11.

183. Su, R., Thomas, M., Leach, R. K. and Coupland, J., *Effects of defocus on the transfer function of coherence scanning interferometry*. Opt Lett, 2018. **43**(1): p. 82-85.
184. Ekberg, P., Su, R. and Leach, R. K., *High-precision lateral distortion measurement and correction in coherence scanning interferometry using an arbitrary surface*. Opt Express, 2017. **25**(16): p. 18703-18712.
185. Harasaki, A. and Wyant, J. C., *Fringe modulation skewing effect in white-light vertical scanning interferometry*. Appl Opt, 2000. **39**(13): p. 2101-6.
186. Tavrov, A., Schmit, J., Kerwien, N., Osten, W. and Tiziani, H., *Diffraction-induced coherence levels*. Appl Opt, 2005. **44**(11): p. 2202-12.
187. Coupland, J. and Lobera, J., *Measurement of steep surfaces using white light interferometry*. Strain, 2010. **46**(1): p. 69-78.
188. Fay, M., Colonna de Lega, X. and de Groot, P., *Measuring high-slope and super-smooth optics with high-dynamic-range coherence scanning interferometry*. in *Classical Optics 2014*. 2014. Kohala Coast, Hawaii, United States: OSA Technical Digest (online).
189. Moench, W. and Zappe, H., *Fabrication and testing of micro-lens arrays by all-liquid techniques*. Journal of Optics A: Pure and Applied Optics, 2004. **6**(4): p. 330-337.
190. Vallance, R. R., Morgan, C. J., Shreve, S. M. and Marsh, E. R., *Micro-tool characterization using scanning white light interferometry*. Journal of Micromechanics and Microengineering, 2004. **14**(8): p. 1234-1243.
191. Bosseboeuf, A. and Petitgrand, S., *Application of microscopic interferometry techniques in the MEMS field*. Optical Metrology. Vol. 5145. 2003: SPIE.
192. Grigg, D., Felkel, E., Roth, J., Colonna de Lega, X., Deck, L. and de Groot, P., *Static and dynamic characterization of MEMS and MOEMS devices using optical interference microscopy*. Photonics Europe. Vol. 5455. 2004: SPIE.
193. Mack, C., *Reducing roughness in extreme ultraviolet lithography*. SPIE Photomask Technology and EUV Lithography. Vol. 10450. 2017: SPIE.
194. Sachs, R. and Stanzel, F., *Interference Microscopy for Clean Air – How Optical Metrology Is Improving Quality Control of Fuel Injection Systems*, in *Fringe 2013*, W. Osten, Editor. 2014, Springer, Berlin, Heidelberg. p. 535-538.
195. Zou, Y., Li, Y., Kaestner, M. and Reithmeier, E., *Low-coherence interferometry based roughness measurement on turbine blade surfaces using wavelet analysis*. Optics and Lasers in Engineering, 2016. **82**: p. 113-121.
196. Sandler, N., Kassamakov, I., Ehlers, H., Genina, N., Ylitalo, T. and Haeggstrom, E., *Rapid interferometric imaging of printed drug laden multilayer structures*. Sci Rep, 2014. **4**: p. 4020.

197. Scott, C. C., Luttge, A. and Athanasiou, K. A., *Development and validation of vertical scanning interferometry as a novel method for acquiring chondrocyte geometry*. J Biomed Mater Res A, 2005. **72**(1): p. 83-90.
198. Pecheva, E., Montgomery, P., Montaner, D. and Pramatarova, L., *White light scanning interferometry adapted for large-area optical analysis of thick and rough hydroxyapatite layers*. Langmuir, 2007. **23**(7): p. 3912-8.
199. Alchikh-Sulaiman, B., Carriere, P. and Yue, S., *For Powder Bed Additive Manufacturing Process: Correlations between Single Layer Density and Powder Properties with the Assistance of Coherence Scanning Interferometry*, in *POWDERMET 2019 International Conference on Powder Metallurgy & Particulate Materials*. 2019: Phoenix, AZ, USA.
200. Uğur Solakoğlu, E., Gürgen, S. and Kuşhan, M. C., *Surface topography of nickel-based superalloy manufactured with direct metal laser sintering (DMLS) method*. Surface Topography: Metrology and Properties, 2019. **7**(1).
201. Gomez, C., Campanelli, C., Su, R. and Leach, R. K., *Surface-process correlation for an ink-jet printed transparent fluoroplastic*. Surface Topography: Metrology and Properties, 2020. **8**(3).
202. Fay, M. and Dresel, T., *Applications of model-based transparent surface films analysis using coherence-scanning interferometry*. Optical Engineering, 2017. **56**(11).
203. Feng, X., Senin, N., Su, R., Ramasamy, S. and Leach, R. K., *Optical measurement of surface topographies with transparent coatings*. Optics and Lasers in Engineering, 2019. **121**: p. 261-270.
204. Yu, Y. and Mansfield, D., *Characterisation of Thin Films Using a Coherence Scanning Interferometry*. Journal of Materials Science and Chemical Engineering, 2015. **03**(01): p. 15-21.
205. Wiesner, B., Hybl, O. and Häusler, G., *Improved white-light interferometry on rough surfaces by statistically independent speckle patterns*. Appl. Opt., 2012. **51**(6): p. 751-757.
206. Ma, S., Quan, C., Zhu, R., Tay, C. J., Chen, L. and Gao, Z., *Application of least-square estimation in white-light scanning interferometry*. Optics and Lasers in Engineering, 2011. **49**(7): p. 1012-1018.
207. Gianto, G., Salzenstein, F. and Montgomery, P., *Comparison of envelope detection techniques in coherence scanning interferometry*. Appl Opt, 2016. **55**(24): p. 6763-74.
208. Lei, Z., Liu, X., Chen, L., Lu, W. and Chang, S., *A novel surface recovery algorithm in white light interferometry*. Measurement, 2016. **80**: p. 1-11.

209. Huang, Y., Gao, J., Zhang, L., Deng, H. and Chen, X., *Fast template matching method in white-light scanning interferometry for 3D micro-profile measurement*. Appl Opt, 2020. **59**(4): p. 1082-1091.
210. Vo, Q., Fang, F., Zhang, X. and Gao, H., *Surface recovery algorithm in white light interferometry based on combined white light phase shifting and fast Fourier transform algorithms*. Appl Opt, 2017. **56**(29): p. 8174-8185.
211. Lehmann, P., Tereschenko, S. and Xie, W., *Fundamental aspects of resolution and precision in vertical scanning white-light interferometry*. Surface Topography: Metrology and Properties, 2016. **4**(2).
212. Ghim, Y. S. and Davies, A., *Complete fringe order determination in scanning white-light interferometry using a Fourier-based technique*. Appl Opt, 2012. **51**(12): p. 1922-8.
213. Kiselev, I., Kiselev, E. I., Drexel, M. and Hauptmannl, M., *Noise robustness of interferometric surface topography evaluation methods. Correlogram correlation*. Surface Topography: Metrology and Properties, 2017. **5**(4).
214. Kiselev, I., Kiselev, E. I., Drexel, M. and Hauptmannl, M., *Precision of evaluation methods in white light interferometry. Correlogram correlation method*. Measurement, 2018. **123**: p. 125-128.
215. Lee-Bennett, I. *Advances in non-contacting surface metrology*. in *Frontiers in Optics 2004/Laser Science XXII/Diffractive Optics and Micro-Optics/Optical Fabrication and Testing*. 2004. Rochester, New York: Optical Society of America.
216. de Groot, P., *Surface profiling using an interference pattern matching template*. 2007, Zygo Corporation: United States.
217. Kim, S. W. and Kim, G. H., *Thickness-profile measurement of transparent thin-film layers by white-light scanning interferometry*. Appl Opt, 1999. **38**(28): p. 5968-73.
218. Mansfield, D. *The distorted helix: thin film extraction from scanning white light interferometry*. in *SPIE Photonics Europe*. 2006. SPIE.
219. de Groot, P. and Colonna de Lega, X., *Angle-resolved three-dimensional analysis of surface films by coherence scanning interferometry*. Opt Lett, 2007. **32**(12): p. 1638-40.
220. de Groot, P., Colonna de Lega, X. and Fay, M., *Transparent film profiling and analysis by interference microscopy*. Optical Engineering + Applications. Vol. 7064. 2008: SPIE.
221. Maniscalco, B., Kaminski, P. M. and Walls, J. M., *Thin film thickness measurements using Scanning White Light Interferometry*. Thin Solid Films, 2014. **550**: p. 10-16.

222. Park, M. C. and Kim, S. W., *Compensation of phase change on reflection in white-light interferometry for step height measurement*. Opt. Lett., 2001. **26**(7): p. 420-2.
223. Deck, L., de Groot, P. and Soobitsky, J., *Large-aperture, equal-path interferometer for precision measurements of flat transparent surfaces*. Appl Opt, 2014. **53**(8): p. 1546-53.
224. Beverage, J., Colonna de Lega, X. and Fay, M., *Interferometric microscope with true color imaging*. SPIE Optical Engineering + Applications. Vol. 9203. 2014: SPIE.
225. Hubel, P., Liu, J. and Guttosch, R., *Spatial frequency response of color image sensors: Bayer color filters and Foveon X3*. Electronic Imaging 2004. Vol. 5301. 2004: SPIE.
226. Hubel, P. and Bautsch, M., *Resolution for color photography*. Electronic Imaging 2006. Vol. 6069. 2006: SPIE.
227. Oh, J. S. and Kim, S.-W., *Femtosecond laser pulses for surface-profile metrology*. Optics Letters, 2005. **30**(19).
228. Joo, W.-D., Kim, S., Park, J., Lee, K., Lee, J., Kim, S., Kim, Y.-J. and Kim, S.-W., *Femtosecond laser pulses for fast 3-D surface profilometry of microelectronic step-structures*. Opt Express, 2013. **21**(13): p. 15323-34.
229. Lu, Y., Park, J., Yu, L. and Kim, S.-W., *3D profiling of rough silicon carbide surfaces by coherence scanning interferometry using a femtosecond laser*. Appl Opt, 2018. **57**(10): p. 2584-2589.
230. Sykora, D. and de Groot, P., *Instantaneous Interferometry: Another View*. in *International Optical Design Conference and Optical Fabrication and Testing*. 2010. Jackson Hole, Wyoming: Optical Society of America.
231. Sykora, D. and Holmes, M., *Dynamic measurements using a Fizeau interferometer*. SPIE Optical Metrology. Vol. 8082. 2011: SPIE.
232. Dunsby, C., Gu, Y. and French, P., *Single-shot phase-stepped wide-field coherence-gated imaging*. Opt Express, 2003. **11**(2): p. 105-115.
233. Millerd, J., Brock, N., Hayes, J., North-Morris, M., Novak, M. and Wyant, J., *Pixelated phase-mask dynamic interferometer*. Optical Science and Technology, the SPIE 49th Annual Meeting. Vol. 5531. 2004: SPIE.
234. Novak, M., Millerd, J., Brock, N., North-Morris, M., Hayes, J. and Wyant, J., *Analysis of a micropolarizer array-based simultaneous phase-shifting interferometer*. Appl. Opt., 2005. **44**(32): p. 6861-8.
235. Wiersma, J. T. and Wyant, J. C., *Vibration insensitive extended range interference microscopy*. Appl Opt, 2013. **52**(24): p. 5957-61.

236. Jeon, J. W., Jeong, H. W., Jeong, H. B. and Joo, K.-N., *High-speed polarized low coherence scanning interferometry based on spatial phase shifting*. Appl Opt, 2019. **58**(20): p. 5360-5365.
237. Thomas, M., Su, R., Nikolaev, N., Coupland, J. and Leach, R. K., *Modeling of interference microscopy beyond the linear regime*. Optical Engineering, 2020. **59**(03).
238. NewView 8300, *specification sheet SS-0100 01/17*, Zygo Corporation (2017).
239. Nexview/Newview 8000/ZeGage objective chart, *specification sheet SS-0101 12/15*, Zygo Corporation (2015).
240. ASM Aerospace Specification Metals, *Titanium TI-6AL-4V-AMS-4911*. (Available from: <https://www.aerospacemetals.com/titanium-ti-6al-4v-ams-4911.html>).
241. Brandl, E., Heckenberger, U., Holzinger, V. and Buchbinder, D., *Additive manufactured AlSi10Mg samples using Selective Laser Melting (SLM): Microstructure, high cycle fatigue, and fracture behavior*. Materials & Design, 2012. **34**: p. 159-169.
242. Giusca, C. L. and Leach, R. K., *Calibration of the Metrological Characteristics of Coherence Scanning Interferometers (CSI) and Phase Shifting Interferometers (PSI)*, in *NPL measurement good practice no. 127*. 2013, National Physical Laboratory.
243. Smith, D. W., Iacono, S. T. and Iyer, S. S., *Handbook of fluoropolymer science and technology*. 2014, John Wiley & Sons, Inc., Hoboken, New Jersey. p. 1 online resource.
244. Gardiner, J., *Fluoropolymers: Origin, Production, and Industrial and Commercial Applications*. Australian Journal of Chemistry, 2015. **68**(1): p. 13-22.
245. Ok, S., Sadaf, S. and Walder, L., *Basic characterization and investigation of a fluorinated terpolymer in pure state and in mixtures with kaolinite at solid interphases of thin films prepared by facile solution cast and nonsolvent methods*. High Performance Polymers, 2014. **26**(7): p. 779-789.
246. Améduri, B. and Boutevin, B., *Well-architected fluoropolymers : synthesis, properties and applications*. 2004, Oxford: Elsevier. xvii, 480 p.
247. Drobny, J. G., *Technology of fluoropolymers*. 2008, CRC Press: Boca Raton, FL. p. 248.
248. Ok, S., Furquan, S. A, Khan, Z. and Dogan, A. U., *Near superhydrophobic-fluorinated THV fiber-like structures and fibers prepared by electrospinning*. High Performance Polymers, 2016. **28**(2): p. 206-214.

249. Pacetti, S., *Use of a terpolymer of tetrafluoroethylene, hexafluoropropylene, and vinylidene fluoride in drug eluting coatings on medical devices*. 2008: United States.
250. Begolo, S., Colas, G., Viovy, J.-L. and Malaquin, L., *New family of fluorinated polymer chips for droplet and organic solvent microfluidics*. *Lab Chip*, 2011. **11**(3): p. 508-12.
251. Slim, C., Ratajovà, E., Griveau, S., Kanoufi, F., Ferraro, D., Perréard, C., d'Orlyé, F., Varenne, A. and Bedioui, F., *Two-step local functionalization of fluoropolymer Dyneon THV microfluidic materials by scanning electrochemical microscopy combined to click reaction*. *Electrochemistry Communications*, 2015. **60**: p. 5-8.
252. Hutchings, I. M. and Martin, G., *Inkjet technology for digital fabrication*. 2013, Chichester, West Sussex, United Kingdom: John Wiley & Sons Ltd. xvi, 372 pages, 16 pages of color plates.
253. Dimatix Materials Printer, *DMP-2850 Data Sheet*, Fujifilm (2019).
254. PICO Pulse Jet Valve System, *PICO Pulse Data Sheet*, Nordson EFD (2018).
255. Smallwood, I., *Handbook of organic solvent properties*. 1996, New York: Butterworth-Heinemann. 306.
256. Goustouridis, D., Manoli, K., Chatzandroulis, S., Sanopoulou, M. and Raptis, I., *Characterization of polymer layers for silicon micromachined bilayer chemical sensors using white light interferometry*. *Sensors and Actuators B: Chemical*, 2005. **111-112**: p. 549-554.
257. Digital Surf, *Digital Surf MountainsMap Software*. (2017).
258. Deegan, R. D., *Pattern formation in drying drops*. *Physical Review E*, 2000. **61**(1): p. 475-85.
259. Kuang, M., Wang, L. and Song, Y., *Controllable printing droplets for high-resolution patterns*. *Adv Mater*, 2014. **26**(40): p. 6950-8.
260. Xue, L. and Han, Y., *Inhibition of dewetting of thin polymer films*. *Progress in Materials Science*, 2012. **57**(6): p. 947-979.
261. Okuzono, T., Ozawa, K. and Doi, M., *Simple model of skin formation caused by solvent evaporation in polymer solutions*. *Phys Rev Lett*, 2006. **97**(13): p. 136103.
262. Baldwin, K. A. and Fairhurst, D. J., *The effects of molecular weight, evaporation rate and polymer concentration on pillar formation in drying poly(ethylene oxide) droplets*. *Colloids and Surfaces A: Physicochemical and Engineering Aspects*, 2014. **441**: p. 867-871.

263. Li, Y., Yang, Q., Li, M. and Song, Y., *Rate-dependent interface capture beyond the coffee-ring effect*. Sci Rep, 2016. **6**: p. 24628.
264. Gomez, C., Su, R., de Groot, P. and Leach, R. K., *Noise reduction in coherence scanning interferometry for surface topography measurement*. Nanomanufacturing and Metrology, 2020. **3**(1): p. 68-76.
265. Gao, W., Haitjema, H., Fang, F. Z., Leach, R. K., Cheung, C. F., Savio, E. and Linares, J. M., *On-machine and in-process surface metrology for precision manufacturing*. CIRP Annals, 2019. **68**(2): p. 843-866.
266. Hosseini, P., Zhou, R., Kim, Y.-H., Peres, C., Diaspro, A., Kuang, C., Yaqoob, Z. and So, P. T. C., *Pushing phase and amplitude sensitivity limits in interferometric microscopy*. Opt Lett, 2016. **41**(7): p. 1656-9.
267. Pavliček, P. and Hybl, O., *White-light interferometry on rough surfaces—measurement uncertainty caused by noise*. Appl Opt, 2012. **51**(4): p. 465-73.
268. Brophy, C. P., *Effect of intensity error correlation on the computed phase of phase-shifting interferometry*. Journal of the Optical Society of America A, 1990. **7**(4).
269. Bendat, J. S. and Piersol, A. G., *Random data : analysis and measurement procedures*. 4th ed. Wiley series in probability and statistics. 2010, Hoboken, NJ: Wiley-Blackwell. xxi, 604 p.
270. Haitjema, H. and Morel, M. A. A., *Noise bias removal in profile measurements*. Measurement, 2005. **38**(1): p. 21-29.
271. Abbas, G. L., Babbitt, W. R., de La Chapelle, M., Fleshner, M. L., McClure, J. D. and Vertatschitsch, E., *High-precision fiber-optic position sensing using diode laser radar techniques*. OE/LASE '90. Vol. 1219. 1990: SPIE.
272. Fleming, A. J., *A review of nanometer resolution position sensors: Operation and performance*. Sensors and Actuators A: Physical, 2013. **190**: p. 106-126.
273. de Groot, P. and DiSciacca, J., *Surface-height measurement noise in interference microscopy*. SPIE Optical Engineering + Applications. Vol. 10749. 2018: SPIE.
274. Vanrusselt, M., Haitjema, H., Leach, R. K. and de Groot, P., *International comparison of noise in areal surface topography measurements*. Surface Topography: Metrology and Properties, 2021. **9**(2): p. 025015.
275. Kladovasilakis, N., Charalampous, P., Kostavelis, I., Tzetzis, D. and Tzovaras, D., *Impact of metal additive manufacturing parameters on the powder bed fusion and direct energy deposition processes: a comprehensive review*. Progress in Additive Manufacturing, 2021.

276. Gockel, J., et al., *The influence of additive manufacturing processing parameters on surface roughness and fatigue life*. International Journal of Fatigue, 2019. **124**: p. 380-388.
277. Majeed, A., Ahmed, A., Salam, A. and Sheikh, M. Z., *Surface quality improvement by parameters analysis, optimization and heat treatment of AlSi10Mg parts manufactured by SLM additive manufacturing*. International Journal of Lightweight Materials and Manufacture, 2019. **2**(4): p. 288-295.
278. Osma, A., *An assessment of the robustness of gauge repeatability and reproducibility analysis in automotive components*. Proceedings of the Institution of Mechanical Engineers, Part D: Journal of Automobile Engineering, 2011. **225**(7): p. 895-912.
279. Wang, F. K., Chern, H. L. and Yu, T. C., *A Gauge Study for Dynamic Light Scattering and Differential Mobility Analyzer Instruments*. Journal of Testing and Evaluation, 2012. **40**(4): p. 580-585.
280. Syam, W. P., Rybalcenko, K., Gaio, A., Crabtree, J. and Leach, R. K., *Methodology for the development of in-line optical surface measuring instruments with a case study for additive surface finishing*. Optics and Lasers in Engineering, 2019. **121**: p. 271-288.